The Role of Microtubule End Structure in Microtubule Acetylation and Dynamics

A DISSERTATION

SUBMITTED TO THE FACULTY OF THE GRADUATE SCHOOL

OF THE UNIVERSITY OF MINNESOTA

BY

Courtney Elizabeth Coombes

IN PARTIAL FULFILLMENT OF THE REQUIREMENTS

FOR THE DEGREE OF

DOCTOR OF PHILOSOPHY

Advisor, Melissa K. Gardner

July, 2016

Acknowledgments

I would like to first thank my advisor Melissa Gardner for guiding me through this journey. She has encouraged me, supported me, and pushed me to be the best student I could be. Her mentorship has been invaluable, and I would not have succeeded without her.

I would like to thank all of the members of the Gardner Lab, past and present. Each of you has made it easy and enjoyable to come to work. I am grateful for all of your help, thoughtful discussions, and encouragement. Thank you to Jeremy Chacon, Soumya Mukherjee, Lauren Jelenchick, Taylor Reid, Mark McClellan, Damien Tank, Patrick Willey, Bre Schuster, Melissa Plooster, Ami Yamamoto, Stephanie Dewald, Qing Yang, Sneha Parmar, and Lauren Douglas.

I would like to thank my thesis committee members Mary Porter, David Odde, Jim Ervasti, Tom Hays, and G.W. Gant Luxton for their constructive guidance and support. I would also like to thank the members of the Clarke, Titus, Luxton, and Courtemanche Labs for insightful discussion and feedback during lab meetings.

I thank my collaborators David Odde, G.W. Gant Luxton, Joshua D. Alper, and Jonathon Howard for their invaluable contributions to my projects.

Thank you to the American Heart Association for funding my research for two years.

Thank you to my fellow graduate students, especially Allison O'Rourke and Jami Erickson, for your support and friendship.

Thank you to my friends and family for your unwavering support during this and every other part of my life. In particular, I thank Brandon Coombes for always standing by my side.

Dedication

This thesis is dedicated to my father, Mike Goodrich, who always expected me to be excellent, and to my mother, Vicky Eitel, who reminded me I'd be loved regardless.

Abstract

Microtubules are long hollow filaments that have the striking ability to restructure themselves. This is accomplished via a behavior termed “dynamic instability”, which involves stochastic transitions between growing and shortening at microtubule ends. They are also subject to post-translational modifications including acetylation. By performing biochemical assays, fluorescence and electron microscopy experiments, and computational simulations, we found that both acetylation and changes in dynamics are dependent on the microtubule structure itself.

Acetylation is unique from other post-translational modifications in that it is the only modification which takes place in the hollow lumen of the microtubule. It is known that the α-tubulin acetyltransferase αTAT1 is responsible for the majority of the microtubule acetylation that is observed in cells. However, the mechanism for how αTAT1 accesses the Lys40 acetylation site inside of the microtubule lumen is not fully understood. We found that the microtubule α-tubulin acetylation rate is limited by accessibility of the enzyme to the lumen, and that αTAT1 preferentially targets tapered microtubule ends with exposed Lys40 acetylation sites. These results provide important insights into the mechanism for αTAT1 microtubule acetylation and its dependence on the microtubule structure.

Tapering at microtubule ends may also be playing a role in microtubule dynamics. The dynamics at microtubule ends are characterized by periods of slow growth, followed by stochastic switching events termed “catastrophes”, in which microtubules suddenly undergo rapid shortening. The mechanistic basis of catastrophe is not known. To investigate microtubule catastrophe events, we performed 3D mechanochemical simulations that account for interactions between neighboring protofilaments. We found that there are two separate factors which contribute to catastrophe events in the 3D simulation: the GTP-Tubulin cap size and the structure of the microtubule tip. Importantly, 3D simulations predict, and both fluorescence and electron microscopy experiments confirm, that microtubule tips become more tapered as the microtubule grows. This effect destabilizes the tip and ultimately contributes to microtubule catastrophe. Thus, the likelihood of a catastrophe event may be intimately linked to the aging physical structure of the growing microtubule tip.

Table of Contents

List of Tables

List of Figures

Chapter One

Introduction

Microtubule Function and Structure

Microtubules are cylindrical polymers that, along with actin and intermediate filaments, make up the cytoskeleton. These structures are both rigid and dynamic, which make them useful for building temporary structures like the mitotic spindle and for maintaining more permanent cellular architecture in non-dividing cells (Figure 1-1). Spindle formation during mitosis and meiosis requires a complex cooperation of many dynamic microtubules, molecular motors, and other mitotic proteins, which ultimately wrangle, align, and separate chromosomes to prepare for cell division. When cells are not dividing, microtubules provide a radial array on which molecular motors can carry cargo to and from the cell's center and periphery, participate in cell signaling, help maintain overall cell morphology by positioning the nucleus and other organelles, and form axonemes in appendages like cilia. Because microtubules are necessary for a wide range of cellular processes, they are the target for several medical treatments.

Microtubules are made up of α- and β- tubulin heterodimers that stack end to end in long thin structures called protofilaments. These protofilaments, usually 13, are bound laterally to form a long hollow tube polymer (Figure 1-2). This structure is dynamic via the addition and loss of tubulin heterodimers at the ends of the tube. During the addition of new heterodimers, the α-tubulin subunit of one dimer will bind to the β- tubulin subunit of another. This confers a polarity to the microtubule structure where the plus end has β-tubulin subunits exposed, while the minus end exposes α-tubulin subunits. In cells, most loss and addition of tubulin subunits occurs at the plus end. As tubulin dimers add to the plus end, they are each bound to a GTP molecule [1]. Once incorporated into the microtubule lattice, the GTP will stochastically hydrolyze [2]. This hydrolysis cycle drives microtubule dynamics.

Microtubule Dynamics

Microtubules can grow slowly for long periods of time and to long lengths, and then stochastically start to rapidly shrink. This switch is termed a "catastrophe". In contrast, a shrinking microtubule can switch back to a growing state, which is known as a "rescue". This behavior, described as dynamic instability [3], is essential for cell growth and survival. It allows the microtubule network to restructure and evolve to perform its various functions. It also allows microtubules to perform mechanical work through

pushing forces during polymerization and pulling forces by depolymerization [4–6]. These dynamics can be modulated by drugs to treat human diseases including cancer [7].

In cells, microtubule dynamics are also regulated by different microtubule associated proteins. Some proteins cause catastrophe such as kinesin-13 [8–15] and kinesin-8 [8,15–19]. Katanin severs the lattice of stable microtubules, which then leads to disassembly [20]. Conversely, microtubule polymerization can be catalyzed by the protein XMAP215 [21] and catastrophe can be suppressed by the proteins tau [22] and doublecortin [23]. Additionally, microtubule dynamics may be modulated by the intrinsic microtubule structure itself. This is in part due to the concentrated GTP loaded subunits at the growing end of the microtubule, known as the GTP cap [1,3,24–26]. Loss of this protective structure is thought to induce microtubule catastrophe [27–31]. However, how and in what conditions the GTP cap is lost is still a topic of study. It was once hypothesized that microtubule catastrophe was strictly a single step process by which any microtubule would randomly and stochastically lose the GTP cap and undergo a catastrophe [32,33]. We now know that microtubule catastrophe is not strictly a single-step random process but instead is age dependent; in that short, young microtubules are less likely to catastrophe than longer, older microtubules [15,34,35]. This phenomenon could be caused by an age dependent decay of the GTP cap size, or possibly by a change in the microtubule structure at the growing plus end. Some predict that the GTP cap may be quite large, greater than 100 layers of tubulin away from the growing microtubule tip [36], which may not change over time. On the other hand, microtubule plus ends can adopt varying degrees of tapering: some are blunt because the protofilaments are all similar lengths, while others have protofilaments with widely varying lengths [37]. Changes in the degree of tapering could create instability at the microtubule ends and predispose a microtubule to catastrophe. These structural changes could occur in a time dependent manner to promote catastrophe, but may also be modified by different microtubule associated proteins to control microtubule dynamics in cells.

Microtubule Acetylation

The microtubule network can also evolve through the accumulation of post-translational modifications. These modifications may help fine tune microtubule function by changing their dynamics, their interactions with other microtubule associated proteins, or their spatial arrangements [38]. The most noteworthy modifications that microtubules

are subject to are polyglycylation, polyglutamylation, detyrosination, Δ2-tubulin generation, and acetylation (Figure 1-3). The focus of this work is on one of the first discovered modifications, microtubule acetylation [38,39].

Acetylated tubulin was discovered in the green algae *Chlamydomonas reinhardtii* axonemes [39]. We now know that acetylated microtubule networks are in other cellular structures in addition to flagella, such as the mitotic spindle [40,41], and neuronal axons [42–44]. While the other post-translational modifications occur on the carboxy-terminal tails of tubulin subunits, acetylation occurs on the ε-amino group of lysine 40 (K40) of α-tubulin subunits, which resides on an unstructured loop within the hollow portion of the tube polymer, known as the lumen (Figure 1-3) [1,45–48]. Acetylation was first detected using ^{3}H acetate [39], but then labeled using the Clone 6-11B-1 antibody, which is still the only antibody available that specifically and exclusively binds to the acetylated K40 residue [40,49].

Microtubule acetylation is often associated with stable microtubule networks; however, it is not known whether acetylation stabilizes microtubules per se, as it may only passively mark stabilized microtubules. In initial studies, acetylated microtubules that were put in depolymerizing conditions, such as in cold or with treatment of nocodozole and colchicine, seemed to be more resistant to such conditions than their unacetylated counterparts [40,49–53]. These studies suggested that acetylation acted to stabilize those microtubules in some way. However, other studies showed that if you stabilize microtubules in cells using the drug Taxol, the microtubules then become acetylated [40]. These experiments suggest that acetylation may instead be a marker of stability instead of a change that confers stability. Still, other studies have shown that actively dynamic microtubule networks can be acetylated as well [54], so it remains unclear how this modification affects dynamics for both individual microtubules and global microtubule networks.

Along with its controversial effects on microtubule dynamics, microtubule acetylation has also been linked to several other functional changes involving microtubules. Studies have found that acetylation can influence the binding and interactions of some microtubule associated proteins on the outer lattice. The binding and processivity of the motors kinesin-1 and cytoplasmic dynein may be directly impacted by microtubule acetylation levels [55–57]. Similarly, acetylated portions of microtubules tend to be more sensitive to severing by the protein katanin [58]. In *Caenorhabditis elegans* touch receptor neurons, microtubule acetylation is needed to

constrain the number of protofilaments per microtubule [59,60], which suggests that acetylation may be affecting the interactions between tubulin subunits. However, in vitro 3D cryo-electron microscopy has demonstrated that the sub-nanometer structures of acetylated and deacetylated tubulin are not different in any distinguishable way [61]. Likewise, lack of α-tubulin acetylation is not essential in protist *Tetrahymena* cells, and these mutant cells are also indistinguishable from their wild-type counterparts [62]. With each of these studies, it is difficult to define universal attributes of acetylated tubulin that would be able to explain how the microtubule network is affected in such different ways. Instead it seems that cells have evolved to control acetylation in different ways depending on the specific structure or network. Because of this, the physiological role of K40 acetylation remains a mystery.

The Microtubule Acetyltransferase, αTAT1

One reason that the functional importance of microtubule acetylation has remained elusive is because, until recently, many studies were carried out by manipulating the levels of the K40 tubulin deacetylases: histone deacetylase 6 (HDAC6) [63,64] and sirtuin 2 (SIRT2) [65]. This made interpretation of physiological results difficult because both enzymes have several other substrates and functions [66–69]. Many acetyltransferases are able to acetylate α-tubulin subunits. These enzymes include arrest-defective 1–amino-terminal, α-amino, acetyltransferase 1 (ARD1-NAT1) [70], general control of amino acid synthesis 5 (GCN5) [71], and the elongator protein complex (ELP complex) [72,73]. However, these acetyltransferases are also known to acetylate substrates other than tubulin. Recently, a K40-specific acetyltransferase related to GCN5 was discovered in *C. elegans* and *Tetrahymena* [74]. This acetyltransferase (called MEC-17) was found to exclusively acetylate K40 of α-tubulin [74]. Its orthologues in mammals were shown to have the same function, and so the protein is now known as α-tubulin N-acetyltransferase 1 (αTAT1) [75,76]. The X-ray crystal structure of the αTAT1/acetyl-CoA complex has been solved (Figure 1-4) [77,78]. In this study, Friedmann et al. found that while αTAT1 is structurally similar to GCN5, its unique substrate binding groove is important for exclusive α-tubulin K40 acetylation. Knockout studies demonstrated that αTAT1 is the major tubulin acetyltransferase in *Tetrahymena*, *C. elegans*, and mice [74–76]. It is also present and active in zebrafish [74].

Lack of αTAT1 in all model organisms studied is not lethal, but can cause a wide array of structural abnormalities. As mentioned previously, when αTAT1 is absent in C.

elegans, the microtubules in the touch receptor neurons have variable numbers of protofilaments and are also shorter than in wild-type [59,60,79]. These structural abnormalities led to a reduction in touch responsiveness in the mutant worms. αTAT1 activity is also important in zebrafish neuron structure and function, along with general body shape and body axis [74]. Mice lacking αTAT1 are remarkably normal. Without αTAT1 there are reductions in sperm motility and thus male mouse fertility [75] and some structural deformations in the dentate gyrus of the brain [76]. Normally there are high αTAT1 expression levels in the mouse brain, which suggests that it may help fine tune microtubule function in neurons for higher order behavior. In line with this reasoning, it was found that the 8 week old αTAT1 knockout mice did exhibit slight anxiety during open field tests [75]. Interestingly, in mammalian cells, loss of αTAT1 leads to an increase, not decrease, in stabilized microtubules [75]. Similarly, when αTAT1 is increased in mouse fibroblasts, there is an increase in microtubule dynamics. This is true even when αTAT1 is mutated and no longer able to acetylate tubulin [80]. These intriguing results suggest that αTAT1 binding to microtubules and αTAT1 mediated acetylation may confer different and separable affects to the microtubule structure or function.

Aside from the functional outcomes of αTAT1's interaction with microtubules, it is also not understood how αTAT1 accesses the luminal acetylation site. The enzyme is far more active on the polymerized form of tubulin than it is on dimers [74,81–84], and so αTAT1 must enter the hollow microtubule to acetylate the α-tubulin subunits. However, it is not immediately obvious how αTAT1 could travel within the lumen to bind and acetylate K40 sites. This is because diffusion of a molecule with even a modest affinity for the luminal side of the tubulin subunits is predicted to be very slow due to the high concentration of K40 sites within the small volume of the lumen [85]. Several theorized potential mechanisms for K40 access exist. Some groups predict that the enzyme takes advantage of a phenomenon known as microtubule breathing, which is thought to create transient openings between protofilaments [61,83,86]. This temporary opening could either allow αTAT1 into the lumen at any position along the microtubule, or could perhaps allow the loop that K40 resides on to escape to the outer side of the lattice. Other groups suggest that αTAT1 enters the microtubule through the microtubule ends [74,84] and either diffuses slowly as previously predicted [74] or rapidly diffuses along the luminal wall [84]. If αTAT1 does primarily enter through the ends, the tapering that exists at the plus end could play a role by physically exposing the normally enclosed K40 binding sites. It will

be important to distinguish among these possibilities to fully understand the mechanism and contexts by which microtubules become acetylated.

Microtubule Acetylation and Human Disease

Misregulation of microtubule acetylation and/or αTAT1 has been linked to several human diseases. Many of these diseases are neurodegenerative in nature, which is not surprising since several of the phenotypes associated with misregulated microtubule acetylation in model organisms occur in neurons. In human neurons, microtubule acetylation may be important for intracellular transport of vesicles. In Huntington's disease, microtubule-dependent transport of brain-derived neurotrophic factor (BDNF) is altered, which leads to neuronal death [57]. Dompierre et al. showed that neurons from Huntington's disease patients had reduced microtubule acetylation levels and that increasing the overall microtubule acetylation levels in these neurons rescued anterograde and retrograde transport. Similarly, Chen et al. found that microtubule acetylation modulates mitochondrial transport, which may have implications in Alzheimer's disease and Parkinson's disease [87]. In Parkinson's disease, abnormal aggregates of protein called Lewy bodies, which contain α-synuclein, develop and cause neuronal toxicity. When the deacetylase SIRT2 is inhibited, which results in hyperacetylation of the neuronal microtubules, this α-synuclein toxicity is reduced [88]. Hyperacetylation has also been shown to decrease the binding of mutant Leucine-rich repeat kinase 2 protein and rescue axonal transport in Parkinson's disease models [89].

In addition to neurodegenerative disease, microtubule acetylation has also been linked to different forms of cancer. Interestingly, the protective levels of acetylation seem to differ among different cancers. In breast cancer, HDAC6 expression, and presumably lower microtubule acetylation levels, is correlated with better patient survival [90]. However, HDAC6 inhibitors have also shown to be therapeutic against cancer via their antimetastatic and antiangiogenic properties [91]. In addition, when used with paclitaxel, HDAC6 inhibitors can also increase apoptosis in thyroid cancer cell lines [92]. However, for these human disease studies, it is difficult to know if the effects and correlations are due to the modulations in tubulin acetylation or in other cellular processes.

Finally, microtubule acetylation, along with increases in microtubule density, may play a role in the disease conditions associated with hypertension [93]. Part of this story is understood: increased pressure load causes an overall increase in microtubule density,

leading to an increase in cellular stiffness and viscosity. The increase in viscosity dampens the myocyte's ability to elongate and shorten, causing contractile dysfunction and ultimately contributing to heart failure [94,95]. However, less understood is the role of the increased microtubule acetylation that accompanies the increase in microtubule density [93].

Conclusions and Thesis Aims

Microtubules possess the remarkable ability to maintain structural rigidity while dynamically changing their lengths, the proteins bound to their surface, and their post translational modifications. These dynamic changes are intimately linked to the microtubule structure as a whole. The focus of this thesis is to understand how microtubule structure, particularly at the plus end, affects both the entry mechanism for the α-tubulin acetyltransferase αTAT1 during microtubule acetylation, and also the mechanism for microtubule catastrophe. Although these two processes are widely disparate, I hypothesize that they are linked by their dependence on the microtubule end structure created by differing distributions of protofilament lengths.

In my thesis work, I first identified how αTAT1 accesses the α-tubulin subunits and how this process is hindered by the hollow tube structure of the microtubule. I hypothesized that the small volume of the lumen, and thus the high concentration of potential αTAT1 binding sites, leads to inefficient αTAT1 mobility while inside the enclosed lumen structure. Similarly, I hypothesized that tapering at microtubule ends could allow access to the normally enclosed lumen and increase the probability of αTAT1 binding to those microtubule ends. Also, I determined the effect of both αTAT1 binding and acetylation on microtubule structure and dynamics of stable microtubule populations. I tested these hypotheses by performing biochemical assays, fluorescence and electron microscopy experiments, and computational simulations.

Secondly, I determined the structural morphology of the microtubule tip over time and its effect on microtubule dynamics. I visualized the structure of the microtubule tip over time *in vitro* and *in vivo* using Total Internal Reflection Fluorescence (TIRF) microscopy and Transmission Electron microscopy (TEM) and measured the effect on dynamics through computational modeling and *in vitro* assays to show that changes in tip structure directly affect microtubule dynamics.

Figures

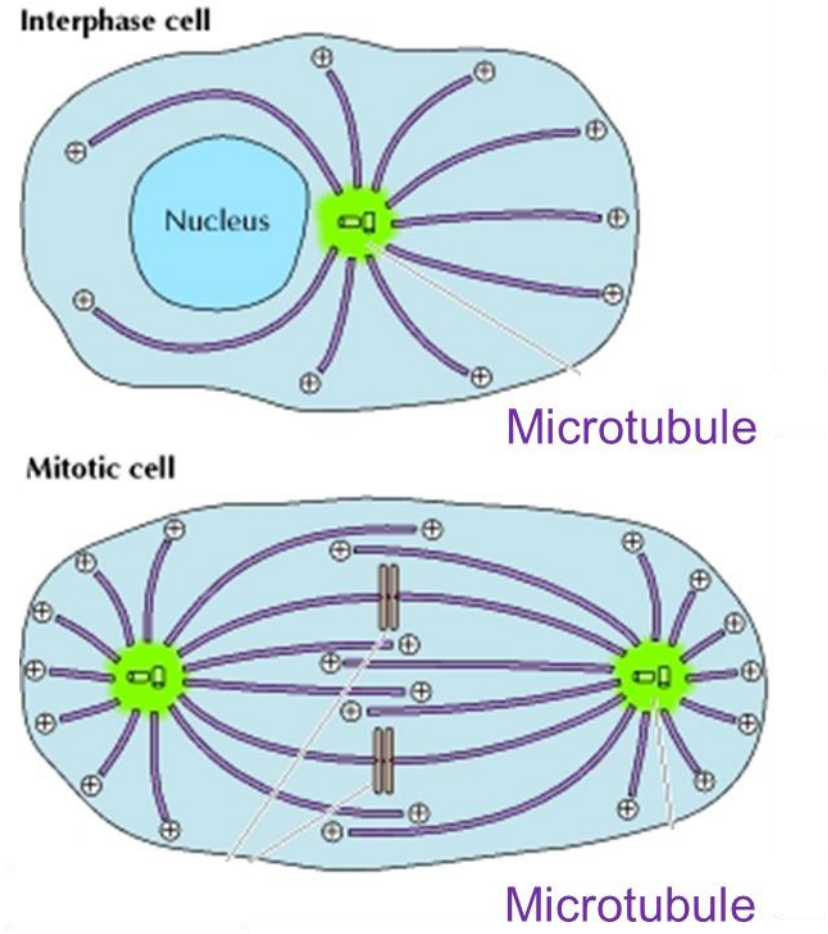

Figure 1-1: Microtubules in the cell. Schematic representation of microtubule networks in non-dividing and in dividing cells. Adapted from The Cell: A Molecular Approach. 2nd edition.

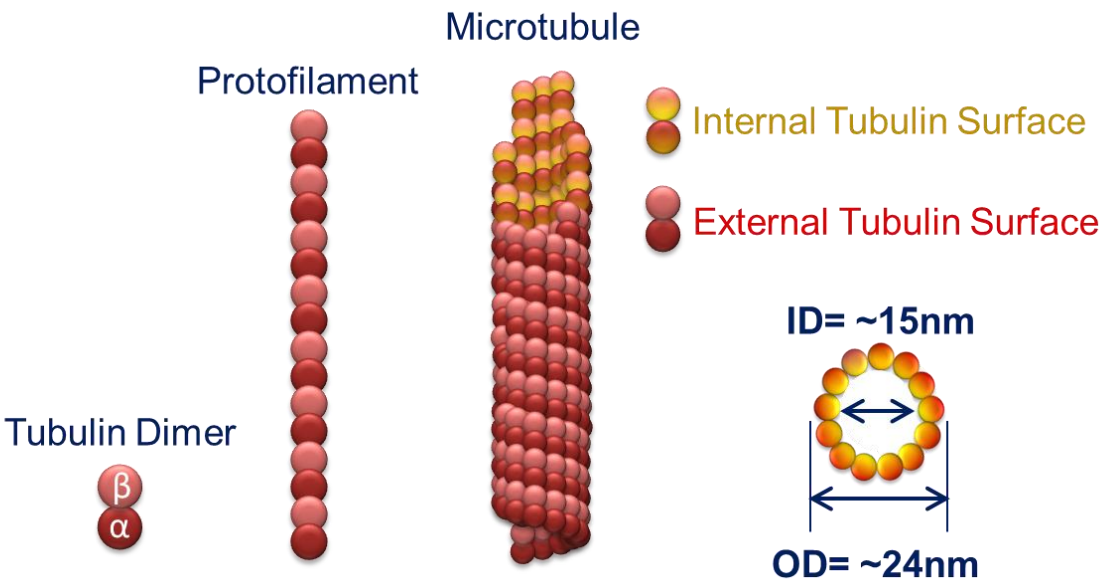

Figure 1-2: The microtubule structure. Schematic representation of the microtubule polymer made of tubulin heterodimers.

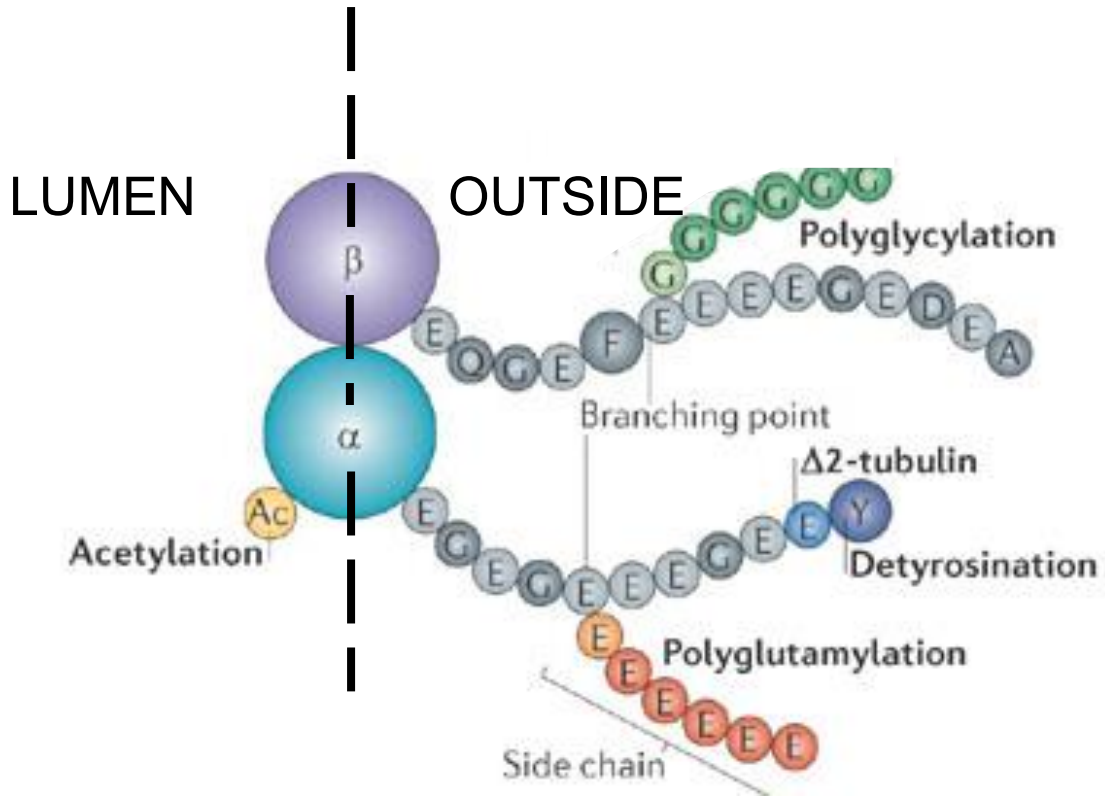

Figure 1-3: Microtubule post-translational modifications. Schematic representation of where post-translational modifications occur on the tubulin subunits. Adapted from Janke and Chloe Bulinski, 2011 [38]

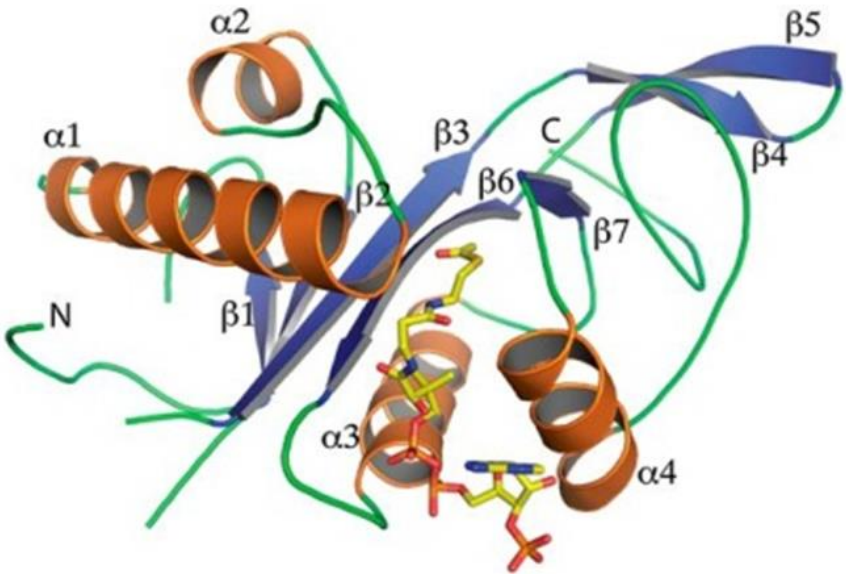

Figure 1-4: Structure of the αTAT1/AcCoA complex. Schematic representation of the complex, α-helices (orange) are numbered 1-4, β-strands (blue) are numbered 1-7, loops are colored green, and the N and C termini are indicated. AcCoA is represented as sticks and colored according to element: carbon, yellow; nitrogen, blue; and oxygen, red. From Friedmann et al. (2012) [77]

Chapter Two

Mechanism of microtubule lumen entry for the α-tubulin acetyltransferase enzyme αTAT1

Courtney E. Coombes conceived of and participated in study design, carried out all TIRF, all TEM, and most western blot experiments, participated in analysis of data, and drafted the manuscript.

Ami Yamamoto and Melissa Plooster participated in western blot experiments.

Mark McClellan purified protein for experiments.

G.W. Gant Luxton, Joshua D. Alper, and Jonathon Howard provided theoretical direction and participated in study design.

Melissa K. Gardner participated in study design, participated in data analysis, created the model simulation, and participated in drafting the manuscript.

Summary and Significance Statement

Microtubules are structural polymers inside of cells that are subject to post-translational modifications. These post-translational modifications create functionally distinct subsets of microtubule networks in the cell, and acetylation is the only modification that takes place in the hollow lumen of the microtubule. While it is known that the α-tubulin acetyltransferase αTAT1 is the primary enzyme responsible for microtubule acetylation, the mechanism for how αTAT1 enters the microtubule lumen to access its acetylation sites inside of the microtubule lumen is not well understood. By performing biochemical assays, fluorescence and electron microscopy experiments, and computational simulations, we found that αTAT1 enters the microtubule lumen through the microtubule ends, and through bends or breaks in the lattice. Thus, microtubule structure is an important determinant in the acetylation process. In addition, once αTAT1 enters the microtubule lumen, the mobility of αTAT1 within the lumen is controlled by the affinity of αTAT1 for its acetylation sites, due to the rapid rebinding of αTAT1 onto the highly concentrated α-tubulin acetylation sites. These results have important implications for how acetylation could gradually accumulate on stable subsets of microtubules inside of the cell.

αTAT1 is an enzyme that acetylates microtubules inside of cells, and acetylation is an important post-translational microtubule modification. However, microtubules are long, hollow tubes, and the acetylation site for αTAT1 is on the inside of this hollow tube. We investigated how αTAT enters the tube, and how it moves around to access its acetylation sites once inside the microtubule. We found that αTAT1 enters microtubules through its ends, but does not move efficiently inside of the microtubule. However, a lowered affinity allows the enzyme to move more efficiently, and leads to longer stretches of acetylation. Therefore, acetylation of microtubules could be controlled in the cell by modulating the affinity of αTAT1 for its acetylation site, or by increasing microtubule ends.

Introduction

Microtubules are dynamic structural polymers that participate in cell and organelle morphology and motility, intracellular transport, signaling, and chromosome movement during mitosis. Despite these various roles, microtubule structure is highly conserved: microtubules across a wide range of organisms are hollow tube structures that are made up of α- and β-tubulin heterodimers stacked end-to-end into protofilaments. For microtubules to perform such a wide range of tasks, the cell utilizes a variety of post-translational modifications to fine-tune their function [38,96]. Unlike the other known microtubule post-translational modifications, the enzyme responsible for microtubule acetylation must access the α-tubulin Lysine 40 (Lys40) site inside the hollow portion of the microtubule, known as the lumen, to acetylate microtubules [47,48]. Because of this unique localization to the lumen, the functional consequences of microtubule acetylation were initially puzzling to the field. However, recent functional studies have revealed effects of microtubule acetylation on cell signaling [97], cell cycle progression [98], and breast cancer cell migration [99]. In humans, microtubule acetylation may be important for intracellular cargo transport in neurons and neuronal maintenance in neurodegenerative disease contexts, including Alzheimer's [100], Parkinson's [88,89], and Huntington's Disease [57].

The primary enzyme which is responsible for α-tubulin Lys40 acetylation in mammals, nematodes, and protozoa has been identified as α-tubulin acetyltransferase 1 (αTAT1), which was first found in *Tetrahymena* and *Caenorhabditis elegans* [74,75,83]. However, despite identification of the enzyme and its substrate, the mechanism for how αTAT1 enters the microtubule lumen to access its acetylation sites is yet to be fully understood. There are several potential mechanisms for how αTAT1 may access the acetylation site on the inside of the microtubule lumen: by copolymerization with tubulin at growing microtubule plus-ends [101], by transient openings in the lattice during microtubule breathing [83,86,102], or by microtubule end entry [74,84]. Copolymerization is not likely to be the primary mechanism for αTAT1 access, because stable microtubules are acetylated, and because αTAT1 is more active on polymerized microtubules than on free tubulin dimers [74,81–83 40,49,51–53]. Conversely, the other modes of access are possible [83,74,84]. Distinguishing among these possibilities is important for developing a mechanistic understanding to explain how αTAT1 could access its acetylation sites to facilitate microtubule acetylation.

In this work, we found that αTAT1 enters the microtubule lumen from the microtubule ends, and through breaks and bends in the lattice. Furthermore, our results support a model in which the mobility of αTAT1 within the lumen is controlled by the affinity of αTAT1 for its acetylation sites, which are highly concentrated inside of the microtubule lumen.

Results

αTAT1 is concentrated near to microtubule ends

To investigate the localization of αTAT1 binding to the microtubule, we used Total Internal Reflection Fluorescence (TIRF) microscopy to visualize the interactions of purified αTAT1-GFP protein (Fig. S2-1A) with GMPCPP-stabilized (non-dynamic), Rhodamine-labeled microtubules [83] (Fig. 2-1A and Supplemental Materials (Figs. S2-1B,D)). Qualitatively, we observed that αTAT1-GFP was concentrated near to the microtubule ends (Fig. 2-1B, top left, typical images). We quantified the microtubule images, and the corresponding green αTAT1-GFP fluorescence, by plotting the average red tubulin and green αTAT1-GFP fluorescence intensity as a function of the distance from the highest red fluorescence intensity (bright) microtubule end to the lowest red fluorescence intensity (dim) microtubule end (Fig. 2-1B, bottom left (red: microtubule; green: αTAT1-GFP). We then normalized the green αTAT1-GFP fluorescence intensity to its corresponding red microtubule fluorescence intensity at each microtubule position (Fig. 2-1B, bottom, grey markers). We found that αTAT1-GFP was concentrated at microtubule ends, and in particular on the “dim” end of the microtubule (Fig. 2-1B bottom left).

In the first set of experiments, it was clear from the fluorescence plots that the protofilaments at the end of the microtubules were generally similar lengths, leading to a relatively sharp drop in fluorescence at the microtubule tips (Fig. 2-1B, left, red). Therefore, to test whether αTAT1-GFP preferentially binds to exposed acetylation sites at the microtubule tip, we made microtubules with more tapered tips, relative to our initial blunt-tip microtubules, by allowing for a longer microtubule growth time [103]. In this case, the tapered ends would more readily expose the acetylation site due to increased variability in protofilament lengths, and thus allow us to distinguish whether the end preference was due in part to preferential binding of αTAT1-GFP to acetylation site-exposed protofilaments. As with the blunt-tip microtubules, αTAT1-GFP was introduced

to the imaging chamber with the cover-slip attached microtubules, and single-time-point images were collected using TIRF microscopy after steady-state αTAT1-GFP binding was achieved. Again, average red fluorescence intensity was plotted as a function of distance from the bright microtubule end to the dim microtubule end. In Fig. 2-1B (bottom right, n=104), note that the red fluorescence intensity drops off to background more slowly at the dim end as compared to in the blunt-tip microtubules (Fig. 2-1B left; 5μm microtubules shown; other microtubule lengths in Fig. S2-1C). Here, the "dim" end of the microtubule is likely composed of variable protofilament lengths [103–105], and thus may expose the internal microtubule lumen surface (Fig. 2-1B, inset). The corresponding αTAT1-GFP fluorescence intensity was then measured and plotted for the tapered-tip microtubules (Figure 2-1B bottom right, n=104). Importantly, the αTAT1-GFP localization to the dim microtubule end appeared to be more prominent on microtubules with tapered tips, suggesting that αTAT1 preferentially concentrates at microtubule ends with acetylation site-exposed protofilaments.

To confirm that αTAT1 binding was concentrated near to the microtubule ends, we conjugated purified, unlabeled αTAT1 (Fig. S2-1A) to 1.3 nm diameter gold beads, incubated the αTAT1-conjugated beads with GMPCPP-stabilized microtubules, and then imaged the microtubules using Transmission Electron Microscopy (TEM) (Supplemental Methods). The 1.3 nm diameter beads act as reporters for αTAT1 localization, but they should not limit access to the lumen because they are much smaller than the inner diameter of the microtubule (~15 nm). Consistent with the αTAT1-GFP fluorescence data, 86% of the observed αTAT1-conjugated bead clusters were located either at microtubule ends, or else at breaks or openings in the lattice (Fig. 2-1C; red arrows, ends; blue arrows, lattice opening).

Simulations suggest αTAT-GFP localization correlates with end-entry into the microtubule lumen

To investigate whether the experimentally observed αTAT1-GFP localization on stabilized microtubules could correlate with a lumen entry mechanism, we performed computational simulations of the αTAT1-microtubule interaction. Our simulations accounted for the (1) the model for αTAT1 entry into the lumen (end vs. lattice entry), (2) association and dissociation of αTAT1 with tubulin subunits on the external surface and internal luminal surface of the microtubule, and (3) diffusion of αTAT1 on the external surface of the microtubule and in solution within the lumen (Fig. 2-2A, supplemental

methods, Fig. S2-5). We constrained the model parameters either through experiments (Fig. S2-5), or, alternatively, by testing them over a range of values to ensure that model conclusions did not depend on narrowly defined parameter values (see Table S2-4 and Fig. S2-5). We found that the modeling results for αTAT1-GFP localization on the microtubule were most sensitive to the parameter γ, which controls the αTAT1 off-rate (affinity) on the luminal surface of the microtubule, as described below.

We first tested a microtubule "lattice entry" model in which simulated αTAT1 could bind the microtubule lattice, and then subsequently enter into the lumen regardless of its position along the microtubule (Fig. 2-2B), similar to "breathing" model in which transient lattice openings could routinely provide access for αTAT1 to enter the lumen along the length of the lattice. Using the lattice entry model, the simulated αTAT1-GFP localization data were not consistent with the experimentally observed localization of αTAT1-GFP at the microtubule tip (Fig. 2-2C). We ran this simulation for multiple values of *γ,* which is the relative affinity of αTAT1 for α-tubulin Lys40 acetylation sites on the inside surface versus the outside of the microtubule ($k_{off,lumen}=\gamma(k_{off,lattice})$). We found that the lattice entry model failed to explain the experimental data, independent of the value for *γ* (Fig. 2-2C).

Next, we used our simulations to test a microtubule "end entry" model, in which simulated αTAT1 could only enter the lumen through the microtubule ends (Fig. 2-2D). The simulated αTAT1-GFP localization data were consistent with the experimentally observed localization of αTAT1-GFP at the microtubule tip for $\gamma \leq 0.5$ (Fig. 2-2E), meaning that the simulated localization of αTAT1-GFP on stabilized microtubules was consistent with experiment if: (1) αTAT1 entered the lumen at microtubule ends, and (2) the simulated affinity of αTAT1 for its acetylation site on the luminal surface of the microtubule was ≥50% higher than for the outside of the lattice.

Thus, the results from these simulations suggest that the primary mode of αTAT1 entry into the lumen may be through the microtubule ends, and that the affinity of αTAT1 for the α-tubulin Lys40 acetylation sites within the lumen is higher than its affinity for the outside of the microtubule. However, our experimental αTAT1-GFP localization studies could not differentiate whether the αTAT1-GFP molecules were on the inside or the outside of the microtubule (Fig. 2-1B). Therefore, we used the simulation to predict the pattern of acetylation on the inside of a stabilized microtubule, as would be visualized using a fluorescent anti-acetylated tubulin antibody. We found that the lattice-entry model predicted uniformly distributed acetylated tubulin subunits along the length of the

microtubule (Fig. 2-2F, left-middle) because the αTAT1 molecules that entered the lumen along the length of the microtubule lattice were randomly localized along the inside of the microtubule (Fig. 2-2F, left-bottom cartoon). Conversely, we found that the end-entry simulation (using parameters that were consistent with the αTAT1-GFP localization data) predicted concentrated, short "bursts" of acetylation at microtubule ends (Fig. 2-2F, right-middle). This is because the αTAT1 molecules that entered the lumen through the microtubule ends tended to remain near to the microtubule ends (Fig. 2-2F, right-bottom cartoon).

In the end-entry αTAT1 simulation, the luminal αTAT1 molecules remained near to the microtubule ends because the simulated αTAT1 molecules exhibited very slow mobility inside of the microtubule lumen. While it is expected that αTAT1 should diffuse rapidly in solution, the concentration of α-tubulin Lys40 binding sites inside of the lumen is very high due to the small volume and dense packing of tubulin subunits inside the lumen (approximately 17 mM, see calculation, supplemental material). This high concentration of α-tubulin Lys40 binding sites within the lumen makes the effective on-rate for an individual αTAT1 molecule inside of a microtubule also very high. For example, we predict that the typical rebinding time for a free αTAT1 molecule inside the lumen will be $(1 / (k_{on}[\text{binding sites}])) = 6\text{x}10^{-5}$ sec (using a diffusion-limited biomolecular on-rate constant of $k_{on} = 1\ \mu M^{-1}s^{-1}$) [106]. As a result, we further predict that the root mean squared (RMS) travel distance for a free αTAT1 molecule prior to rebinding to an α-tubulin Lys40 acetylation site (Δx_{lumen}) is ~50 nm, where

$$< \Delta x_{lumen}^2 >^{1/2} = \sqrt{2 D_{lumen} \Delta t_{rebind}} \qquad (1)$$

in which D_{lumen} is the αTAT1 diffusion coefficient in solution (~$2.6\text{x}10^7$ nm^2/s) [84], and Δt_{rebind} is the typical rebinding time, as calculated above (~$6\text{x}10^{-5}$ sec). This predicted mean travel distance is similar to previous computational predictions [85].

Thus, the end-entry model for αTAT1 predicts that there will be bursts of acetylated tubulin near to the αTAT1 entry point at microtubule ends because the mobility of αTAT1 within the lumen is limited by rapid rebinding of luminal αTAT1 to nearby tubulin subunits (Fig. 2-2G). This led to two key predictions from the simulation that could be tested experimentally. First, if the "end-entry" model is correct, then acetylation should be most commonly observed near to the ends of the microtubules

where αTAT1 routinely enters the lumen. Second, if there is frustrated mobility of αTAT1 inside the microtubule lumen due to rapid rebinding, then concentrated “bursts” of microtubule acetylation should be observed, rather than a uniform dispersion of acetylation along the length of the microtubule (Fig. 2-2G).

Microtubule acetylation occurs in bursts that are preferentially localized at microtubule ends

We experimentally tested these simulation predictions by visualizing fluorescently labeled anti-acetylated tubulin antibodies on Rhodamine-labeled, GMPCPP-stabilized microtubules that had been acetylated by αTAT1 for 30 minutes in the microscope imaging chamber (Fig. 2-3A, left, see methods (bent and broken microtubules analyzed separately, see below)). We observed acetylation bursts at the ends of microtubules (Fig. 2-3A, right, top), similar to the simulation predictions for the end entry model (Fig. 2-2F, right, white arrow). The bursts, which were defined as an area of fluorescent antibody localization along the length of the microtubule lattice, averaged ~300 nm in length. This represents up to ~200 acetylated tubulin subunits (= ((300 nm -170 nm point spread function)/(8 nm/layer))*(13 subunits/layer)). Less frequently, we also observed bursts within the microtubule lattice (Fig. 2-3A, right, bottom). To quantify this observation, we calculated the burst frequency per site by normalizing the burst frequency to the number of available sites in each case, where end sites represented the last 128 nm (2 pixels) of a microtubule at each end, and lattice sites represented the remainder of the microtubule. Similar to the predictions from our simulation, we found that bursts were 15-fold more likely to occupy microtubule end sites than microtubule lattice sites (Fig. 2-3B, Binomial test $p<2X10^{-6}$).

To ensure that the antibody itself was not limited in its mobility to travel within the lumen, leading to an inability to detect acetylation along the length of the microtubules, we performed a positive control experiment. Here, dynamic microtubules were grown in the presence of αTAT1, in contrast to the stabilized microtubule experiments above, in which αTAT1 was added to pre-formed microtubules ((Fig. 2-3C, left), vs Fig. 2-3A). After 30 minutes of growth, the dynamic microtubules were then stabilized with Taxol, and imaged with the fluorescently labeled anti-acetylated tubulin antibody (Fig. 2-3C, left). We observed a population of microtubules that were uniformly labeled with antibody over their entire lengths (Fig. 2-3C, right, top), indicating that the antibody was indeed able to access a uniform proportion of the acetylated sites in the microtubules. To

quantify this observation, average line scans for similar length, fully acetylated microtubules in the positive controls were collected. We found that the antibody brightness was uniform along the length of the microtubule for the fully acetylated controls (Fig. 2-3C right, bottom), indicating that the fluorescent antibody brightness as visualized by TIRF microscopy was similar whether the antibody reported acetylated tubulin subunits near the ends of the microtubules, or inside of the lumen along the length of the microtubule.

Acetylation burst lengths increased slowly over time, while the fraction of acetylated microtubule ends increased more quickly over time

To test whether increased αTAT1 incubation time would increase the length or frequency of the acetylation bursts, we incubated stable, pre-formed microtubules with αTAT1 for times ranging from 20-120 minutes and then visualized the acetylation with fluorescent anti-acetylation antibody. We found that the largest increase over time was in the fraction of microtubules with at least one burst (Fig. 2-3D right, Logistic regression, $p=5X10^{-13}$), and we note that a similar trend was observed with increasing αTAT1 concentrations (Fig. S2-3). Additionally, we found that the acetylation bursts remained primarily at the microtubule ends at all of the sampled time points (Fig. 2-3D, left). Finally, we found that the mean burst length increased slowly over time (logistic regression of time points ≥ 5 min of the burst Length, p=0.151). Thus, increasing the αTAT1 incubation time (Fig. 2-3D) or concentration (Fig. S2-3) led to a higher overall acetylation level due primarily to an increased fraction of acetylated microtubule ends, consistent with an end entry model, and, secondarily, due to a slow increase in microtubule burst length, consistent with frustrated mobility of αTAT1 within the lumen.

If higher acetylation levels over time were due primarily to an increased number of acetylated microtubule ends, we reasoned that bulk acetylation levels would increase if the number of microtubule ends and/or lattice openings were increased by mechanical shearing and breaking of the microtubules. To test this prediction, we incubated Rhodamine-labeled GMPCPP-stabilized microtubules with unlabeled αTAT1 for 60 min., at which point we separated half of the mixture and sheared it using a small diameter needle. We then continued the αTAT1 incubation for both the sheared and unsheared mixtures for 120 min., at which point we re-sheared the previously sheared mixture. We then continued the incubation of both the sheared and unsheared mixtures for another 60 min (Fig. 2-3E, left). We quantified the acetylation levels at each time point for both

mixtures using western blots, and then normalized the anti-acetylation band intensities to the tubulin loading controls at each time point to account for loss of microtubules inside of the syringe during the shearing process (Fig. 2-3E, right; replicate experiment Fig. S2-1E). We found that the microtubules were slightly shorter, and the microtubule acetylation levels were slightly higher, in the 1X sheared mixture (120 min.) as compared to the unsheared controls (Fig. 2-3E). However, for the 2X sheared mixture (180 min.), the microtubules were substantially shorter, and the acetylation level substantially higher, than in the unsheared controls (Fig. 2-3E). This suggests that the microtubules were broken into smaller fragments by successive shearing, which increased the total number of microtubule ends and/or openings in the lattice, and thus allowed access for αTAT1 into the lumen on more microtubules. This then led to a higher bulk acetylation level, likely due to an increased fraction of luminal αTAT1 proteins [102]. Finally, we note that microtubules are depolymerized prior to detection of acetylation level by the antibody in western blots, and so access of the antibody itself to acetylation sites not a concern. Thus, the western blot results provide an independent confirmation of the fluorescent antibody results (Fig. 2-3A,B,D).

Microtubule acetylation is facilitated by new lattice openings

In addition to mechanical shearing, another method for allowing access of αTAT1 to the microtubule lumen may be by introducing large breaks or openings within the microtubule wall (Fig. 2-4A). Thus, we predicted that by opening up the closed tube, or by introducing breaks into the tube, this should also allow for increased numbers of acetylation bursts along the length of the microtubule lattice, and an increase in the bulk acetylation level of a microtubule population (Fig. 2-4B).

It has been previously demonstrated that opened, damaged microtubules can be created by briefly exposing GMPCPP microtubules to calcium [107]. Therefore, Rhodamine-labeled GMPCPP microtubules were briefly incubated with $CaCl_2$, and the $CaCl_2$-treated microtubules were imaged with TEM (Fig. 2-4C, top (supplemental methods)). From the TEM images, it was clear that portions of the GMPCPP microtubules were unraveled and damaged through the $CaCl_2$ treatment (Fig. 2-4C, top), which should allow increased access of αTAT1 to its acetylation site inside the microtubule lumen. Therefore, the $CaCl_2$ treated microtubules were incubated with αTAT1 in an imaging chamber for 30 min., and then acetylation was imaged with anti-acetylated tubulin antibody (Fig. 2-4C, bottom). We found that $CaCl_2$ treatment

substantially increased both the number of bursts per microtubule (Poisson regression $p<2.2X10^{-16}$), and the fraction of microtubules with bursts (Two sample test of proportions $p<2.2X10^{-16}$) (Fig. 2-4D; Fig. S2-2B).

To confirm that the anti-acetylated tubulin antibody was properly reporting the acetylation of $CaCl_2$-treated microtubules, we performed a parallel experiment using western blots. Acetylated tubulin levels were measured over time for control and $CaCl_2$-treated microtubules (Fig. 2-4E, top; Fig. S2-2A), and the normalized band intensities plotted as a function of αTAT1 incubation time (Fig. 2-4E, bottom). We found that the αTAT1 acetylation level after 60-120 minutes of αTAT1 incubation time was 3.7 fold higher for $CaCl_2$-treated microtubules as compared to control microtubules (Fig. 2-4E; green: $CaCl_2$, red: controls; Log transformed linear regression p=0.003), consistent with our fluorescence studies (Fig. 2-4D). In addition, we found that αTAT1 does not acetylate tubulin dimers as efficiently as it does intact microtubules, consistent with previous αTAT1 studies (Fig. 2-4E, blue)[82,84].

Together, these results are consistent with the prediction that αTAT1 relies on microtubule ends and breaks or openings in the microtubule lattice to allow access to the lumen, and that αTAT1 exhibits slow mobility within the lumen.

Slow depolymerization activity of αTAT1 may lead to microtubule-mediated cooperative binding of αTAT1

Our studies suggest that the overall microtubule acetylation rate is limited both by αTAT1 access to the lumen, and also by the mobility of αTAT1 once inside of the lumen. Thus, this raises the question of how it is that longer-lived microtubules tend to be increasingly acetylated inside of the cell [43,108]. Because our data suggests that microtubules with tapered ends have exposed α-tubulin Lys40 acetylation sites that allow for preferential αTAT1 targeting, we asked whether αTAT1 itself could perhaps contribute to generating these tapered microtubule ends on older, stabilized microtubules. To ask this question, we imaged coverslip-attached microtubules and generated average linescans of similar length, stabilized GMPCPP microtubules after 1 hour of treatment in buffer alone, and buffer with either acetyl-CoA, αTAT1, or αTAT1 and acetyl-CoA. Interestingly, treatments that included αTAT1 (either with or without acetyl-CoA) appeared to have modified tip structures, such that there was reduced fluorescence at the microtubule end, suggestive of more tapered microtubule tips (Fig. 2-5A, Buffer alone: n=92, Acetyl CoA: n=57, αTAT1: n=259, αTAT1+Acetyl coA: n=69).

This suggested that αTAT1 may be able to slowly "eat away" at microtubule ends to create tapered tips, leading to increased numbers of exposed acetylation sites in the presence of αTAT1. To quantify this effect, double-stabilized GMPCPP-Taxol microtubules were incubated with or without αTAT1 at 37 °C for 0 and 24 hours. Then, each group of microtubules were imaged using TIRF microscopy, and the mean microtubule lengths were measured in each case (Control: 0 Hour n=3626, 24 Hours n=1984, αTAT1:0 Hour n=513, 24 Hours n=215). Consistent with a slow depolymerization activity of αTAT1, the mean Taxol-GMPCPP microtubule length was reduced after 24 hours of αTAT1 treatment compared to controls (Fig. 2-5B, Log transformed two sample t-test, 0 Hour $p=0.029$, 24 Hours $p<2.2X10^{-16}$).

Because αTAT1 itself may act to create tapered tips, we speculated that this could lead to cooperative binding of αTAT1 on microtubules. Here, binding of the αTAT1 protein to the microtubule would tend to degrade the microtubule tip, and thus generate newly exposed α-tubulin Lys40 acetylation sites, which would then allow for additional αTAT1 targeting. Consistent with this idea, the integrated binding of αTAT1-GFP to microtubules after 1 hour of incubation appeared to increase cooperatively with increasing αTAT1-GFP concentration (Fig. 2-5C). Therefore, we speculate that because of its slow depolymerization activity, αTAT1 may bind to stable microtubules with blunt ends, but then over time the interaction of αTAT1 with microtubules may lead to increased acetylation site exposure at microtubule ends, and thus lead to increased acetylation of older, more stable microtubules (Fig. 2-5D).

Burst length increases with increasing salt concentration

Our results are consistent with a model in which αTAT1 exhibits slow, frustrated mobility inside of the microtubule lumen. This may be due to rapid rebinding of αTAT1 to densely packed acetylation sites. Therefore, we reasoned that if the αTAT1 rebinding rate was suppressed, then this should lead to increased αTAT1 mobility within the lumen, and subsequently to longer bursts of microtubule acetylation. Consistent with this hypothesis, our simulations predicted that larger RMS travel distances between rebinding events ($(<\Delta x_{lumen}>^2)^{1/2}$) for luminal αTAT1 molecules would lead to longer simulated acetylation bursts (Fig. 2-6A-C; supplemental methods).

It has been previously demonstrated that the binding affinity of αTAT1 for microtubules is suppressed at higher salt concentrations [61]. Therefore, if the slow

mobility of αTAT1 inside of the microtubule lumen is due to rapid, high affinity binding to densely packed tubulin subunits, we predicted that by adding salt during αTAT1 incubation, this could lead to longer acetylation burst lengths. Thus, we performed the acetylation-TIRF experiments, but by adding different concentrations of KCl during αTAT1 incubation. Strikingly, burst lengths were ~3-fold longer if the αTAT1 incubation was carried out at high salt conditions relative to our previous no-salt-added conditions (Fig. 2-6D-E), regardless of microtubule type (Two sample t-test, $p=5.2X10^{-12}$). This result supports a model in which the mobility of αTAT1 within the microtubule lumen is controlled by its affinity to the densely packed acetylation sites within the lumen (Fig. 2-6F).

Discussion

Based on our αTAT1-GFP localization data, computational simulations, biochemical experiments, and acetylation localization data, we conclude that the foremost mode of entry for αTAT1 into the microtubule lumen is through the microtubule ends, or through bends and breaks in the microtubule wall. This is in contrast to the model from Shida et al., which suggested that αTAT1 may access the microtubule lumen through lattice breathing at any position along the lattice [83], but is consistent with findings from Akella et al. in which the K40 acetylation signal formed a decreasing gradient that peaked at microtubule ends in axonemes [74]. We also found that once αTAT1 enters the microtubule lumen, it moves slowly down the lumen, and that this mobility is controlled by the affinity of αTAT1 for the highly concentrated α-tubulin acetylation sites within the lumen. This leads to concentrated “bursts” of microtubule acetylation at the ends of stable microtubules. Here, our study extends the work of Syzk et al. to examine the effect of microtubule structures and αTAT affinities on observed αTAT1 acetylation patterns (Extended discussion and comparison to work described in Syzk et al in Supplemental Material, Fig.S2-4).

Our results are consistent with a model in which αTAT1 stochastically enters microtubule ends. Thus, if αTAT1 never enters a microtubule end, the microtubule could remain unacetylated, even while nearby microtubules are partially or even fully acetylated. However, in stable microtubule networks where the $t_{1/2}$ of some microtubules is ~2.2 hours [109], such as in neurons, it is more likely that αTAT1 would ultimately enter the ends of a larger fraction of the microtubules, given their long lifetimes. Then, αTAT1 may be able to slowly acetylate the stable microtubules while traveling down lumen,

especially under high salt conditions such as is present inside of cells (Fig. 2-6F). In addition, we demonstrated that disruption of microtubule structure leads to an increase in microtubule acetylation (Fig. 2-4), and that acetylation often occurs at breaks in the microtubule lattice (Fig. 2-4A), suggesting that microtubule bending and breaking may provide secondary αTAT1 entry points to the lumen inside of cells. In cells, stable microtubule networks might naturally accumulate more lattice breaks because of their long lifetimes, and so this could also contribute to an increase in overall acetylation of stable microtubule networks, as well as to the discontinuous staining of acetylated tubulin as has been observed in cells[40,52,53,110,111].

Preferential targeting of αTAT1 to tapered microtubule tips could provide a mechanism for the specific acetylation of long-lived microtubules in cells. Because microtubules that have been growing for longer periods of time may be more likely to acquire tapered tip structures [37,103], αTAT1 may access the lumen more efficiently on older microtubules. Therefore, older microtubules would tend to be more acetylated than younger microtubules. This may play a role in the preferential acetylation of microtubules near to the plasma membrane [112]. Along with preferential recognition of older microtubules, αTAT1's slow microtubule depolymerization capability could allow for a positive feedback mechanism to allow the acetylation of older stable microtubules (Fig. 2-5D). In this case, αTAT1 would create its own binding template on a stabilized subset of microtubules in cells by slowly creating more tapered tips on the stable microtubules. This process may be especially important in neurons, where the stable microtubule network plays a vital role in maintaining cell shape and function; and where misregulation of microtubule acetylation has been linked to human disease [57,88,89,100].

Interestingly, αTAT1 is able to create tapered tip structures regardless of the presence of acetyl CoA. This suggests that αTAT1's depolymerization activity is simply due to αTAT1 interaction with the microtubule and not acetylation *per se*. Similar to this result, an acetylation-incompetent αTAT1 mutant has been shown to increase microtubule dynamics by destabilizing microtubules in cells [113]. Here, the slow depolymerization activity by αTAT1 may tend to induce catastrophe of dynamic microtubules, causing an overall increase in dynamics. In light of these findings, it will be important to tease apart the functional consequences of microtubule acetylation and αTAT1-microtubule interaction in different cell types or cellular structures.

Other cellular influences may also impact the efficiency of αTAT1 acetylation in vivo. For instance, Kalebic et al. found that αTAT1 auto-acetylation significantly

increases the catalytic activity of αTAT1. Here, auto-acetylation of αTAT1 could potentially increase the mobility of αTAT1 within the lumen, perhaps by suppressing the binding affinity of αTAT1 for its acetylation site [80]. Additionally, Montagnac et al. found that clathrin-coated pits localize αTAT1 to the ends of growing microtubules, which would subsequently increase the opportunity for αTAT1 to enter the lumen [112]. This led to stretches of acetylation near to the microtubule end, similar to what we observed in our *in vitro* studies. Thus, factors that localize αTAT1 to microtubule plus-ends could also increase the efficiency of αTAT1 acetylation in vivo.

In summary, our data support a model in which αTAT1 stochastically enters the lumen at microtubule ends, or through breaks in the lattice. Then, the mobility of αTAT1 within the lumen is frustrated and controlled by the affinity of αTAT1 for its binding sites, which are highly concentrated within the lumen. Important future efforts will involve identifying regulators of αTAT1 that could facilitate its end entry and luminal mobility, as well as studies to determine whether αTAT1 itself could potentially modulate microtubule dynamics to allow access to the lumen.

Acknowledgements

The authors thank Taylor Reid for image analysis assistance and Brandon Coombes for statistical analysis assistance. CEC is funded by the American Heart Association Predoctoral Fellowship. MKG is supported by the Pew Charitable Trusts through the Pew Scholars Program in the Biomedical Sciences, and by National Institutes of Health grant NIGMS GM-103833. Parts of this work were carried out in the Characterization Facility, University of Minnesota, a member of the NSF-funded Materials Research Facilities Network (www.mrfn.org) via the MRSEC program.

Figures

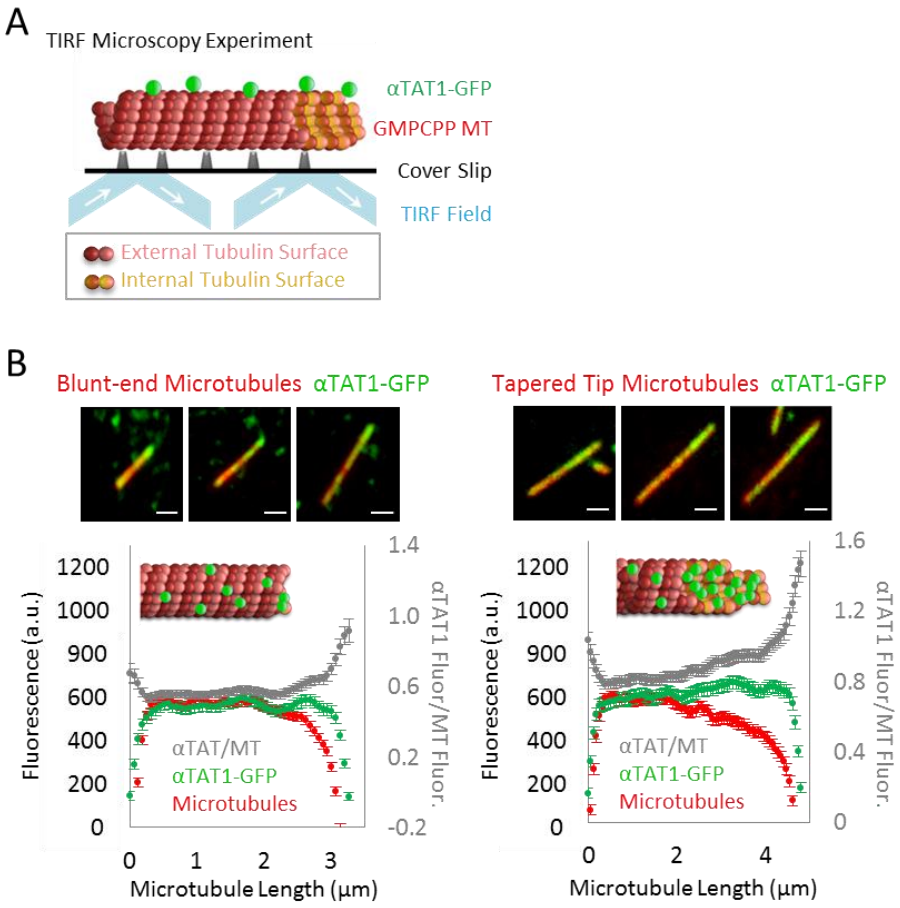
A
TIRF Microscopy Experiment
αTAT1-GFP
GMPCPP MT
Cover Slip
TIRF Field
External Tubulin Surface
Internal Tubulin Surface
B
Blunt-end Microtubules αTAT1-GFP
Tapered Tip Microtubules αTAT1-GFP
Fluorescence (a.u.)
αTAT1 Fluor/MT Fluor.
αTAT/MT
αTAT1-GFP
Microtubules
Microtubule Length (μm)
C
Electron Microscopy Experiment
1.3 nm αTAT1 Conjugated Bead
Tip Localized
Open Lattice

Figure 2-1: αTAT1 preferentially targets the dim microtubule ends of GMPCPP stabilized microtubules. (A) TIRF microscopy experiments to characterize αTAT1-GFP localization on microtubules. (B) Top: typical images of αTAT1-GFP binding (green) to Rhodamine-labeled GMPCPP microtubules (red). (scale bar: 1 μm) Bottom: Quantitative average fluorescence line scans indicating the localization of αTAT1-GFP on blunt microtubules (left, n=126 microtubules) and extended microtubules (right, n=104 microtubules) (Error bars 95% confidence intervals; green markers are αTAT-GFP intensity (grey) normalized to microtubule intensity (red) at each position). Data from other microtubule lengths shown in Fig. S2-1C. Microtubules were computationally aligned during the MATLAB image analysis based on the red microtubule fluorescence intensity, such that the higher red intensity microtubule end was assigned to position 0 μm (left), and the lower intensity (dimmer) red end was assigned to position 5 μm for all microtubules (right). Inset cartoon demonstrates the preferential localization of αTAT1-GFP to the dim microtubule end, which is likely composed of variable protofilament lengths, and thus exposes the internal microtubule lumen surface. (C) TEM images of αTAT1 conjugated to 1.3 nm gold bead (red arrows: αTAT bead clusters at tips; blue arrows: bead at open microtubule lattice) (scale bars 25 nm).

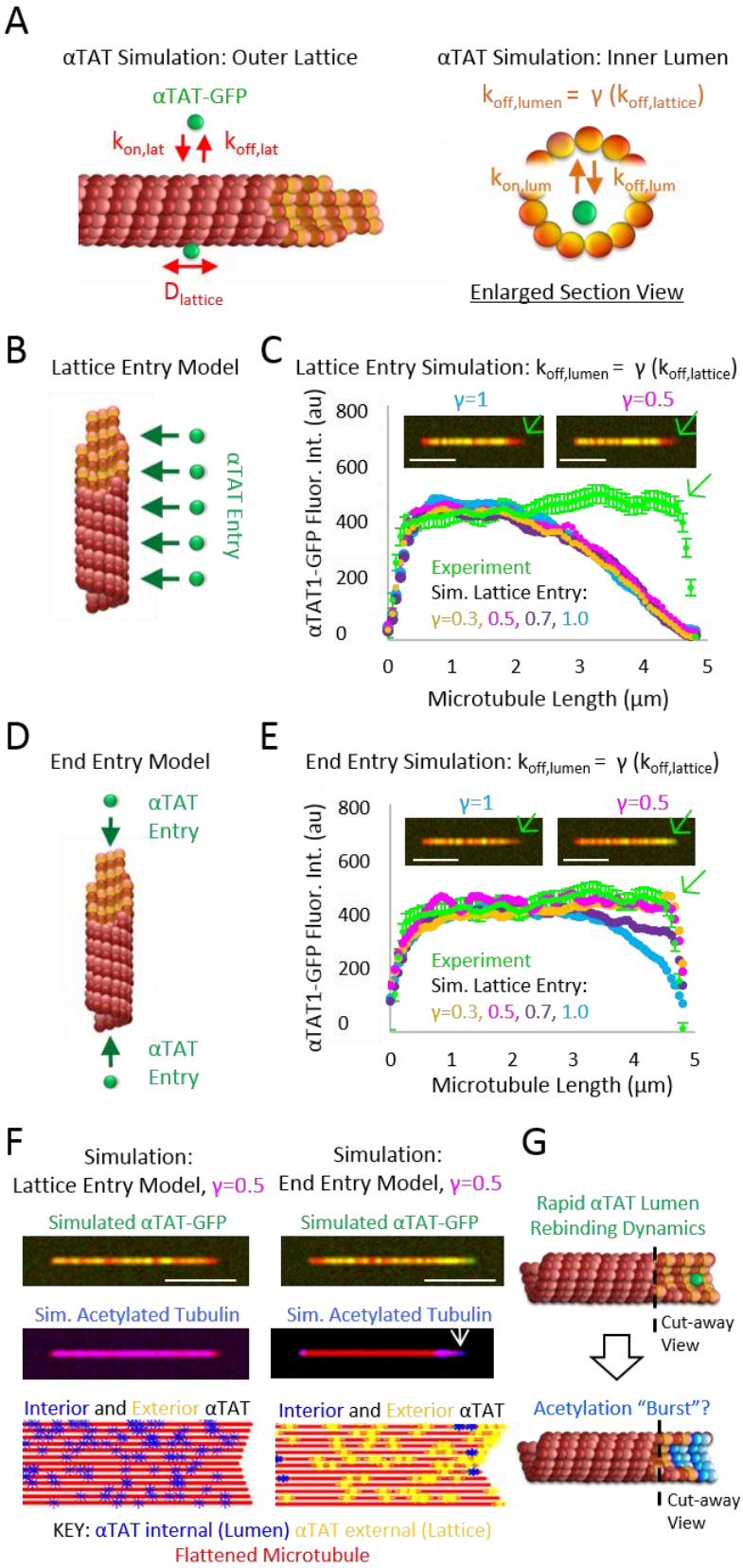
A
αTAT Simulation: Outer Lattice
αTAT-GFP
$k_{on,lat}$
$k_{off,lat}$
$D_{lattice}$
αTAT Simulation: Inner Lumen
$k_{off,lumen} = \gamma\ (k_{off,lattice})$
$k_{on,lum}$
$k_{off,lum}$
Enlarged Section View
B
Lattice Entry Model
αTAT Entry
C
Lattice Entry Simulation: $k_{off,lumen} = \gamma\ (k_{off,lattice})$
γ=1
γ=0.5
αTAT1-GFP Fluor. Int. (au)
800
600
400
200
0
Experiment
Sim. Lattice Entry:
γ=0.3, 0.5, 0.7, 1.0
0 1 2 3 4 5
Microtubule Length (μm)
D
End Entry Model
αTAT Entry
αTAT Entry
E
End Entry Simulation: $k_{off,lumen} = \gamma\ (k_{off,lattice})$
γ=1
γ=0.5
αTAT1-GFP Fluor. Int. (au)
800
600
400
200
0
Experiment
Sim. Lattice Entry:
γ=0.3, 0.5, 0.7, 1.0
0 1 2 3 4 5
Microtubule Length (μm)
F
Simulation:
Lattice Entry Model, γ=0.5
Simulation:
End Entry Model, γ=0.5
Simulated αTAT-GFP
Simulated αTAT-GFP
Sim. Acetylated Tubulin
Sim. Acetylated Tubulin
Interior and Exterior αTAT
Interior and Exterior αTAT
KEY: αTAT internal (Lumen) αTAT external (Lattice)
Flattened Microtubule
G
Rapid αTAT Lumen
Rebinding Dynamics
Cut-away
View
Acetylation "Burst"?
Cut-away
View

Figure 2-2: Simulations predict differential acetylation patterns based on αTAT1 lumen entry model. (A) Rules for αTAT1 simulation, which includes movement and binding of αTAT1 on the internal and external surfaces of the microtubules. Key parameters are as shown, with a detailed description of parameter value assignment in Table S4 and Fig. S5. The simulated αTAT1-GFP localization is most sensitive to the parameter γ, which controls the αTAT1 off-rate on the luminal surface of the microtubule (small γ = high affinity lumen binding, larger γ = low affinity lumen binding). (B) In the simulated αTAT1 "lattice entry" model, αTAT1 is able to randomly enter the lumen at any point along the microtubule. However, as shown in (C), the lattice-entry model does not reproduce experimental αTAT1-GFP localization results (experimental data reproduced from Fig. 1B), regardless of the value for γ. Green arrow: simulated αTAT1-GFP is not concentrated at dim microtubule end in the lattice entry model. (D) In the simulated αTAT1 "end entry" model, αTAT1 is only able to enter the microtubule lumen from its ends. As shown in (E), the end-entry model reproduces experimental αTAT1-GFP localization results if γ≤0.5, such that αTAT1 has a 50% lower off-rate (higher affinity) on the interior surface of the microtubule relative to the outside surface (experimental data reproduced from Fig. 1B). Green arrow: αTAT1-GFP is localized to the dim microtubule end in the end entry model when γ≤0.5. (F) Simulated αTAT1-GFP localization (Top) and the resulting distribution of acetylated tubulin (middle), when using the lattice entry model (left) and end entry model (right). During these simulations, every acetylation site on the inside of the microtubule lumen was non-acetylated at the start of the simulation, and then every acetylation site that was visited by an αTAT1 molecule during the simulation was acetylated. In addition, for simplicity it was assumed that the affinity (on and off rates) of αTAT1 were identical whether or not a tubulin subunit was acetylated. Note that the end-entry model predicts "bursts" of acetylated tubulin at the microtubule ends (white arrow, right). This is because αTAT1 is distributed throughout the lumen for the lattice entry model (left, bottom, graphical output at completion of simulation), while for the end-entry model, αTAT1 which has entered the lumen is concentrated at the microtubule ends (right, bottom, graphical output at completion of simulation). (G) Cartoon summarizing simulation predictions: luminal αTAT1 (green) diffuses in solution, but rapidly rebinds to nearby tubulin subunits, and so αTAT1 moves slowly down the lumen (top). As a result, the simulation predicts "bursts" of acetylated tubulin near to the microtubule end (bottom, blue: acetylated subunits) (scale bars all images, 3 μm).

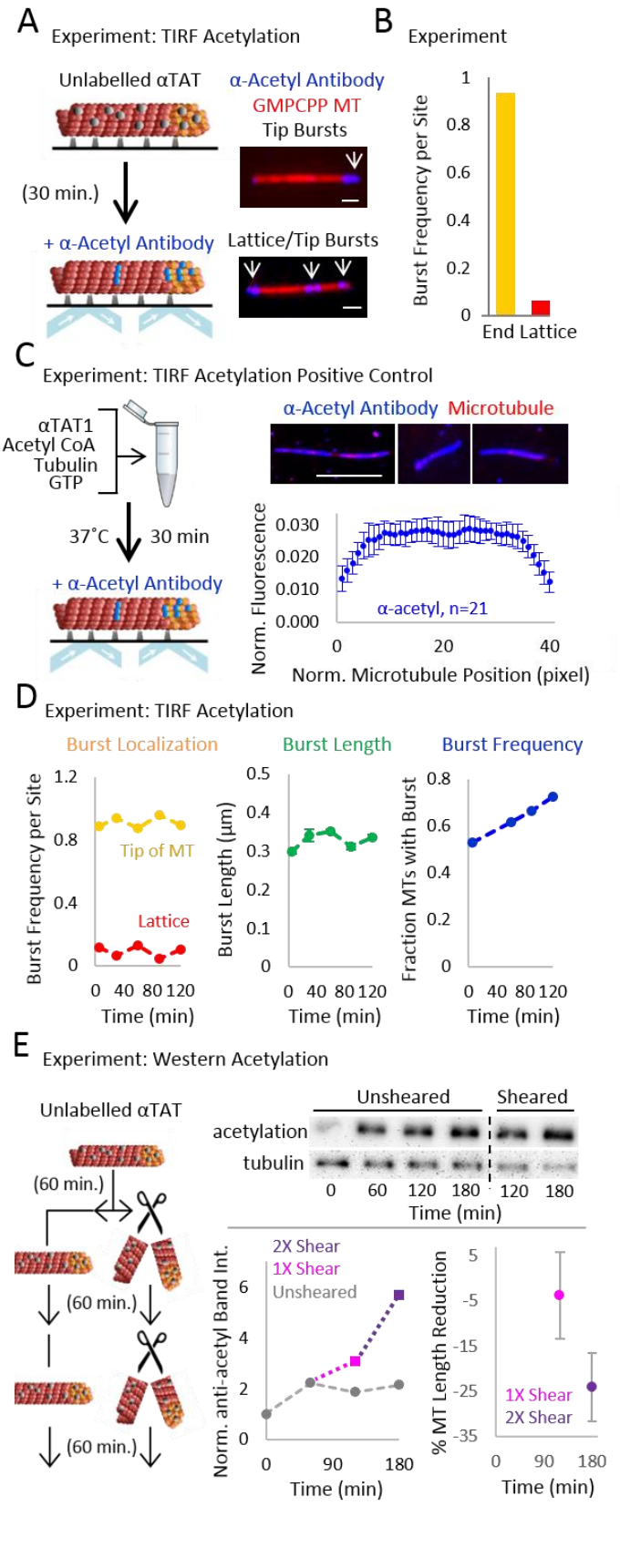
A
Experiment: TIRF Acetylation
Unlabelled αTAT
α-Acetyl Antibody
GMPCPP MT
Tip Bursts
(30 min.)
+ α-Acetyl Antibody
Lattice/Tip Bursts
B
Experiment
Burst Frequency per Site
1
0.8
0.6
0.4
0.2
0
End Lattice
C
Experiment: TIRF Acetylation Positive Control
αTAT1
Acetyl CoA
Tubulin
GTP
37˚C
30 min
+ α-Acetyl Antibody
α-Acetyl Antibody
Microtubule
Norm. Fluorescence
0.030
0.020
0.010
0.000
α-acetyl, n=21
0
20
40
Norm. Microtubule Position (pixel)
D
Experiment: TIRF Acetylation
Burst Localization
Burst Length
Burst Frequency
Burst Frequency per Site
1.2
0.8
0.4
0
Tip of MT
Lattice
0 40 80 120
Time (min)
Burst Length (μm)
0.5
0.4
0.3
0.2
0.1
0
0 40 80 120
Time (min)
Fraction MTs with Burst
0.8
0.6
0.4
0.2
0
0 40 80 120
Time (min)
E
Experiment: Western Acetylation
Unlabelled αTAT
(60 min.)
(60 min.)
(60 min.)
Unsheared
Sheared
acetylation
tubulin
0 60 120 180 120 180
Time (min)
Norm. anti-acetyl Band Int.
2X Shear
1X Shear
Unsheared
6
4
2
0
0 90 180
Time (min)
% MT Length Reduction
5
-5
-15
-25
-35
1X Shear
2X Shear
0 90 180
Time (min)

Figure 2-3: Acetylation occurs in bursts, which are preferentially localized at microtubule ends. (A) Left: Schematic of Acetylation TIRF experiment: pre-formed and cover-slip adhered GMPCPP microtubules were incubated in the imaging chamber with unlabeled αTAT1, and then subsequently labeled with fluorescent α-acetylated tubulin antibody to detect acetylation patterns. Right: Typical images of acetylated microtubules: blue acetylation "bursts" were observed at microtubule ends (top), and occasionally along the length of the microtubule (bottom) (scale bar 1 μm) (B) Burst frequency per site, where bursts that occupied the first two pixels (128 nm) from each microtubule end occupied a "tip" site, and bursts occupying any other pixels along the microtubule were "lattice" sites (n=426 microtubules). Acetylation bursts were 15-fold more likely to occupy microtubule end sites than microtubule lattice sites. (C) Left: Schematic of positive control assay: dynamic microtubules were grown in the presence of αTAT1, and then labeled with fluorescent α-acetyl antibody. Right: (Top) typical images of fully acetylated microtubules, which were not observed in experiments from (A) (scale bar 3 μm). Bottom: quantification of average α-acetyl antibody fluorescence along the length of fully acetylated microtubules of similar length. The fluorescence was similar regardless of location on the microtubule. (D) Acetylation TIRF experimental results on pre-formed, stabilized microtubules with increasing amounts of αTAT1 incubation time. The number of microtubules with bursts increases most substantially with increased αTAT1 incubation time (right; Logistic regression, p=5X10-13). One sided test of Burst Localization proportions show that none are significantly different from each other (left; 30 min p=1, 60 min p=0.46, 90 min p=1, 120 min p=0.96). Logistic regression of time points ≥ 5 min of the Burst Length (center; p=0.151). (Burst Localization (left) and Burst Length (center): n ≥340 each time point; Burst Frequency (right): n≥470 each time point) (E) Left: Schematic for experiment to test the effect of microtubule shearing on acetylation rate, analyzed by western blot. Right: results for one experiment (replication results, Fig. S2-1E). Acetylation level is increased upon shearing, while microtubule lengths are decreased. Note that acetylation levels are normalized to the tubulin loading control to account for loss of microtubules in the syringe during the shearing process (Error bars in all panels are 95% confidence intervals).

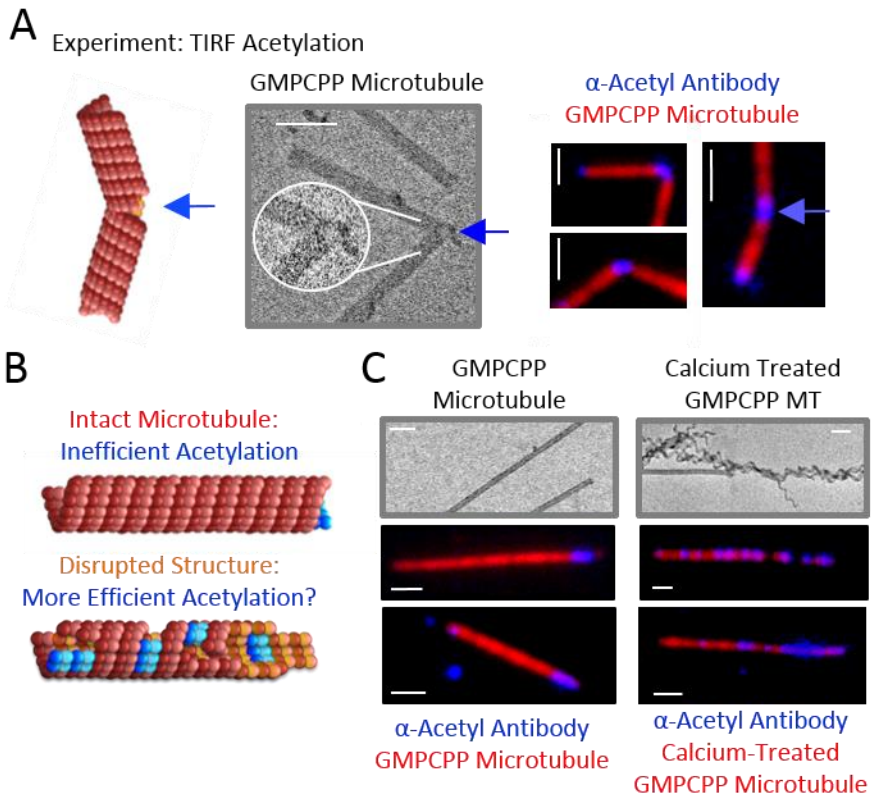
A
Experiment: TIRF Acetylation
GMPCPP Microtubule
α-Acetyl Antibody
GMPCPP Microtubule
B
Intact Microtubule:
Inefficient Acetylation
Disrupted Structure:
More Efficient Acetylation?
C
GMPCPP
Microtubule
Calcium Treated
GMPCPP MT
α-Acetyl Antibody
GMPCPP Microtubule
α-Acetyl Antibody
Calcium-Treated
GMPCPP Microtubule
D
Experiment: TIRF Acetylation
Number of Bursts per MT
2.5
2
1.5
1
0.5
0
***
Control
Calcium
Fraction MTs with Burst
0.8
0.6
0.4
0.2
0
***
Control
Calcium
E
Experiment: Western Acetylation
α-acetyl tubulin
Ca
MTs
Dim. MTs
0
10
20
40
60
90
Time (min)
Calcium-Treated Microtubule
Microtubule
Dimers
Norm. α-acetyl
tubulin intensity
40
20
0
0
50
100
Time (min)

Figure 2-4: Disruption of microtubule structure is correlated with higher acetylation rates. (A) Acetylation bursts frequently occurred at bends and breaks in the GMPCPP microtubules Left: schematic and TEM image of microtubule break at a bend (scale bar 100 nm). Right: acetylation-TIRF microscopy images of bent microtubules (scale bar 1 μm). (B) If αTAT1 typically enters the microtubule through its ends (top), then the presence of new openings in the lattice may increase acetylation rate (bottom) (C) Top: TEM images of GMPCPP microtubules (left), and $CaCl_2$ treated GMPCPP microtubules (right) (scale bar 100 nm). $CaCl_2$ treated GMPCPP microtubules have disrupted structure. Bottom: TIRF microscopy images of acetylated GMPCPP and $CaCl_2$ treated GMPCPP microtubules (scale bars 1μm). (D) Left: mean number of bursts per microtubule in control vs $CaCl_2$ treated microtubules (control: n=3533, SD=0.98, $CaCl_2$: n=2540, SD=1.46), and Right: the fraction of microtubules which have at least one burst (control: n=3533, $CaCl_2$: n=2540). Both are increased with $CaCl_2$ treatment (see also Fig. S2-2B). (E) The increase in acetylation level over time was measured for controls and $CaCl_2$ treated microtubules via western blot. Top: representative western blots of acetylated dimers, GMPCPP microtubules, and $CaCl_2$ treated GMPCPP microtubules taken after 0-90 minutes of αTAT1 incubation (see also Fig. S2-2A). Bottom: Normalized western band intensities; all experimental data points shown on graph).

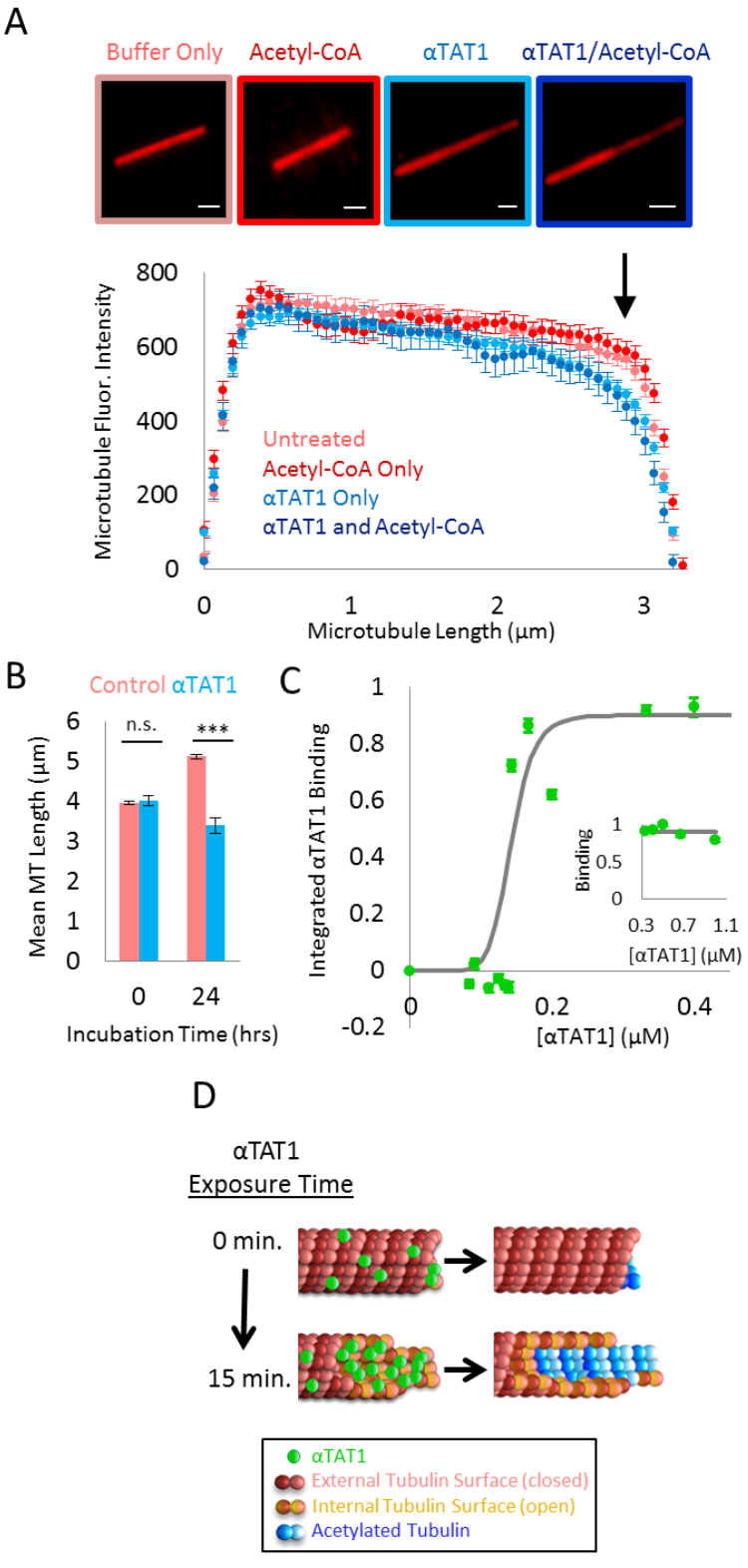
A
Buffer Only
Acetyl-CoA
αTAT1
αTAT1/Acetyl-CoA
Microtubule Fluor. Intensity
800
600
400
200
0
Untreated
Acetyl-CoA Only
αTAT1 Only
αTAT1 and Acetyl-CoA
0
1
2
3
Microtubule Length (μm)
B
Control αTAT1
n.s.
***
Mean MT Length (μm)
6
5
4
3
2
1
0
0
24
Incubation Time (hrs)
C
Integrated αTAT1 Binding
1
0.8
0.6
0.4
0.2
0
-0.2
0
0.2
0.4
[αTAT1] (μM)
Binding
1
0.5
0
0.3
0.7
1.1
[αTAT1] (μM)
D
αTAT1
Exposure Time
0 min.
15 min.
αTAT1
External Tubulin Surface (closed)
Internal Tubulin Surface (open)
Acetylated Tubulin

Figure 2-5: Slow depolymerization activity of αTAT1 may lead to microtubule-mediated cooperative binding of αTAT1. (A) Top: example TIRF microscopy images of GMPCPP microtubules with and without αTAT1 and acetyl CoA (scale bars 1 μm). Bottom: quantitative analysis of microtubule fluorescence with and without αTAT1 and acetyl CoA shows increased microtubule end tapering with αTAT1 present (Untreated: n=92, Acetyl coA: n=57, αTAT1: n=259, αTAT1+Acetyl coA: n=69). (B) Mean double-stabilized microtubule lengths after incubation with and without αTAT1 (Control: 0 Hour n=3626, 24 Hour n=1984, αTAT1:0 Hour n=513, 24 Hour n=215). (C) Integrated binding of αTAT1-GFP to microtubules after 1 hour of incubation appears to increase cooperatively with increasing αTAT1-GFP concentration (Hill coefficient = 9). (D) αTAT1 may bind to the blunt ends of microtubules (top), but then over time, the interaction of αTAT1 with microtubules may lead to increased acetylation site exposure at microtubule ends (bottom), and thus lead to cooperative targeting of αTAT1 to microtubule ends (bottom, green).

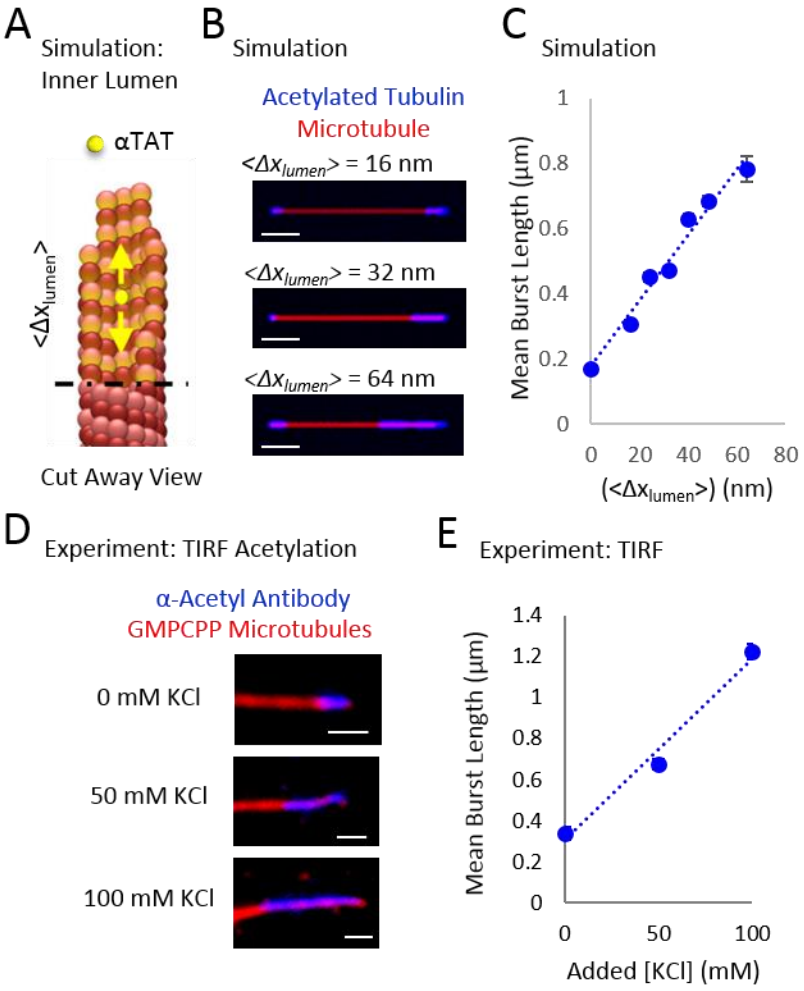
A
Simulation:
Inner Lumen
αTAT
<Δx_lumen>
Cut Away View
B
Simulation
Acetylated Tubulin
Microtubule
<Δx_lumen> = 16 nm
<Δx_lumen> = 32 nm
<Δx_lumen> = 64 nm
C
Simulation
Mean Burst Length (μm)
0
0.2
0.4
0.6
0.8
1
0
20
40
60
80
(<Δx_lumen>) (nm)
D
Experiment: TIRF Acetylation
α-Acetyl Antibody
GMPCPP Microtubules
0 mM KCl
50 mM KCl
100 mM KCl
E
Experiment: TIRF
Mean Burst Length (μm)
0
0.2
0.4
0.6
0.8
1
1.2
1.4
0
50
100
Added [KCl] (mM)
F
High αTAT1 Affinity
(Low Salt)
αTAT1
Entry
Low αTAT1
Mobility
Cut-away
View
Acetylation "Burst"
Low αTAT1 Affinity
(High Salt)
αTAT1
Entry
High αTAT1
Mobility
Cut-away
View
Acetylation "Burst"

Figure 2-6: Reduced binding affinity of αTAT1 for microtubules leads to increased mobility within the lumen, and therefore increased acetylation burst lengths. (A) Schematic of αTAT1 movement inside of the microtubule lumen. Yellow arrows represent the diffusive mobility of αTAT1 within the lumen, which is described by the variable $<\Delta x_{lumen}>$, the RMS αTAT1 travel distance between binding events. (B) Simulated TIRF microscopy images of acetylation bursts with increasing $<\Delta x_{lumen}>$ for αTAT1 (scale bar 1 μm, see supplemental methods). (C) Simulations predict that burst lengths will increase with increased travel distance between binding events for luminal αTAT1 (e.g., for increasing $<\Delta x_{lumen}>$), as would be expected if the affinity of αTAT1 for its binding sites was reduced. (D). Example TIRF microscopy images from experiments with increasing added KCl concentration during αTAT1 incubation (KCl concentrations added to Brb80 buffer). (E) Burst lengths increase at higher KCl concentrations (n≥426 each concentration; rrror bars 95% confidence intervals) (F) Model for acetylation of stable microtubules in low (left) and high (right) salt. Top: αTAT1 enters at the ends of microtubules. Bottom Left: αTAT1 has high affinity to the luminal surface in low salt and thus has slow mobility to travel down the microtubule lumen, creating short bursts of acetylation at microtubule ends. Bottom Right: αTAT1 would have lower affinity to the luminal wall in high salt conditions, and would move more efficiently within the lumen. High salt conditions, such as within a cellular environment, would allow for gradual acetylation of stable microtubules over time.

Supplemental Material and Methods

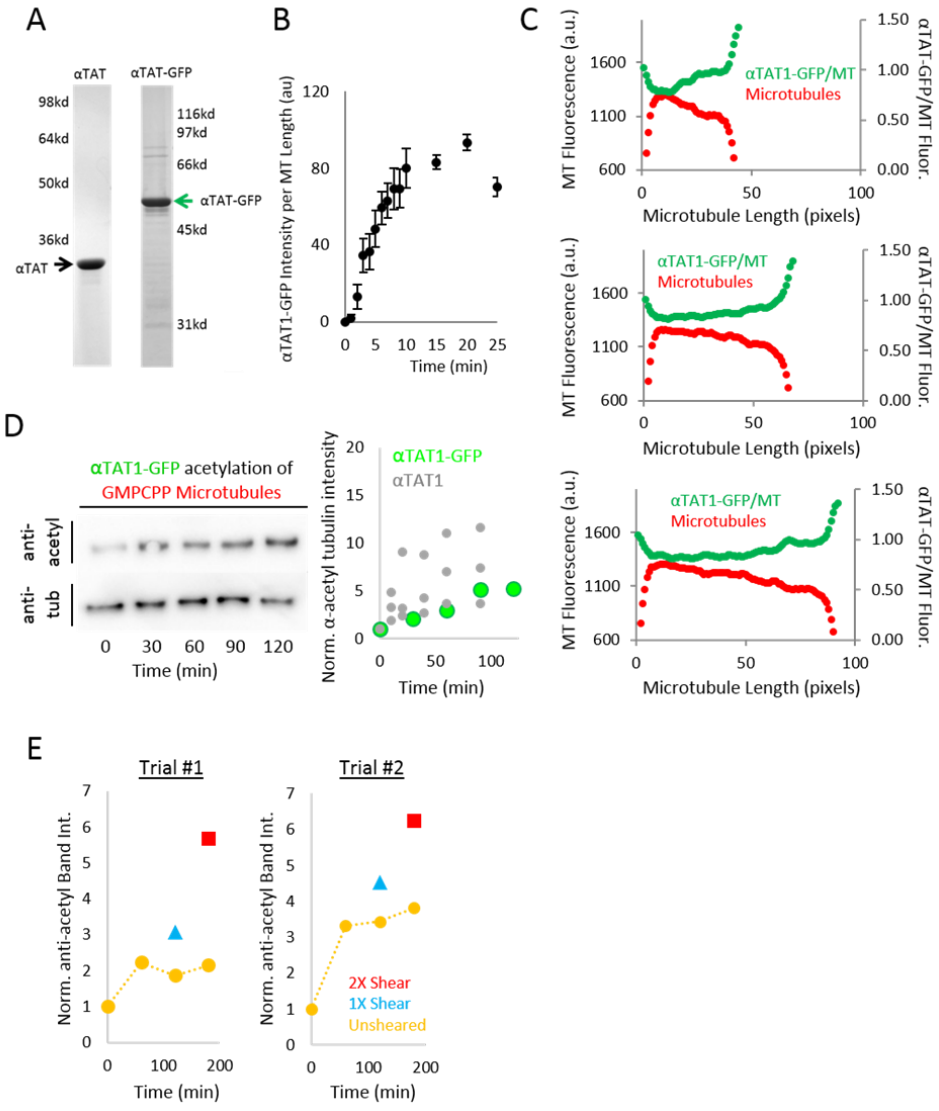

Figure S2-1: Additional Experimental Data and Verification (A) Human αTAT1 and αTAT1-GFP protein was expressed and purified from *E. coli* cells. The two cropped Coomassie Gels demonstrate the purity of the αTAT1 and αTAT1-GFP preparations. (B) Quantitative analysis of αTAT1-GFP fluorescence intensity measured per microtubule length over increasing amounts of time after αTAT1-GFP addition to the imaging chamber (n>100 for each time point). (C) αTAT1-GFP (green) and microtubule (red) fluorescence intensity as a function of position for different microtubule lengths (D) Left: GMPCPP microtubules were acetylated with αTAT1-GFP and measured from 0 to 120 minutes using western blots. Right: αTAT1-GFP and αTAT1 acetylate GMPCPP microtubules at similar rates. (E) Repeats of the western shearing experiment in Fig. 2-3D. Trial #1 is shown in the main text figure, and reproduced here.

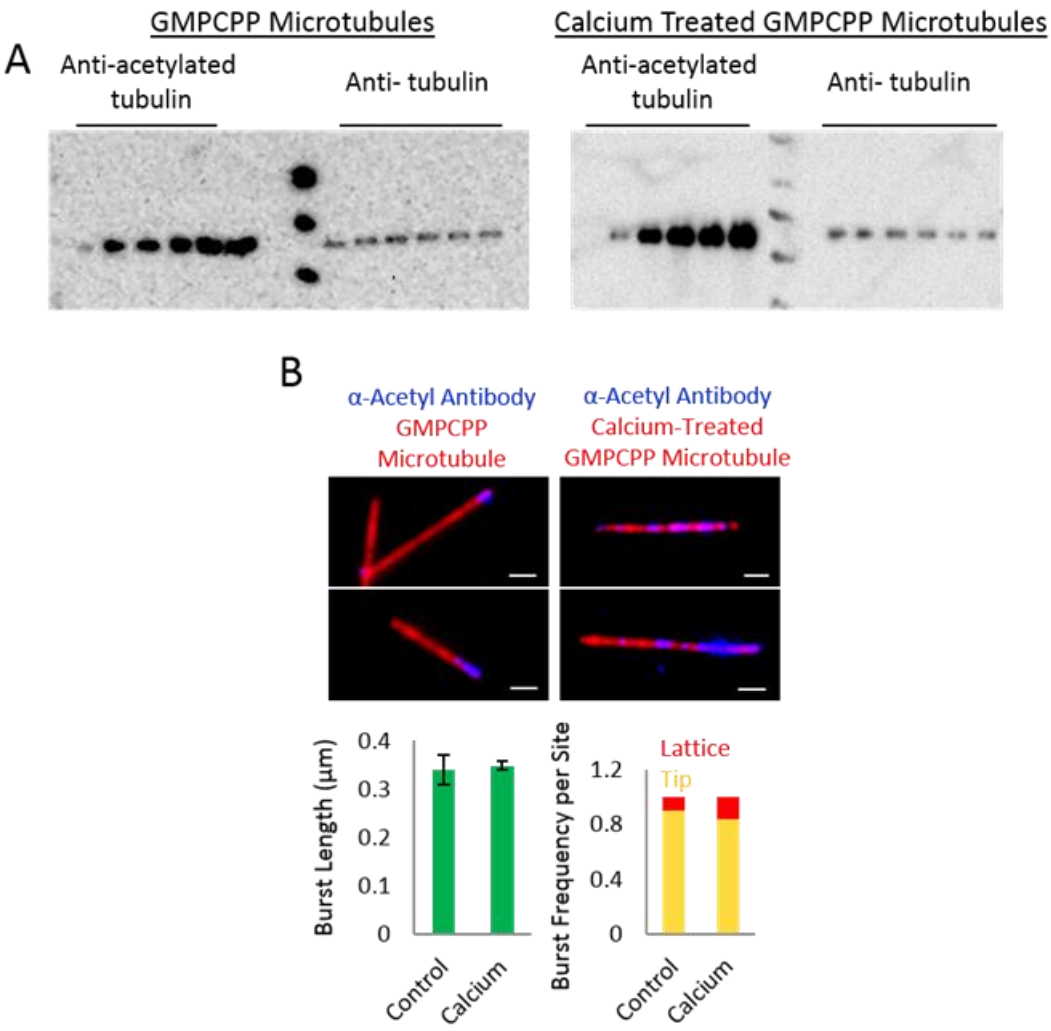
A
GMPCPP Microtubules
Anti-acetylated tubulin
Anti- tubulin
Calcium Treated GMPCPP Microtubules
Anti-acetylated tubulin
Anti- tubulin
B
α-Acetyl Antibody GMPCPP Microtubule
α-Acetyl Antibody Calcium-Treated GMPCPP Microtubule
Burst Length (μm)
0.4
0.3
0.2
0.1
0
Control
Calcium
Burst Frequency per Site
1.2
0.8
0.4
0
Lattice
Tip
Control
Calcium

Figure S2-2: Acetylation of Microtubules. (A) Acetylation rates of intact GMPCPP microtubules and calcium-treated GMPCPP microtubules were compared using western blots. Western blots of acetylated microtubules and calcium treated microtubules demonstrate an increased acetylation rate on calcium treated microtubules. (B) Effect of calcium treatment on burst length and burst localization in our acetylation TIRF experiment was assessed. Only small differences were found between GMPCPP microtubules and calcium treated GMPCPP microtubules. (Control: n= 426, Calcium: n= 1307, Burst Length: Log transformed two sample t-test $p=1X10^{-7}$, Burst Frequency per Site: Two sample test of proportions p=0.003)

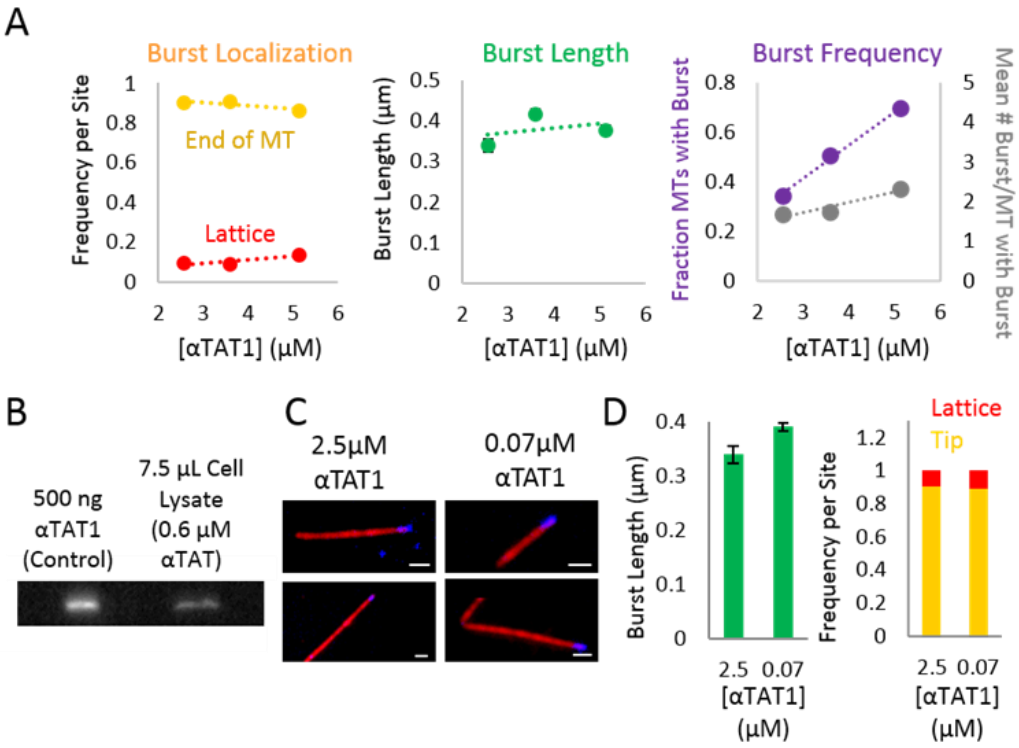
A
Burst Localization
Frequency per Site
End of MT
Lattice
[αTAT1] (μM)
Burst Length
Burst Length (μm)
[αTAT1] (μM)
Burst Frequency
Fraction MTs with Burst
Mean # Burst/MT with Burst
[αTAT1] (μM)
B
500 ng αTAT1 (Control)
7.5 μL Cell Lysate (0.6 μM αTAT)
C
2.5μM αTAT1
0.07μM αTAT1
D
Burst Length (μm)
Frequency per Site
Lattice
Tip
2.5 0.07
[αTAT1] (μM)
2.5 0.07
[αTAT1] (μM)

Figure S2-3: Effect of αTAT1 Concentration on Acetylation Bursts. (A) To test the effect of αTAT1 concentration on acetylation bursts in our TIRF assay, analysis of burst localization, burst length, and burst frequency was performed for increasing concentrations of αTAT1. There was a small but significant effect of concentration on burst localization and burst length (2.5 μM αTAT1: n=426, 3.6 μM αTAT1: n=735, 5.1 μM αTAT1: n=1139, Burst Frequency per Site: Logistic regression p=0.010, Burst Length: Log transformed linear regression $p=6.8X10^{-5}$). However, the fraction of microtubules with at least one burst and the mean number of bursts substantially increase as αTAT1 concentration increases (2.5 μM αTAT1: n=3533, 3.6 μM αTAT1: n=4831, 5.1 μM αTAT1: n=4202, Fraction of MTs with a Burst: Logistic regression $p<2X10^{-16}$, Mean Number Bursts: Poisson regression $p<2X10^{-16}$). (B) The concentration of αTAT1 in human RPE cells was approximated by western blot. Known concentrations of αTAT1 were blotted with an anti- αTAT1 antibody alongside cell lysate. The approximate concentration of αTAT1 in cells was 0.6 μM, which is within the range of concentrations used in our *in vitro* experiments (C) To surround the in vivo concentration range, a comparison of burst lengths and burst localization with 2.5 μM αTAT1 and 0.07 μM αTAT1 was assessed using the acetylation TIRF assay. (D) Burst lengths increased slightly with 0.07 μM αTAT1 (Log transformed two sample t-test $p=6.7X10^{-15}$) while burst locations were not affected by dropping the αTAT1 concentration (Two sample test of proportions p=0.752, 2.5μM αTAT1: n=426, 0.07μM αTAT1: n=923).

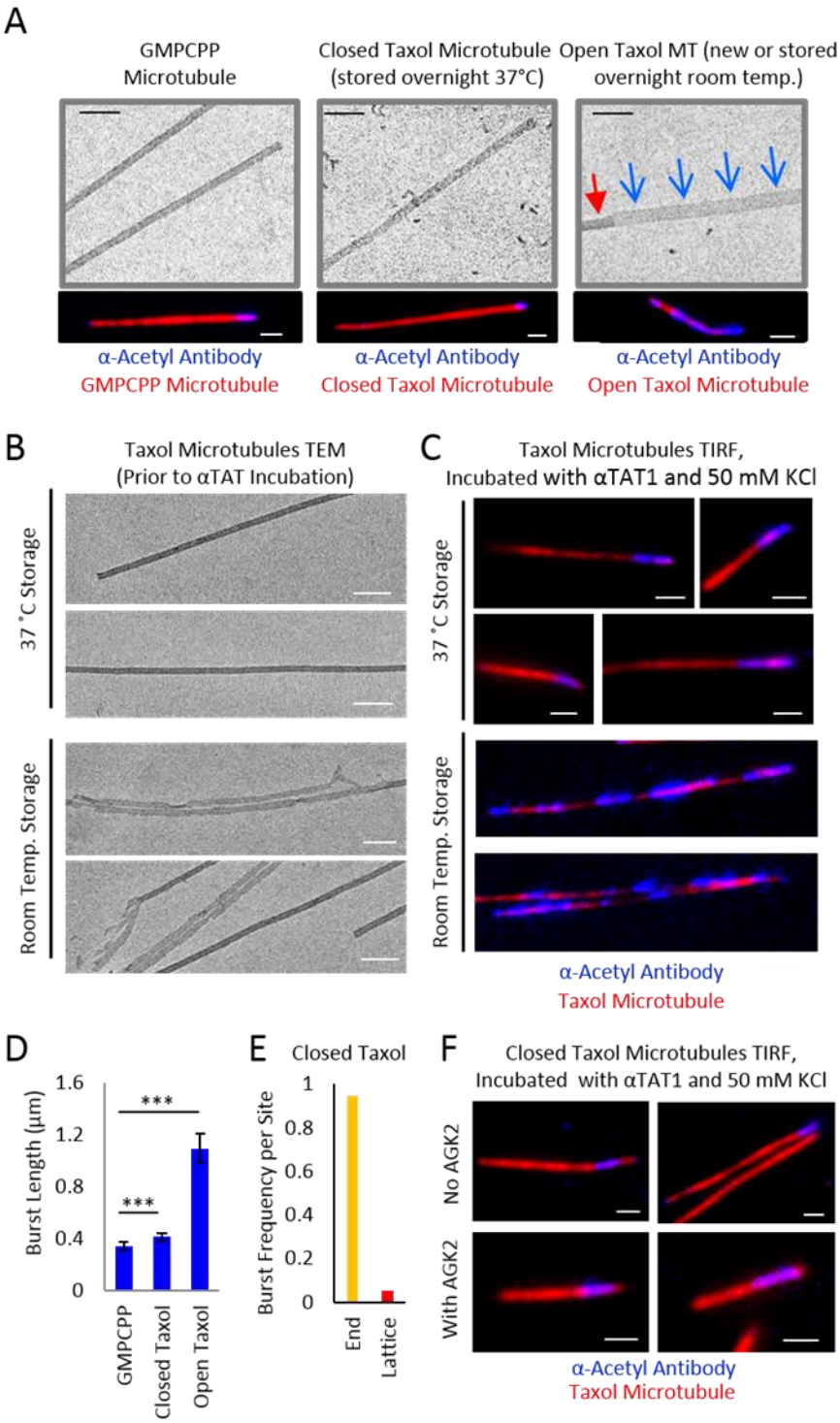
A
GMPCPP Microtubule
Closed Taxol Microtubule (stored overnight 37°C)
Open Taxol MT (new or stored overnight room temp.)
α-Acetyl Antibody
GMPCPP Microtubule
α-Acetyl Antibody
Closed Taxol Microtubule
α-Acetyl Antibody
Open Taxol Microtubule
B
Taxol Microtubules TEM
(Prior to αTAT Incubation)
37 °C Storage
Room Temp. Storage
C
Taxol Microtubules TIRF,
Incubated with αTAT1 and 50 mM KCl
37 °C Storage
Room Temp. Storage
α-Acetyl Antibody
Taxol Microtubule
D
Burst Length (μm)
1.6
1.2
0.8
0.4
0
***
***
GMPCPP
Closed Taxol
Open Taxol
E
Closed Taxol
Burst Frequency per Site
1
0.8
0.6
0.4
0.2
0
End
Lattice
F
Closed Taxol Microtubules TIRF,
Incubated with αTAT1 and 50 mM KCl
No AGK2
With AGK2
α-Acetyl Antibody
Taxol Microtubule

Figure S2-4 Discussion: Comparison to Previous Work.

Our results suggest that αTAT1 enters the microtubule ends and preferentially acetylates these ends because αTAT1 is not able to efficiently diffuse within the lumen. This is in contrast to recent work by Szyk et al., which suggested that a high concentration of αTAT1 was able to almost simultaneously acetylate an entire microtubule through longer acetylation bursts that occurred randomly along the microtubule length (Szyk et al, Fig. 2-4) (1). We noted that a potentially important difference between the two studies was that we used GMPCPP stabilized microtubules to analyze acetylation patterns on pre-formed microtubules, while Szky et al. used Taxol-stabilized microtubules. Both the timing and method of Taxol introduction have been shown to affect the structure of Taxol microtubules (2).

Therefore, to better understand the effect that the microtubule stabilization method may have on the acetylation results, microtubules were grown in the presence of GTP, diluted into a Taxol buffer solution (single-step), and then stored overnight at 37˚C. For Taxol microtubules stored overnight at 37 °C, the structure of the GMPCPP and Taxol microtubules, as imaged by TEM, was similar (Fig. S2-4A, left vs center). The acetylation bursts were slightly longer than those in GMPCPP microtubules (~20 %) (Fig. S2-4D, "closed Taxol", $p<2X10^{-16}$), but this increase in burst length was quite moderate compared to the large stretches of acetylation observed by Szky et al (1).

However, we noted that the microtubules stored overnight in Taxol at 37 °C tended to be much longer than our freshly prepared Taxol microtubules, suggesting that perhaps the overnight 37 °C storage condition was sufficient to drive microtubule assembly and repair, even in the presence of a very low concentration of free tubulin. Thus, we compared the structure of Taxol microtubules which were either imaged immediately after preparation, or stored overnight at room temperature, to those stored overnight at 37 °C. We found that freshly prepared Taxol microtubules, or those stored overnight at room temperature, were much more likely to have large stretches of open lattice (Fig. S2-4A, right, Fig. S2-4B), as compared to GMPCPP microtubules (Fig. S2-4A, left), or to Taxol microtubules stored overnight at 37°C (Fig. S2-4A, center, Fig. S2-4B).

We performed our acetylation-TIRF assay to determine whether the more "open" Taxol-stabilized microtubule structures (e.g., freshly prepared or stored overnight at room temperature) led to longer acetylation burst lengths (Fig. S2-4C). We found that acetylation bursts for the freshly prepared Taxol microtubules were >3-fold longer than on the GMPCPP microtubules (Fig. S2-4D) (Two sample t-test, $p<2.2X10^{-16}$), and 2.6 fold longer than the closed Taxol microtubules stored overnight at 37 °C ($p<1X10^{-6}$) (Fig. S2-4D). This suggests that 1-step microtubule stabilization by Taxol may lead to more open, sheet-like microtubule structures, and thus to a more disperse acetylation pattern due to direct access of αTAT1 to its acetylation site. Thus, differences in microtubule preparation, and thus microtubule structure, may contribute to differing acetylation patterns between this study and Szyk et al (1).

Further, TIRF acetylation experiments in Szyk et al were performed with 50 mM added KCl, which would also be expected to increase burst lengths: as shown in Fig. 2-6E, we found that there was a ~2-fold increase in burst lengths with 50 mM added KCl

as compared to the “no KCl added” conditions in our baseline experiments. Thus, the combination of a higher salt concentration and room-temperature storage Taxol microtubules may have contributed to longer acetylation bursts, often throughout the microtubule, in the previous study by Szyk et al (conditions reproduced from Szyk et al in Fig. S2-4C).

Finally, our experimental measurements for the diffusion coefficient of αTAT1 on the microtubule lattice were similar to those reported by Szyk et al (Fig. S2-5). However, as previously reported (3), αTAT1 interacts electrostatically with the outside of the microtubule lattice, and so we predicted that the measured lattice diffusion was on the outside of the microtubule, while the behavior of the αTAT1 enzyme on the inside of the microtubule would be dominated by binding/unbinding and rapid diffusion in solution. This argument is consistent with (a) observations of diffusing αTAT1-GFP molecules “jumping” from one microtubule to another on the exterior surface of the microtubule, consistent with electrostatic interactions such as with the C-terminal tails of tubulin (3), (b) higher affinity of αTAT1 for its acetylation site on the inside of the microtubule than for the outside of the microtubule, as predicted by our αTAT1-GFP experiments and simulations, and (c) observations of increasing acetylation burst lengths at higher salt concentrations, which suggests that mobility of αTAT1 on the inside of the lumen is dominated by affinity rather than a lattice diffusion coefficient.

Figure S2-4 Legend: (A) Top: TEM images of GMPCPP Microtubules (left), as compared to Taxol-stabilized microtubules that were imaged after overnight storage at 37 °C (middle). Microtubule structures appear similar. (scale bar 100 nm). Bottom: Typical TIRF microscopy images of acetylation bursts on GMPCPP microtubules as compared to Taxol microtubules with 37 °C storage. Bursts are of similar length and localization. (scale bar 1 μm). Top Right: TEM images of Taxol-stabilized microtubules, imaged immediately following one-step dilution into Taxol buffer. Blue arrows indicate open microtubule structure, red arrow closed microtubule structure. (scale bar 100 nm). Bottom Right: TIRF microscopy image of acetylation burst on freshly prepared Taxol microtubule. Bursts appear to be longer as compared to GMPCPP microtubules. (scale bar 1 μm). (B) Taxol microtubules stored at room temperature overnight had more disrupted structures than Taxol microtubules stored at 37˚C. (C) This increase in disrupted microtubule structure correlated with longer and more disperse stretches of acetylation. (D) Comparative analysis of burst lengths from GMPCPP (n=426), Closed Taxol (37 °C storage) (n=249), and Open Taxol (newly prepared) microtubules (n=328). Burst lengths were substantially longer for the Open Taxol microtubules (Log transformed t test p value<$1X10^{-6}$). (E) Burst localization in closed Taxol-stabilized microtubules is similar to GMPCPP microtubules. (F) In order to compare our results to a previous study (1), we tested the effect of the SIRT2 inhibitor, AGK2, on acetylation bursts using the acetylation TIRF assay. We found that AGK2 did not appear to substantially affect acetylation burst lengths on Taxol microtubules.

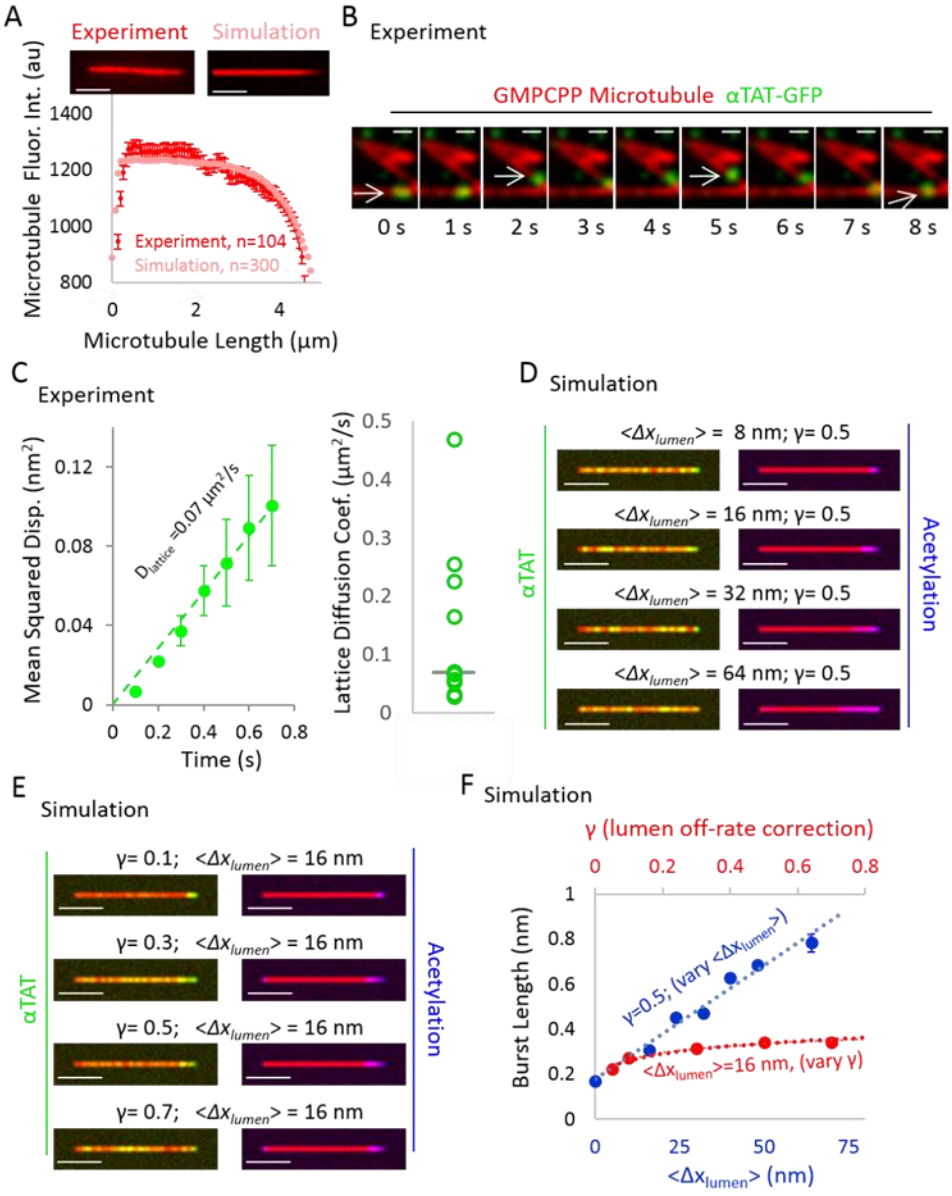
A
Experiment
Simulation
Microtubule Fluor. Int. (au)
1400
1200
1000
800
Experiment, n=104
Simulation, n=300
0
2
4
Microtubule Length (µm)
B
Experiment
GMPCPP Microtubule αTAT-GFP
0 s
1 s
2 s
3 s
4 s
5 s
6 s
7 s
8 s
C
Experiment
Mean Squared Disp. (nm²)
0.12
0.08
0.04
0
D_lattice =0.07 µm²/s
0
0.2
0.4
0.6
0.8
Time (s)
Lattice Diffusion Coef. (µm²/s)
0.5
0.4
0.3
0.2
0.1
0
D
Simulation
<Δx_lumen> = 8 nm; γ= 0.5
<Δx_lumen> = 16 nm; γ= 0.5
<Δx_lumen> = 32 nm; γ= 0.5
<Δx_lumen> = 64 nm; γ= 0.5
αTAT
Acetylation
E
Simulation
γ= 0.1; <Δx_lumen> = 16 nm
γ= 0.3; <Δx_lumen> = 16 nm
γ= 0.5; <Δx_lumen> = 16 nm
γ= 0.7; <Δx_lumen> = 16 nm
αTAT
Acetylation
F
Simulation
γ (lumen off-rate correction)
0
0.2
0.4
0.6
0.8
Burst Length (nm)
1
0.8
0.6
0.4
0.2
0
γ=0.5; (vary <Δx_lumen>)
<Δx_lumen>=16 nm, (vary γ)
0
25
50
75
<Δx_lumen> (nm)

Figure S2-5: Evaluation of Simulation Parameters. (A) Simulation tip structures were matched to experimental fluorescence distribution curves for GMPCPP stabilized microtubules to assess models which could reproduce the experimental αTAT-GFP localization on the microtubules. (B) Diffusion of αTAT1-GFP was experimentally observed on stabilized GMPCPP microtubules to assess the diffusion behavior and measure the diffusion coefficient. "Jumping" of αTAT1-GFP from one microtubule to another suggests that our observed diffusion behavior is on the exterior surface of the microtubule, consistent with electrostatic interactions such as with the C-terminal tails of tubulin as previously reported [61]. (C) The external lattice diffusion coefficient ($D_{lattice}$) is constrained by experiments. (D) The effect of increasing luminal αTAT1 step sizes on both acetylation burst length and also αTAT1-GFP localization in the simulation was qualitatively assessed. (E) Similarly, the effect of increasing the αTAT luminal off-rate correction on both acetylation burst length and also αTAT1-GFP localization was qualitatively assessed. (F) Quantitative analysis of burst length for simulations shown in (D) and (E): The strongest effect on burst length is the luminal αTAT1 step sizes ($<\Delta x_{lumen}>$) (blue line). For the luminal αTAT1 off-rate, the burst lengths approach the maximal values allowed by the set value for $<\Delta x_{lumen}>$ when $\gamma>0.1$. Therefore, low luminal off-rates can limit burst length to below the maximum value allowed by $<\Delta x_{lumen}>$ (red line), however, increased (long) burst lengths result from increasing step sizes prior to rebinding (e.g., by $<\Delta x_{lumen}>$), which represents travel distance prior to rebinding.

Experimental Methods

Purification of αTAT1 and αTAT1-GFP

A plasmid, pGEX-GST-αTAT1, was purchased from Addgene.org (#27101) and transformed into Rosetta high protein expression E.coli (EMDMillipore, #71397)). GFP was also ligated into this plasmid to create pGEX-GST-GFP-αTAT1. E. coli containing these plasmids were grown in 10ml of LB+amp+cam media at 37° overnight, subcultured 1:200 into 500ml of fresh media and grown for 3.5hr at 37° until an A600 of 0.58. IPTG was then added to 1mM final and the cultures continued growth at 18° for 16hr. Cultures were centrifuged and the cell pellets resuspended in 16ml lysis buffer (50mM Tris pH 75, 150mM NaCl, 1% triton X-100, 10% glycerol, 2mM DTT, 2mM AEBSF, 4mg/ml lysozyme and mixed at 90min at 30°. The cell suspension was then frozen drop-wise in liquid nitrogen and the frozen beads were ground multiple times in a coffee grinder. Lysate was centrifuge at 18000xg for 1hr at 4° and the supernatant was mixed with 250ul of PBS-washed glutatione-sepharose 4B beads (GE Healthcare, #17-0756-01) for 2.5hr and 4°. Beads were then washed 4x with 3ml of lysis buffer, resuspended in 1ml lysis buffer + 12ul of Prescission protease (GE Healthcare, #27-0843-01) and mixed at 4° for 20 hrs to release the αTAT1 from the GST tag and beads (Fig. S2-1).

In vitro Microtubule-αTAT1-GFP Experiments and Imaging

GMPCPP Microtubules

To make stabilized GMPCPP microtubules, a 45 µL solution which consisted of 3.9 µM tubulin (25% rhodamine-labeled, 75% unlabeled) and 1 mM GMPCPP in BRB80 was mixed and kept on ice for 5 min, then incubated at 37^{o}C for 10 minutes to 2 hours. Following incubation, the seeds were diluted into 400 µL warm BRB80, and 350 µL of this dilution was spun down in an air-driven ultracentrifuge @ 20 psi for 5 min. The supernatant was discarded, and the pellet resuspended into 400 µL warm BRB80. To further stabilize the microtubules, Taxol was added to a final concentration of 10 µM Taxol.

Construction and Preparation of Flow Chambers for Imaging

Imaging flow chambers were constructed as in Section VII of Gell et al. 2010 [114], with the following modifications: two narrow strips of parafilm replaced double-sided scotch tape as chamber dividers: following placement of the smaller coverslip onto the parafilm strips, the chamber was heated to melt the parafilm and create a seal between the coverslips; typically only three strips of parafilm are used, resulting in two chambers per holder. Chambers were prepared with anti-rhodamine antibody followed by blocking with Pluronic F127, as described in Section VIII of Gell et al. 2010 [114].

αTAT1-GFP Binding Assay and Imaging

A flow chamber was prepared as described above. GMPCPP microtubules were adhered to the chamber coverslip, and the chamber was flushed gently with warm

BRB80. The flow chamber was heated to 28°C using an objective heater on the microtubule stage, and then 3-4 channel volumes of imaging buffer containing 110 µg/ml Glucose Oxidase, 20 µg/ml Catalase, 20 nM D-Glucose, 10 mM DTT, 0.1 mg/ml Casien, and 1% Tween-20, were flushed through the chamber. A reaction mixture containing the imaging buffer and .08 to 100 nM final concentration of αTAT1-GFP (Experiments in Fig. 1 use 30 nM) was then prepared and immediately flowed into the imaging chamber, with drops left at the flow chamber ends to keep the flow chamber from drying out during imaging.

After 10 minutes, αTAT1-GFP binding on GMPCPP microtubules was imaged on a Nikon TiE microscope using 488 nm and 561 nm lasers sent through a Ti-TIRF-PAU for Total Internal Reflectance Flourescence (TIRF) illumination. An Andor iXon3 EM-CCD camera fitted with a 2.5X projection lens was used to capture images with high signal to noise and small pixel size (64 nm). Movies were collected in 5 s intervals using TIRF with a Nikon CFI Apochromat 100X 1.49 NA oil objective. Images for tip structure/αTAT1-GFP binding analysis were single time points only, to avoid complications from photobleaching.

Image Analysis

The single time point images of GMPCPP microtubules with αTAT1-GFP were cropped to separate each microtubule into a single image using ImageJ. Then, integrated and averaged line scans of each microtubule image were created using a MATLAB script. In each case, the microtubule was aligned with the “dim” fluorescence end on the right, and then the red and green fluorescence were plotted as a function of microtubule length from microtubule bright end to microtubule dim end. To do this, the red tubulin fluorescence was integrated along the length of each microtubule ± 256 nm above and below the microtubule centerline to account for point spread function and variability in properly finding the microtubule centerline. Then, the red fluorescence intensity was summed over the last 576 nm on both ends of the microtubule. The lower summed value was considered the “dim” microtubule end, while the higher summed value was deemed the “bright” microtubule end. Scatter plots were created by importing the integrated line scan fluorescence data into Excel.

αTAT1 and BSA Conjugation to Gold Beads

αTAT1 and BSA were conjugated to 20nm gold beads with the Innovacoat 20nm gold particle labeling kit (Innova Biosciences, #229-0005) as per instructions, except that the αTAT1 was buffer-exchanged beforehand into PBS with Microcon Ultracel YM-3 microcentrifuge filter concentrators. For labeling proteins with 1.4 nm gold particles, buffer exchanged αTAT1 was reacted for 1.5hr with mono-sulfo-NHS-nanogold 1.4nm particle reagent as per instructions (nanoprobes #2025A) and excess particles were washed out by 2 - wash / centrifugations in Amicon Ultra 0.5ml 30k filter units, diluting with PBS.

αTAT1-conjugated gold beads (1.3nm and 20nm) were incubated with GMPCPP microtubules and Acetyl CoA (.35mM final concentration) for 20 minutes and imaged using Transmission Electron Microscopy. BSA-conjugated gold beads (1.3nm and 20nm) were incubated with GMPCPP microtubules and Acetyl CoA (.35mM final concentration) for 20 minutes and imaged using Transmission Electron Microscopy.

Calcium Treated GMPCPP Microtubules

GMPCPP Microtubules were incubated with .04 M final concentration of $CaCl_2$ for 40 minutes at 37˚C. Calcium treated GMPCPP microtubules were then adhered to an imaging flow chamber as described above. A mixture of αTAT1-GFP in imaging buffer was flushed into the flow chamber and imaged as described above.

Transmission Electron Microscopy

Reaction mixtures were prepared as described for each experiment. A drop of the reaction mixture was placed on a 300-mesh carbon coated copper grid for 1 minute. At 1 minute, the grid was stained with 1% uranyl acetate for 1 minute. The stain was then wicked away with filter paper and the grid was left to dry and then stored. Specimens were observed using an FEI Technai Spirit BioTWIN transmission electron microscope. Images were recorded at 15,000X-23,000X at -3 to -5 defocus.

Fluorescence Microtubule Acetylation Assay

Closed Taxol Microtubules

To make Closed Taxol microtubules, a mixture composed of 33 µM tubulin (25% rhodamine-labeled, 75% unlabeled), 1 mM GTP, 4 mM $MgCl_2$, and 4 % DMSO was prepared and kept on ice for 5 min, and then incubated at 37^{o}C for 30 minutes. Following incubation, the microtubules were diluted into 990 µl warm Taxol solution (10 µM Taxol with Brb80) and stored overnight at 37^{o}C. Taxol microtubules were spun down in an air-driven ultracentrifuge @ 20 psi for 5 min and resuspended in 50 µl warm 10 µM Taxol Brb80 buffer before use in assays.

Open Taxol Microtubules

To make Open Taxol microtubules, a mixture composed of 33 µM tubulin (25% rhodamine-labeled, 75% unlabeled), 1 mM GTP, 4 mM $MgCl_2$, and 4 % DMSO was prepared and kept on ice for 5 min, and then incubated at 37^{o}C for 30 minutes. Following incubation, the microtubules were diluted into 990 µl warm Taxol solution (10 µM Taxol with Brb80). To make Open Taxol microtubules, the microtubules were either used immediately, or else stored overnight at room temperature.

αTAT1 Acetylation Assay and Imaging

GMPCPP, Calcium Treated, Closed Taxol, or Open Taxol microtubules were adhered to flow chamber coverslips as described above. A mixture of αTAT1 (2.5µM and

.07μM final concentration) or αTAT1 conjugated to a 20 nm gold bead, Acetyl CoA (380 nM final concentration), KCl (0-100mM, designated in text), and Brb80 was flown in to the chamber and incubated for 5-120 minutes (designated in text). Then, imaging buffer with CF4-88 labeled anti-acetylated tubulin (6-11B-1, Sigma Aldrich cat. #T7451-200L; 80 μM) was flown in to the chamber as described above and imaged using TIRF microscopy as above.

αTAT1 Acetylation of Dynamic Microtubules Assay and Imaging

A mixture composed of 45 μM tubulin (25% rhodamine-labeled, 75% unlabeled), 1 mM GTP, 4 mM $MgCl_2$, 4 % DMSO, 1.8 μM αTAT1, and 380nM Acetyl CoA was prepared and kept on ice for 5 min, and then incubated at 37^{o}C for 30 minutes. Following incubation, the microtubules were diluted into 990 μl warm Taxol solution (10 μM Taxol with Brb80). The microtubules were adhered to flow chamber coverslips. Then, imaging buffer with CF4-88 labeled anti-acetylated tubulin (6-11B-1, Sigma Aldrich cat. #T7451-200L; 80 μM) was flown in to the chamber as described above and imaged using TIRF microscopy as above.

Image Analysis

The single time point images of GMPCPP microtubules with anti-acetyl antibody were cropped to separate each microtubule into a single image using ImageJ. Then, a MATLAB script was used to measure the location and length of acetylation “bursts” on the microtubules by manual clicking. In each case, the burst positions were measured relative to the bright microtubule end and the dim microtubule end, with assignment of “bright” and “dim” ends as described above. Bursts that occupied the first two pixels from each microtubule end were said to occupy a “tip” site, and bursts occupying any other pixels along the microtubule were labeled “lattice” sites. The burst frequencies of tip and lattice sites were calculated by normalizing the total number of bursts at each site by the total available sites in each category. Burst frequency and mean number of bursts per microtubules with at least one burst were calculated by manually counting bursts on microtubules.

The analysis of tubulin fluorescence intensity at lattice bursts was completed using a custom MATLAB script in which the average red fluorescence intensity was calculated over the entire microtubule by manual clicking at each end of the microtubule, and then the average red fluorescence intensity under a burst was calculated by manual clicking at the ends of an observed lattice burst. The ratio of red tubulin fluorescence at a lattice burst relative to the average red fluorescence along the length of the microtubule was then calculated according to:

$$fluor\_ratio = \frac{burst\_flour}{MT\_fluor} \qquad (1)$$

Where *burst_fluor* is the average red tubulin fluorescence intensity under an acetylation burst, and *MT_fluor* is the average red fluorescence intensity along the entire length of the microtubule. If this ratio was < 1 for a given microtubule, then the burst was classified as being in a “dim” spot on the microtubule. In contrast, if this ratio was ≥ 1, then the burst was classified as being in a “bright” spot on the microtubule.

Western Blot Acetylation Assay

Acetylation Reaction Mixture

Tubulin dimers, GMPCPP microtubules, or Calcium treated GMPCPP microtubules were mixed with Acetyl CoA (0.4 mM final concentration), unlabeled αTAT1 or αTAT1-GFP (4.1 μM final concentration), and BRB80 for 90 minutes. Reactions were kept at 37 ˚C. Aliquots were taken from reaction mixture at 0, 10, 20, 40, 60, and 90 minutes and stored at -20˚C.

Shearing Acetylation Assay

GMPCPP microtubules were mixed with Acetyl CoA (0.4 mM final concentration), unlabeled αTAT1 (2.05 μM final concentration), and BRB80 for 60 minutes. At 60 minutes the mixture was split into two separate mixtures. One mixture was sheared using a small diameter needle while the other mixture was not. After 120 minutes the sheared mixture was sheared a second time while the other mixture was not. Reactions were kept at 37 ˚C. Aliquots were taken from the unsheared mixture at 0, 60, 120, and180 minutes and from the sheared mixture at 120 and 180 minutes and stored at -80 ˚C for western blotting.

Cell Lysate and Known αTAT1 concentration Mixtures

Human RPE cells were grown using standard culturing conditions (in DMEM, 10% PBS, 1% penStrep), and lysed in 5X non-reducing buffer with BME by boiling for 5 minutes. Cell lysates (1, 5, and 10μl) were loaded alongside known concentrations of purified αTAT1 (3, 37.5, and 665 ng/μl).

Western Blots

The reaction mixture aliquots were analyzed for their protein concentrations using a Nanodrop ND-1000 Spectrophotometer. Aliquots were diluted in BRB80 and PAGE buffer. The samples were resolved in 10% polyacrylamide gels and then transferred to PVDF membranes. Membranes were then blocked in 3% BSA in Tris-buffered saline with 0.15% Tween and probed with primary antibodies for anti-α-tubulin (DM1A, VWR Scientific cat.#PI62204), anti-acetylated tubulin (6-11B-1, Sigma Aldrich cat. #T7451-200L), or anti- αTAT1 (C6orf134, LifeSpan Biosciences, Inc cat. #LS-C116215). The membranes were subsequently probed with a horseradish peroxidase-linked anti-mouse secondary (Santa Cruz BioTechnology cat. #SC-2005) or anti-rabbit secondary (Santa Cruz BioTechnology cat. #SC-2004) antibody and developed using chemiluminescence.

Statistical Analysis

All reported tests were calculated in R and are noted in the manuscript.

Modeling Methods

A stochastic simulation was developed to model αTAT dynamics on both the inside and the outside of the microtubule. Tables S2-1-S2-3 summarize the overall simulation behaviors and rules, including applicable variables, formulae, and parameters. Model parameters are shown in Table S4, and are based on values experimentally gathered in this study, as well as from previously published data. Simulation parameters (e.g., such as simulation duration (t_{dur} [s]), and time step size, (Δt_{step} [s])) are shown in Table S2-5. Finally, key modeling assumptions are summarized in Table S2-6.

Essential aspects of the stochastic model include (1) Initiation of a stable microtubule "template" at the start of each microtubule simulation; (2) calculation of on and off rates on the outside of the microtubule for each αTAT1 molecule in the simulation, and then probabilistic αTAT1 molecule unbinding or rebinding at random locations on the outside of the microtubule; (3) diffusion of bound αTAT1 molecules which are on the outside of the lattice; (4) entry of αTAT1 molecules into the microtubule lumen; (5) calculation of on and off rates on the inside of the microtubule lumen for each αTAT1 molecule in the simulation, and then probabilistic αTAT1 molecule unbinding or rebinding at specified locations; (6) acetylation events inside the lumen; and (7) model-convolution image generation for αTAT1-GFP and acetylation antibody images. Following are details for each of these simulation activities:

(1) Initiation of a stable microtubule "template" at the start of each microtubule simulation

At the start of the simulation for each microtubule, a stable microtubule "template" was created, which then remained constant for the duration of each individual microtubule simulation. This was created by selecting a "tip slope" for the tip of each microtubule plus-end, according to:

$$tip\_slope = \left| randn * mean\_slope \right| \quad (2)$$

Where *randn* is a built-in MATLAB function which produces a Gaussian random number with mean 0 and standard deviation 1, and *mean_slope* is the mean taper angle at the microtubule plus end. The value for *mean_slope* was fitted to experimental data by varying the value in simulation until the average simulated microtubule fluorescence over n=300 microtubules was similar to the experimental curve (Fig. S2-5A).

(2) Behaviors on the external surface of the microtubule

Simulation of αTAT1 interaction with the outside of the microtubule is based on previously published data which suggests that αTAT1 binds the exterior surface of microtubules, and interacts with the C-terminal tails of tubulin [102], and on our own and previously published observations that αTAT1-GFP can diffuse on the external surface of microtubules (Fig. S2-5) [84]. Thus, simulated interactions of αTAT1 with the exterior of the microtubule lattice consisted of (a) binding of αTAT1 on the exterior surface of the microtubule, (b) diffusion of αTAT1 on the exterior surface of the microtubule, and (c) unbinding of αTAT1 from the exterior surface of the microtubule. General rules for each of these activities were as follows:

(a) Binding of αTAT1 on the exterior surface of the microtubule: The on-rate of αTAT1 onto the exterior surface of the microtubule was calculated as shown in Table S1. Then, for each individual simulated αTAT1 molecule, the probability of binding to the microtubule exterior was calculated from:

$$pr\_on = 1 - \exp(-k^{*}_{on,lattice}\Delta t_{step}) \quad (3)$$

Where *pr_on* is the probability that a given αTAT1 molecule would bind to a microtubule in the current time step. Thus, if a uniformly distributed random number between 0 and 1 was less than the calculated value for *pr_on*, then the αTAT1 molecule would attach to the microtubule. All αTAT1 molecules, whether newly bound or rebinding, were attached at random locations on the microtubule, weighted by protofilament density. This is based on the assumption that there was a uniform density of αTAT1 molecules around the microtubule, and that αTAT1 could diffuse rapidly in solution outside of the microtubule lumen.

(b) Unbinding of αTAT1 from the exterior surface of the microtubule: The off-rate of αTAT1 from the exterior surface of the microtubule was calculated as shown in Table S2-1, except in the case where an αTAT1 molecule was on an exposed protofilament at the microtubule tip (defined by a position on a protofilament which is longer than the shortest protofilament in the microtubule), in which case the off-rate is calculated according to Table S2-3. Then, for each individual simulated αTAT1 molecule, the probability of unbinding from the microtubule exterior was calculated from:

$$pr\_off = 1 - \exp(-k_{off,lattice}\Delta t_{step}) \quad (4)$$

Where *pr_off* is the probability that a given αTAT1 molecule would unbind from a microtubule in the current time step. Thus, if a uniformly distributed random number between 0 and 1 was less than the calculated value for *pr_off*, then the αTAT1 molecule would detach from the microtubule.

(c) Diffusion of αTAT1 on the exterior surface of the microtubule. Diffusion was experimentally observed on the surface of the microtubule, with a calculated diffusion coefficient of 0.08×10^6 nm^2/s (Fig. S2-5 and [84]), consistent with previous reports of electrostatic interactions such as with the C-terminal tails of tubulin on the external surface of the microtubule [102]. Thus, each bound αTAT1 molecule was allowed to diffuse on the external surface of the microtubule, with step size as shown in Table S2-1 and constrained by the experimentally measured diffusion coefficient. αTAT1 molecules which diffused to the end of a protofilament would remain at the tip of the protofilament, and did not continue to diffuse.

Table S2-1: Behaviors on the External Surface of the Microtubule

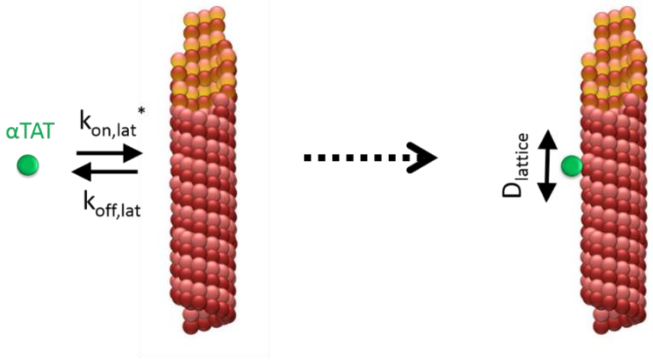

Behavior	Model Equation	Variables	Parameters
αTAT attachment to outside of microtubule lattice	$k_{on,lattice}^* = k_{on,lattice}[Tubulin]$	$k_{on,lattice}^*$ = αTAT on-rate for outside of microtubule lattice	*[Tubulin]* = tubulin-polymer concentration $k_{on,lattice}$ = αTAT diffusion-limited bimolecular on-rate constant
αTAT detachment from outside of microtubule lattice	--	--	$k_{off,lattice}$= αTAT off-rate from the external surface of the microtubule lattice
Diffusion of Bound αTAT on external surface of microtubule lattice	$(<\Delta x_{lattice}>^2)^{1/2} = \pm\sqrt{2D_{lattice}\Delta t_{step}}$	$\Delta x_{lattice}$ = αTAT diffusion step size on microtubule outside lattice	$D_{lattice}$ = αTAT diffusion coefficient on microtubule lattice Δt_{step} = simulation time step size

(3) Entry into the microtubule lumen

αTAT1 molecules bound to the exterior surface of a microtubule had the opportunity to enter the microtubule lumen with rules which depended on the particular lumen entry model being tested. For the end-entry model, αTAT1 molecules which arrived at either

end of a microtubule (as defined by arriving at a position which was past the length of the shortest protofilament), would enter the lumen with a probability as defined in Table S2-2. For the lattice entry model, αTAT1 molecules which were bound to the lattice at any position would enter the lumen with a probability as defined in Table S2-2.

Table S2-2: Rules for Entry into the Microtubule Lumen

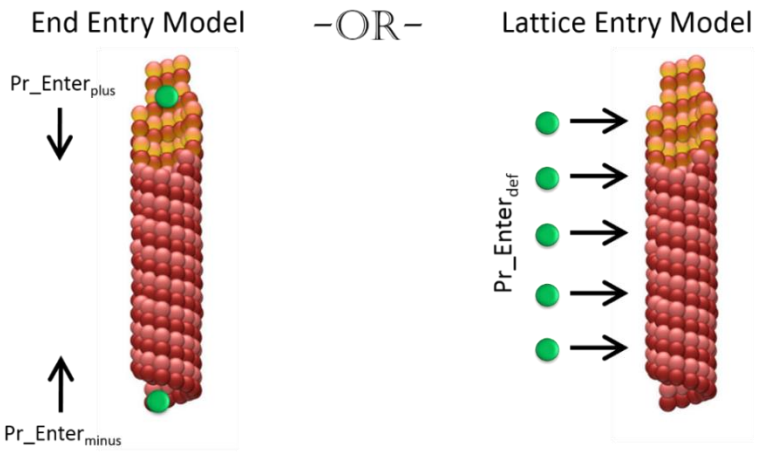

Behavior	Model Equation	Variables	Parameters
In the end-entry model, αTAT entry into lumen, from plus-end of microtubule	--	--	Pr_Enter_{plus} = probability of αTAT which is present at microtubule plus end to enter the lumen
In the end-entry model, αTAT entry into lumen, from minus-end of microtubule	--	--	Pr_Enter_{minus} = probability of αTAT which is present at microtubule minus end to enter the lumen
In the lattice entry model, αTAT entry into lumen, from a defect or other opening along the length of the lattice	--	--	Pr_Enter_{defect} = probability of αTAT which is present at a position along the lattice to enter into the lumen

(4) Behaviors on the internal surface of the microtubule lumen

Simulation of αTAT1 interaction with the inside of the microtubule lumen (e.g., the α-tubulin acetylation site) consisted of (a) binding of αTAT1 on the interior surface of

the microtubule, (b) unbinding of αTAT1 from the interior surface of the microtubule, and (c) Diffusion: given that the acetylation site is on the inside of the microtubule, we assumed that αTAT1 diffusion would exclusively occur in solution after unbinding, consistent with previous reports [84]. General rules for each of these activities were as follows:

a) Binding of αTAT1 on the interior surface of the microtubule: The on-rate of αTAT1 onto the interior surface of the microtubule was calculated as shown in Table S2-1. Then, for each individual simulated αTAT1 molecule, the probability of binding to the microtubule exterior was calculated from:

$$pr\_on = 1 - \exp(-k^{*}_{on,lumen}\Delta t_{step}) \quad (5)$$

Where *pr_on* is the probability that a given αTAT1 molecule would bind to a microtubule in the current time step. Thus, if a uniformly distributed random number between 0 and 1 was less than the calculated value for *pr_on*, then the αTAT1 molecule would attach to the microtubule. We note that because the theoretical rebinding rate of αTAT1 molecules is very high (~1.7×10^4 s^{-1}), the on rate of the αTAT1 molecules in the simulation are limited by the time step size in the simulation, which is typically 0.01 s, to reduce computational intensity. However, a corrected free αTAT1 lumen diffusion coefficient was used to compensate for the simulation time step size so that the reported travel distance between binding events for a free αTAT1 molecule was correctly reflected, as described below.

In contrast to the binding events on the external surface of the microtubule, αTAT1 molecules were not reattached at random locations on the inside of the microtubule, but rather were rebound very near to their previous location in the microtubule lumen. Here, given the high concentration of acetylation sites on the inside of the microtubule, we reasoned that free αTAT1 diffusion in solution on the inside of the microtubule would be limited by rapid rebinding of αTAT1 to nearby acetylation sites. This is due to the small volume and dense packing of tubulin subunits inside of the microtubule lumen, such that the concentration of α-tubulin Lys40 acetylation site binding sites is extremely high (~17×10^3 μM). Therefore, a typical rebinding time for a free αTAT1 molecule inside the lumen with a diffusion limited biomolecular on-rate constant k_{on}= 1 $\mu M^{-1}s^{-1}$ [106] would be ($1/k_{on}$[acetylation sites]) = 6×10^{-5} sec. During this time, the mean distance traveled for a free αTAT molecule prior to rebinding to an acetylation site (Δx) can then be calculated from:

$$(< \Delta x_{lumen} >^2)^{1/2} = \sqrt{2D_{solution}\Delta t_{rebind}} \quad (6)$$

Where $D_{solution}$ is the αTAT1 diffusion coefficient in solution (2.6×10^7 nm^2/s), and Δt_{rebind} is the typical rebinding time (~10^{-5}) sec. This leads to a predicted mean travel distance prior to αTAT1 rebind of ~50 nm. For simplicity and to reduce simulation computational intensity, an adjusted diffusion coefficient, D_{lumen}, was then used to compensate for the diffusion of free αTAT1 molecules within the simulation time step size, Δt_{step}. Thus, free αTAT1 molecules in the simulation would rebind a distance of $<\Delta x_{lumen}>$ away from their previously bound position inside of the lumen (Table S2-3). To test the sensitivity of the simulation to this parameter, the simulation predictions for a range of $<\Delta x_{lumen}>$ values was evaluated (Fig. 2-6G).

b) Unbinding of αTAT1 from the interior surface of the microtubule: The off-rate of αTAT1 from the interior surface of the microtubule was calculated as shown in Table S2-1. Then, for each individual simulated αTAT1 molecule, the probability of unbinding from the microtubule interior acetylation site was calculated from:

$$pr\_off = 1 - \exp(-k_{off,lumen}\Delta t_{step}) \quad (7)$$

Where *pr_off* is the probability that a given αTAT1 molecule would unbind from an acetylation site in the current time step. Thus, if a uniformly distributed random number between 0 and 1 was less than the calculated value for *pr_off*, then the αTAT1 molecule would detach from the acetylation site. To test the sensitivity of the simulation to this parameter, the simulation predictions for a range of $k_{off,lumen}$ values was evaluated (Fig. 2-6G).

Table S2-3: Behaviors on Internal Surface of Microtubules

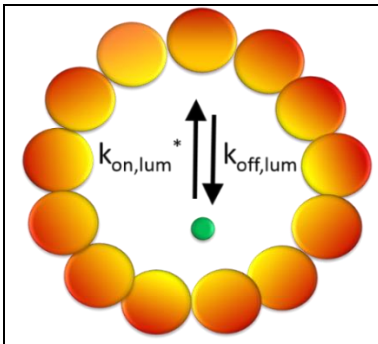

Section View

Behavior	Model Equation	Variables	Parameters
αTAT attachment to acetylation site inside the microtubule lumen; reattachment rate	$k_{on,lumen}^* = k_{on,lumen}[Ac\_sites]$	$k_{on,lumen}^*$ = αTAT on-rate for acetylation sites inside the microtubule lumen	*[Ac_sites]* = concentration of acetylation sites inside the microtubule lumen $k_{on,lumen}$ = diffusion limited αTAT bimolecular on-rate constant
Diffusion of Free αTAT inside of the microtubule lumen	$(<\Delta x_{lumen}>^2)^{1/2} = \pm\sqrt{2D_{lumen}\Delta t}_{step}$	Δx_{lumen} = free αTAT diffusion step size inside of microtubule lumen	D_{lumen} = free αTAT diffusion coefficient inside of microtubule lumen Δt_{step} = simulation time step size
αTAT detachment from acetylation site inside the microtubule lumen	$k_{off,lumen} = \gamma(k_{off,lattice})$	$k_{off,lumen}$ = αTAT off-rate from inside of the microtubule lumen	γ = correction factor for off-rate of αTAT from exposed acetylation site relative to the external surface of microtubules

(5) Acetylation events for αTAT molecules inside the lumen

For simplicity, every acetylation site on the inside of the microtubule lumen was assumed to be non-acetylated at the start of the simulation. Then, every acetylation site which was visited by an αTAT1 molecule during the simulation was assumed to be

acetylated, and was flagged as such during the simulation. In addition, for simplicity it was assumed that the affinity (on and off rates) of αTAT1 was identical whether or not a tubulin subunit was acetylated.

(6) Model-convolution image creation

To visualize the localization of αTAT1-GFP and, simultaneously, the fluorescent anti-acetyl antibody pattern on microtubules at the conclusion of each simulation, we performed model-convolution to generate simulated images for comparison to experiments, as previously described [115–117]. Briefly, for the localization simulations, simulated images of αTAT1-GFP were generated by convolving the microscope point spread function with simulated fluorescent markers at the position of each simulated αTAT1-GFP molecule at the completion of a run. Here, the signal and noise were matched to experimental images, and the average fluorescence distribution curves calculated as described above.

Model Parameters and Assumption Summary

The model parameters are summarized in Table S2-4, with formulae for each parameter shown in the appropriate Table S2-1:S2-3. In addition, the simulation parameters are shown in Table S2-5. Finally, key modeling assumptions are summarized in Table S2-6.

Table S2-4: Model Parameters

Symbol	Description	Value Range Tested	Values Used in Main Text Figures	Reference
$k_{on,lattice}^{*}$	αTAT on-rate, lattice exterior	7 s^{-1}	7 s^{-1}	Northrup and Erickson (1992) [106]
$k_{off,lattice}$	αTAT off-rate constant from exterior microtubule lattice	0.1-10 s^{-1}	1 s^{-1}	This study
$<\Delta x_{lattice}>$	Bound αTAT diffusion step size, lattice exterior	40 nm	40 nm	Constrained by experiment (Fig. S5) and similar to Szyk et al (2014) [84]
Pr_enter_{plus}	In the end-entry model, probability of αTAT located at microtubule plus-end to enter the lumen	0.05	0.05	This study, fit to experimental data
Pr_enter_{minus}	In the end-entry model, probability of αTAT located at microtubule minus-end to enter the lumen	0.005	0.005	This study, fit to experimental data
Pr_enter_{defect}	In the lattice entry model, probability of αTAT located randomly along the lattice to enter the lumen	0.05	0.05	Free parameter, selected to achieve rapid steady-state
$k_{on,lumen}^{*}$	αTAT on-rate, lumen interior	10^2 s^{-1}	10^2 s^{-1}	This study, limited by simulation step size
γ	Correction to external lattice αTAT off-rate for lumen interior	0.1 - 1	0.3 - 1	This study, fit to experimental data
$(<\Delta x_{lumen}>^2)^{1/2}$	Free αTAT diffusion step size, lumen interior	16-128 nm	16-64 nm	Range constrained by theoretical argument (Eq. 6)

Table S2-5: Simulation Parameters

Symbol	Description	Values Used in Main Text Figures
t_{dur}	Duration of the simulation	20 min
Δt_{step}	Duration of each time step	0.01 s
$N_{\alpha TAT}$	Number of αTAT molecules in the simulation	100
L_{MT}	Microtubule Length	4864 nm

Table S2-6: Model Assumption Summary

Behavior	Model Assumption	Reference or Explanation
αTAT attachment to microtubule exterior lattice	Weighted random attachment of αTAT according to protofilament density	Free concentration of αTAT uniformly distributed in imaging chamber during in vitro experiments
αTAT behavior on the exterior microtubule lattice	αTAT diffuses on the external microtubule lattice	Observed experimentally and consistent with previous studies [102]
Acetylation behavior	αTAT enters the microtubule lattice to acetylate the α-tubulin dimer; arrival of αTAT on an interior dimer leads to acetylation	Based on previous studies [61,84]
αTAT movement inside microtubule lumen	αTAT diffuses in solution, but rebinds quickly due to the high density of tubulin binding sites inside of the lumen	Theoretical considerations based on density of binding sites [85,106]

Chapter Three

Evolving tip structures can explain age-dependent microtubule catastrophe

Chapter Three is previously published.

103. Coombes, C. E., Yamamoto, A., Kenzie, M. R., Odde, D. J. & Gardner, M. K. Evolving tip structures can explain age-dependent microtubule catastrophe. *Curr. Biol.* **23,** 1342–8 (2013).

Courtney E. Coombes participated in the study design, carried out the TEM experiments, carried out the *in vivo* budding yeast experiments, participated in analysis of data, and participated in drafting the manuscript.

Ami Yamamoto and Madeline R. Kenzie carried out the *in vivo* budding yeast experiments and participated in *in vivo* data analysis.

David J. Odde participated in the design and coding of the 3D Model Simulation.

Melissa K. Gardner conceived of and participated in the design of the study, carried out the *in vitro* TIRF experiments, participated in data analysis and creating the 3D Model Simulation and participated in drafting the manuscript.

All authors read and approved the final manuscript.

Introduction

Microtubules are key structural and transport elements in cells. The dynamics at microtubule ends are characterized by periods of slow growth, followed by stochastic switching events termed ‘‘catastrophes,’’ in which microtubules suddenly undergo rapid shortening [3]. Growing microtubules are thought to be protected from catastrophe by a GTP- tubulin ‘‘cap’’: GTP-tubulin subunits add to the tips of growing microtubules but are subsequently hydrolyzed to GDP-tubulin subunits once they are incorporated into the microtubule lattice [1,25,26]. Loss of the GTP-tubulin cap ex- poses GDP-tubulin subunits at the microtubule tip, resulting in a catastrophe event [27–31]. However, the mechanistic basis for sudden loss of the GTP cap, leading to catastrophe, is not known. To investigate microtubule catastrophe events, we performed 3D mechanochemical simulations that account for interactions between neighboring protofilaments [118–120]. We found that there are two separate factors that contribute to catastrophe events in the 3D simulation: the GTP-tubulin cap size, which settles into a steady-state value that depends on the free tubulin concentration during micro- tubule growth, and the structure of the microtubule tip. Importantly, 3D simulations predict, and both fluorescence and electron microscopy experiments confirm, that microtubule tips become more tapered as the microtubule grows. This effect destabilizes the tip and ultimately contributes to microtubule catastrophe. Thus, the likelihood of a catastrophe event may be intimately linked to the aging physical structure of the growing microtubule tip. These results have important consequences for catastrophe regulation in cells, as microtubule-associated proteins could promote catastrophe events in part by modifying microtubule tip structures.

Results and Discussion

A 3D Mechanochemical Model Predicts Stochastic Catastrophe Events

Growing microtubule tips are stabilized by a GTP-tubulin ‘‘cap,’’ such that loss of the GTP cap exposes GDP-tubulin subunits, resulting in a catastrophe event [27–31]. However, the mechanistic basis for the abrupt loss of the GTP cap, leading to catastrophe, is not known. To investigate microtubule catastrophe events, we performed 3D mechanochemical simulations of microtubule dynamics [118–120]. This type of simulation allows for a detailed dissection of the events that lead up to a simulated catastrophe event and can therefore provide experimentally testable hypotheses for potential

catastrophe mechanisms. Briefly, the 3D simulation accounts for (1) subunit arrivals at the tip of the microtubule, (2) subunit departures from the tip, and (3) stochastic GTP hydrolysis of subunits that are buried in the lattice (Figure 3-1A; See Experimental Methods). In the simulation, a GTP-tubulin subunit is subject to stochastic hydrolysis once it is buried in the lattice by the addition of a single subunit on top of it. Hydrolysis of a buried subunit changes its stability in the lattice, such that GDP-tubulin subunits that are exposed at the microtubule tip will rapidly dissociate from the lattice. In contrast to 1D models, in which protofilaments are regarded as independent entities, the 3D model explicitly accounts for both lateral and longitudinal bonds between tubulin subunits in the lattice. Here, interactions between protofilaments can stabilize subunits in the lattice via bonding with lateral neighbors.

As the stochastic 3D simulation proceeds, the microtubule tip structure naturally evolves as subunits arrive and depart from the tip of each protofilament. In addition, the energetic penalty introduced by stochastic hydrolysis of buried subunits in the lattice produces a behavior in which slow microtubule growth is followed by periods of rapid shortening (Figure 3-1B). We characterized these large, rapid shortening events as catastrophes (Figure 3-1B, black arrows). Note that the smaller shortening events during the growth phase are slower in their off-rate than rapid shortening, and they do not involve uncapping of the microtubule, as described previously [118].

3D Model Simulations Predict Age-Dependent Catastrophe Events

To verify that the simulated dynamic instability behavior approximated previously published in vitro experimental data, we measured catastrophe frequency, growth rates, and shortening rates in the 3D simulation for three different GTP-tubulin concentrations (Figure 3-1C). Growth and shortening rates were consistent with previous experimental observations [104,121]. Simulated catastrophe events occurred more frequently than in previous experimental observations (Figure 3-1C). The simulated catastrophe frequency is strongly influenced by the largely unconstrained hydrolysis rate simulation parameter. For simulations in this work, we conservatively selected a faster hydrolysis rate, which led to smaller cap sizes and relatively short catastrophe times (see Experimental Procedures). However, our conclusions are robust over a range of values for the simulated hydrolysis rate parameter (Figure S3-1).

Previous analysis of in vitro and in vivo data showed that experimental catastrophe frequencies are age dependent: catastrophe events are less likely for young

microtubules, whereas older microtubules catastrophe more frequently [15,34,35,122]. Thus, microtubules accumulate catastrophe-promoting features over time as they grow.

To directly test whether younger microtubules are less likely to catastrophe than older microtubules in the 3D simulation, we calculated the time-dependent catastrophe frequency, $f\pm(t)$, as a function of microtubule age, t [15,34] (see Experimental Procedures). We found that the catastrophe frequency increased as a function of microtubule growing time in the 3D simulation (Figure 3-1D), similar to previous experimental results [15,34,35].

Thus, the 3D simulation predicts that catastrophe-promoting features are accumulated and remembered over time in the microtubule lattice. We then asked whether there were any microtubule features in the simulation that were time dependent, as this could explain why younger microtubules would be less likely to catastrophe than older microtubules.

Tip Structures Exhibit Aging in the 3D Model

It is thought that the growing microtubule tip is protected from catastrophe by a GTP cap [1,25,26,28,29]. Therefore, if the GTP cap size decays as a function of time during microtubule growth, this would lead to increased catastrophe frequency for older microtubules. We tested this mechanism for age-dependent catastrophe by calculating the total number of GTP-tubulin subunits in the lattice at 1 s intervals during simulated microtubule growth and then averaging these values over 10–20 separately growing microtubules. Strikingly, after an initial period of cap establishment, the mean GTP cap size rapidly settled into a steady-state value (Figure 3-2A, green; $t_{1/2}$ ~5 s).

Because the simulated GTP cap size remained constant as a function of microtubule age, we did not see evidence for age-dependent decay of the GTP cap. However, in analyzing the behavior of the 3D simulation, we noted that the microtubule tip structure appeared to be evolving as a function of microtubule age (Figure 3-2B). Therefore, we asked whether the structure of the microtubule tip was changing over time in the simulation, and whether the tip structure configuration could play a role in the initiation of a catastrophe event. The possibility that microtubule tip structure is important for microtubule catastrophe has been suggested in previous modeling efforts [119,123–125].

At any given time, the tip of the microtubule may be blunt (Figure 3-2B, top) or more tapered (Figure 3-2B, bottom). To quantitatively measure changes in simulated microtubule tip structure, we calculated the length (in nm) of each microtubule protofilament within a microtubule and then calculated the standard deviation of

protofilament lengths (which we term ‘‘tip SD’’). For tips that are blunt (Figure 3-2B, top), the tip SD is low, and for tips that are tapered, the tip SD is high (Figure 3-2B, bottom). Thus, we used this metric to evaluate tip structure changes during simulated microtubule growth.

Surprisingly, we found that simulated microtubule tip structures were not constant over time but rather became increasingly more tapered as the microtubule grew. This effect is demonstrated in the animated simulation output (Figure 3-2B), which shows the tip SD increasing over time. The quantitative tip SD results demonstrate that the microtubule tips start out blunt when they nucleate from the seed (time = 0) but then in- crease in taper as the microtubule grows (Figure 3-2A, purple). We note that the individual microtubule tips are highly dynamic and therefore have rapidly fluctuating tip structures (see Figure 3-2A inset for typical individual tip SD traces over time). Therefore, the monotonic increase in tip SD represents an average behavior over 10–20 simulated microtubules.

We then asked how tubulin concentration would affect tip structure evolution. We did this by comparing the tip SDs of younger (‘‘early’’) and older (‘‘late’’) microtubules (black arrows in Figure 3-2A denote specific time periods analyzed). We found that higher free tubulin concentrations led to a faster evolution of tip structures with time, such that the simulated tip SDs were larger at both early and late time periods for higher tubulin concentrations (Figure 3-2C). The simulation prediction that overall tip structures are more tapered at higher free tubulin concentrations is consistent with electron microscopy data [37,126] and with our previous experimental results using total internal reflection fluorescence (TIRF) microscopy [104]. However, even though simulated tip structures were more tapered with increasing free tubulin concentration, the striking difference in tip SD between early and late time points was present regardless of concentration (Figure 3-2C).

Because the on-rate of GTP-tubulin subunits increases at higher free tubulin concentrations (while the hydrolysis rate remains constant), the overall simulated GTP cap size in- creases with increasing free tubulin concentration (Figure 3-2D). However, in contrast to the tip SD, the average GTP cap size does not depend on microtubule age: the cap size remained constant regardless of early or late time points at all simulated tubulin concentrations (Figure 3-2D). Thus, the simulated GTP cap size is not aging. In contrast, there is a large difference in catastrophe frequency between the early and late time points regardless of tubulin concentration (Figure 3-2E). Therefore, we

conclude that (1) the simulated microtubules are aging, such that catastrophe events are more likely for older microtubules than for young, early-growing microtubules, and (2) the aging process may be dictated by an increase in tip SD over time, such that microtubule tips evolve from a blunt configuration for young microtubules to more tapered tips for older microtubules.

Tip Structures Demonstrate Aging for In Vitro Microtubules as Measured by TIRF Microscopy

The 3D simulation predicts that catastrophe events are more frequent for older, longer microtubules. This observation is consistent with previously published in vitro experimental results, which demonstrated that the catastrophe frequency of a microtubule depends on the length of time that the microtubule has been growing [15,34,35]. Therefore, the simulation prediction that microtubule tip structures become more tapered over time may provide a key insight into the age-dependent mechanism of catastrophe.

Using TIRF microscopy of microtubules grown in vitro, we directly tested the simulation prediction that tip structures evolve during microtubule growth, such that the tips become more tapered over time. Here, we used green Alexa 488- labeled GTP-microtubules grown from coverslip-attached rhodamine-labeled GMPCPP seeds, as described previously [127], and collected single-time-point images of different green microtubules growing from the red seeds (Figure 3-3A, top). We analyzed the green microtubule extensions by measuring green fluorescence intensity as a function of distance from the red/green transition point (Figure 3-3A, bottom) and then calculated the average fluorescence intensity distributions as a function of microtubule length (Figure 3-3A, bottom).

Qualitative examination of the fluorescence intensity data suggests that the green microtubule-associated fluorescence drops off more quickly to background when microtubules are short (Figure 3-3A, left, red), as compared to the longer microtubules (Figure 3-3A, left, blue). To quantitatively compare the drop-off in fluorescence intensity at microtubule ends, we calculated the microtubule tip SD by fitting the fluorescence data at microtubule ends to a Gaussian survival function, as described previously [104,105]. This approach allows for quantitative evaluation of microtubule end structures with nanometer-scale resolution using fluorescence microscopy, such that smaller tip SD values correspond to blunt microtubule tips and larger tip SD measurements correspond to tapered microtubule ends. Consistent with our qualitative observations, we found that

the microtubule tip SD was increased for longer microtubule lengths (Figure 3-3A, right; probability of zero slope for 7 mM: p < 5 3 1024). In addition, higher tubulin concentrations led to more rapid tip structure evolution as compared to low concentrations, such that larger experimental tip SDs were observed at 8 and 12 mM tubulin (Figure 3-3A, right, magenta and purple) as compared to 7 mM (green) for similar microtubule lengths. Thus, similar to simulation predictions (Figure 3-2C), in vitro microtubule tip structures evolve as a function of time, and higher tubulin concentrations lead to a faster tip structure evolution. These results are also consistent with our measurements of in vitro EB1-GFP distribution as a function of microtubule length (Figure S3-2).

Tip Structures Demonstrate Aging for In Vitro Microtubules as Measured by Electron Microscopy

To verify our quantitative TIRF microscopy results, we used transmission electron microscopy (TEM) to directly measure microtubule tip structures. Here, we evaluated the ‘‘tip extension’’ length by measuring the difference between the shortest and the longest protofilaments at the microtubule tip (Figure 3-3B). A small difference in protofilament lengths is typical of a blunt tip (Figure 3-3B, left, red arrows), whereas a larger difference in protofilament lengths at a microtubule tip is typical of a tapered tip (Figure 3-3B, left, yellow arrows). We found that, similar to our fluorescence microscopy measurements, increasing tip extension lengths were observed for longer microtubules relative to shorter microtubules (Figure 3-3B, right). Our TEM results are similar to previously published cryo-electron microscopy (cryo-EM) results in which longer tip extensions were observed as a function of longer microtubule assembly times (Figure S3-3) [37], and our independent measurements of these previously published cryo-EM images demonstrate that tip extension length increases for longer microtubules as well (Figure S3-3).

Tip Structures Demonstrate Aging for In Vivo Budding Yeast Microtubules as Measured by TIRF Microscopy

Our experimental results confirm the simulation prediction that in vitro tip structures evolve during microtubule growth, such that microtubule tips become more tapered over time. To assess whether microtubules inside of cells also evolve during growth, we used TIRF microscopy to visualize microtubules in wild-type yeast cells that

were labeled with GFP-Tub1 and Bim1-mCherry (Figure 3-3C). Bim1 is the yeast homolog of the plus-end binding protein EB1 and thus similarly targets the tips of growing microtubules [128]. We collected single-time- point images of individual microtubules growing from spindle poles (Figure 3-3C). As in the in vitro studies, we analyzed the green microtubules by measuring green fluorescence intensity as a function of microtubule length. As above, qualitative examination of the binned fluorescence intensity data suggests that the green microtubule-associated fluorescence drops off more quickly to background when microtubules are short (Figure 3-3D, left, red), as compared to the longer microtubules (Figure 3-3D, left, purple). However, the presence of multiple microtubules captured at the spindle pole results in higher fluorescence immediately at the pole. Therefore, we limited our quantitative analysis to the data points near to the micro- tubule tip (Figure 3-3D, left, discarded points circled in black). In addition, we collected independent data on the spatial distribution (‘‘signal width’’) of the Bim1-mCherry fluorescence (Figure 3-3D, center).

To quantitatively compare the drop-off in tubulin-GFP fluorescence intensity at microtubule plus ends, we calculated the microtubule tip SD as described above [35,123]. Consistent with our in vitro data, we found that the microtubule tip SD increased for longer microtubule lengths (Figure 3-3D, right, green). In addition, the increase in micro- tubule tip SD for longer microtubules was correlated with a redistribution of Bim1-mCherry localization at the microtubule tip: the Bim1-mCherry signal width was broader for longer microtubules (Figure 3-3D, right, red). Thus, similar to simulation predictions (Figure 3-2C), we conclude that in vivo microtubule tip structures become more tapered over time. These results are consistent with previous in vivo observations of age-dependent catastrophe behavior in neuronal microtubules [122].

Tip Structure Aging Is Independent of GTP Hydrolysis

The 3Dsimulation predicts that tip structures are more tapered for older, longer microtubules, and also that this tip structure aging process is independent of GTP hydrolysis rate (Figure S3-1). To test this prediction, we used GMPCPP, which is a slowly hydrolyzable analog of GTP [129]. Here, Alexa 488-labeled GMPCPP-microtubules were grown from coverslip- attached rhodamine-labeled GMPCPP seeds, and the green microtubule extensions were then analyzed as described above to quantitatively evaluate microtubule end structures (Figure 3-3E, left). We found that the microtubule tip SD was higher at longer microtubule lengths even in the absence of GTP hydrolysis

(Figure 3-3E). In addition, a higher free GMPCPP-tubulin concentration also led to more tapered tips (Figure 3-3E, right; 0.7 mM GMPCPP-tubulin [blue] versus 1.6 mM GMPCPP-tubulin [red]). Therefore, we conclude that the microtubule tip structure aging process does not require GTP hydrolysis.

Disruption of Tip Structure Aging Leads to Loss of Age-Dependent Catastrophe in Simulation

If catastrophe events are sensitive to microtubule tip structure, it may be that microtubule-associated proteins could promote catastrophe events in cells by modifying microtubule tip structures. Thus, we tested whether a simulated molecular motor that acts specifically to modify microtubule tip structures could change the dependence of catastrophe frequency on microtubule aging.

To test whether stochastic modification of microtubule tip structures by a microtubule-associated protein could change the overall catastrophe behavior of microtubules, a tip-modifying molecular motor was added to the 3D microtubule simulation (Figure 3-4A, left). Similar to previously published data on the depolymerizing kinesin-13 molecular motor MCAK, the simulated molecular motor randomly attached to a microtubule and diffused along a microtubule until it reached the microtubule end [130,131] (simulation parameters in Table S3-1).

Once at the microtubule end, the simulated motor acted to outwardly curl its attached protofilament, processively moving toward the microtubule minus end with the depolymerizing protofilament [132]. Importantly, this type of motor activity disrupted the evolution of simulated tip structures: the microtubule tip SD did not monotonically increase as a function of growth time, as was observed in control simulations (Figure 3-4A, center; compare to Figure 3-2A). Rather, the motor produced fluctuating tip structures after a short initial elongation period.

Strikingly, disruption of tip structure evolution also disrupted the age dependence of catastrophe. Similar to previously published experimental results for MCAK [15], the dependence of catastrophe frequency on microtubule age was reduced as compared to control simulations (Figure 3-4A, right, compare to Figure 3-1D). These results confirm that catastrophe events are linked to tip structures in the 3D mechanochemical simulation.

Because MCAK has been reported to be a catastrophe promoter that disrupts the age-dependent catastrophe process [8,15,131], we were curious as to whether the presence

of MCAK would also disrupt in vitro microtubule tip structure as measured by fluorescence microscopy. Thus, we experimentally evaluated microtubule tip structures as described above, only we modified the described assay by adding 9 nM MCAK, as described previously [15](Figure 3-4B, left). Similar to the simulation results with a protofilament kinking motor (Figure 3-4A), we found that the measured tip SD did not steadily increase as a function of microtubule length, as was observed for the control microtubules (Figure 3-4B, right). Rather, the microtubule tip was moderately tapered at short microtubule lengths and then remained similarly tapered regardless of microtubule length. These results are consistent with the hypothesis that tip structure evolution is related to the aging process for microtubule catastrophe.

Conclusions

The microtubule tip becomes more tapered over time as a microtubule grows, both experimentally and in simulation. We propose that the evolution of tip structures during microtubule growth provides a natural explanation for age-dependent catastrophe. Here, new microtubules first start growing with a blunt tip, which does not predispose a microtubule to catastrophe, and thus young microtubules will have a lower catastrophe frequency (Figure 3-4C, left). However, as a microtubule grows, the tip structure becomes more tapered, which ultimately acts to destabilize the microtubule and increase the likelihood of a catastrophe event (Figure 3-4C, left).

Why would an increase in tip taper predispose a microtubule to catastrophe? One possibility is that a tapered tip could lead to a gradient in tubulin subunit off-rates from the end: while a majority of the protofilament tips are relatively stable, protofilaments at tapered tips with fewer lateral neighbors could be quite unstable and thus represent ‘‘hot spots’’ for GTP cap loss (Figure 3-4C, right: note blue/green tubulin subunit stability gradient due to tapered tip configuration). In this fashion, GTP cap loss on a critical number of unstable protofilaments could thus predispose a microtubule with a highly tapered tip structure to catastrophe.

Similar to previous work [123], we propose that there may be a critical minimum number of unstable protofilaments that strongly predispose a microtubule to catastrophe. This idea is consistent with the observation that the simulated tip structure effect appears to saturate at higher tip SDs (Figure 3-4C, left). Here, additional unstable protofilaments past a critical minimum number may not have a substantial effect on increasing catastrophe frequency. The average microtubule tip structure depends on

tubulin concentration, such that tip structures are more tapered at higher tubulin concentrations. We hypothesize that catastrophe frequency is regulated both by the size of the GTP cap and also by the tip structure configuration at the end of a growing microtubule. Here, increasingly tapered and unstable tip structures at moderate tubulin concentrations could antagonize the stabilizing effect of a larger cap size with increasing tubulin concentrations (Figure 3-4D, left). However, the tip structure effect may ultimately saturate at high tubulin concentrations, and the stabilizing effect of a substantial GTP cap would then begin to dominate (Figure 3-4D, left, blue) [133]. This speculative model could explain previously published in vitro data in which the net microtubule lifetime is relatively constant at moderate tubulin concentrations but increases rapidly at higher concentrations (Figure 3-4D, right) [15,121,134].

We conclude that the likelihood of a catastrophe event is intimately linked to the aging physical structure of the growing microtubule tip. As a consequence, microtubule-associated proteins at substoichiometric concentrations could promote catastrophe events in part by modifying microtubule tip structures inside of cells.

Acknowledgements

The authors thank Mark McClellan for experimental technical assistance. We also thank Joe Howard and Marija Zanic for the gift of EB1-GFP protein and for helpful discussions. This work was supported by the Pew Scholars Program in the Biomedical Sciences (supported by the Pew Charitable Trusts) (M.K.G.) and National Institutes of Health grants GM103833 (M.K.G.) and GM071522 (D.J.O.). The TEM work was carried out in the Characterization Facility at the University of Minnesota, a member of the National Science Foundation-funded Materials Research Facilities Network (www.mrfn.org), via the Materials Research Science and Engineering Centers program.

Figures

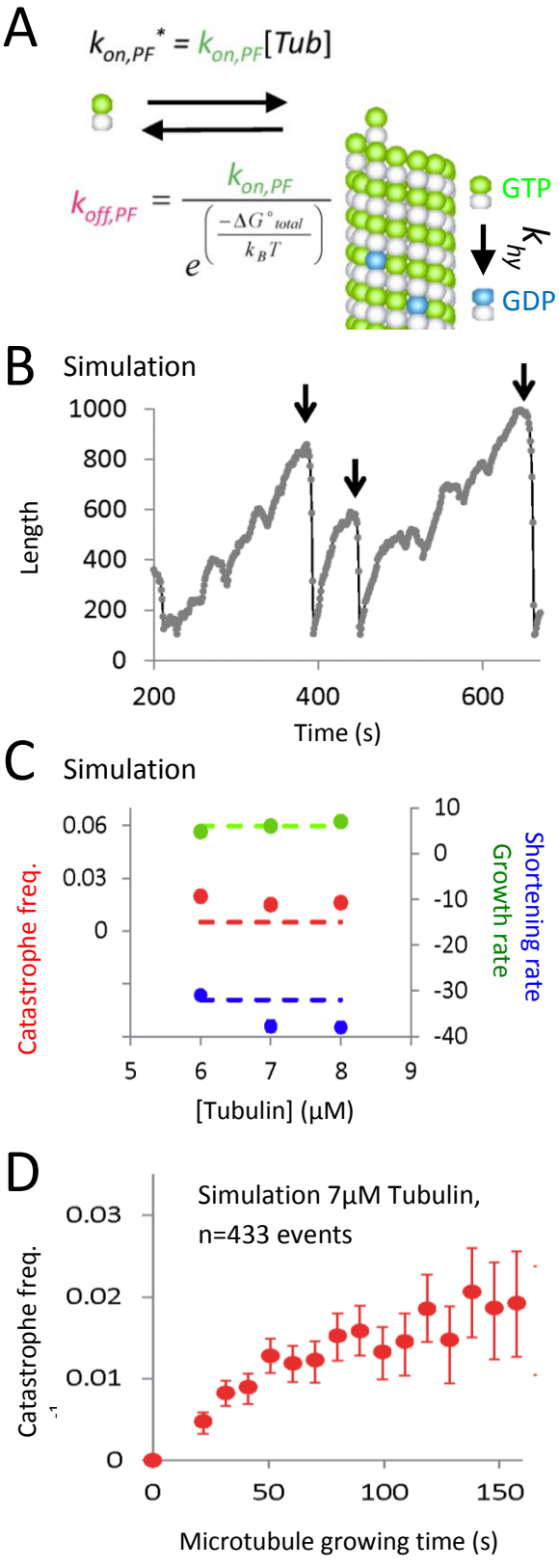
A
$k_{on,PF}^{*} = k_{on,PF}[Tub]$
$k_{off,PF} = \frac{k_{on,PF}}{e^{\left(\frac{-\Delta G^{\circ}_{total}}{k_B T}\right)}}$
GTP
k_{hy}
GDP
B
Simulation
Length
1000
800
600
400
200
0
200
400
600
Time (s)
C
Simulation
Catastrophe freq.
0.06
0.03
0
Growth rate
Shortening rate
10
0
-10
-20
-30
-40
5
6
7
8
9
[Tubulin] (µM)
D
Simulation 7µM Tubulin,
n=433 events
Catastrophe freq.
0.03
0.02
0.01
0
0
50
100
150
Microtubule growing time (s)

Figure 3-1: 3D Mechanochemical Model Predicts Age-Dependent Catastrophe
(A) The 3D simulation accounts for subunit arrivals at the tip of the microtubule (kon, PF*) and subunit departures from the tip (koff, PF*) [120]. Stochastic GTP hydrolysis occurs at a constant rate (khydrolysis) [119], which imposes an energetic penalty on DG total that favors subunit loss (kB = Boltzmann's constant, T = absolute temperature). (B) The 3D simulation predicts growth events followed by catastrophe (black arrows). (C) Growth rates (green markers), shortening rates (blue markers), and catastrophe frequencies (red markers) are compared to experimental data (dashed lines [15]). (D) Simulated catastrophe frequency versus microtubule growth time. Error bars represent SE. See also Figure S3-1 and Table S3-1.

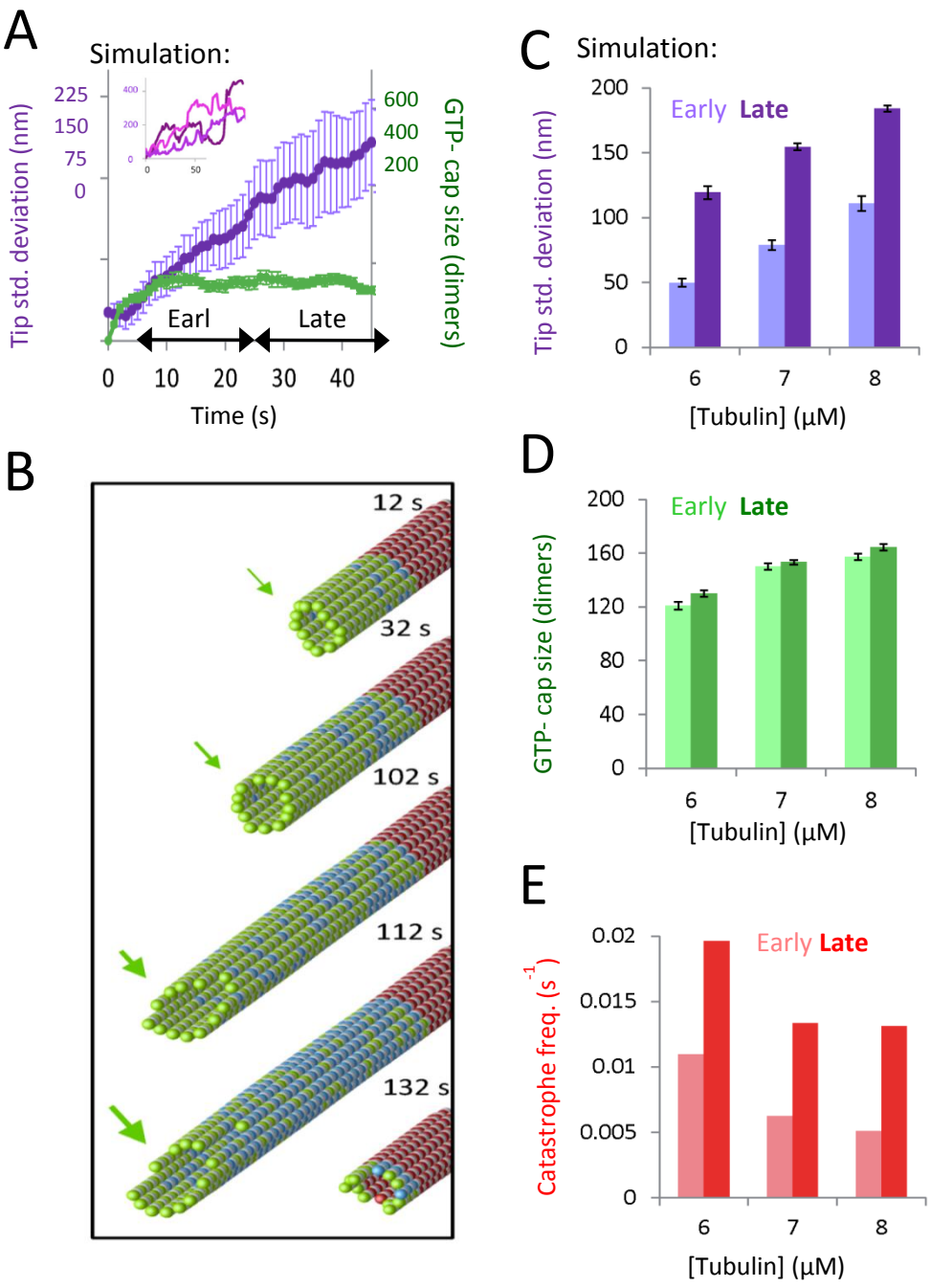

Figure 3-2: The 3D Simulation Predicts that Microtubule Tips Become More Tapered Over Time While the Average GTP-Cap Size Remains Stable (A) After initial rapid growth, the GTP cap size remains stable (green). In contrast, the tip SD increases monotonically with growth time (purple, 7 mM tubulin, n = 14; inset shows three individual microtubule traces). (B) Animated simulation output over time (red, GMPCPP seed; green, GTP tubulin; blue, GDP tubulin). (C–E) Simulated tip SD (C), GTP cap size (D), and catastrophe frequency (E) are shown at early and late time points. Error bars represent SE. See also Figure S3-1.

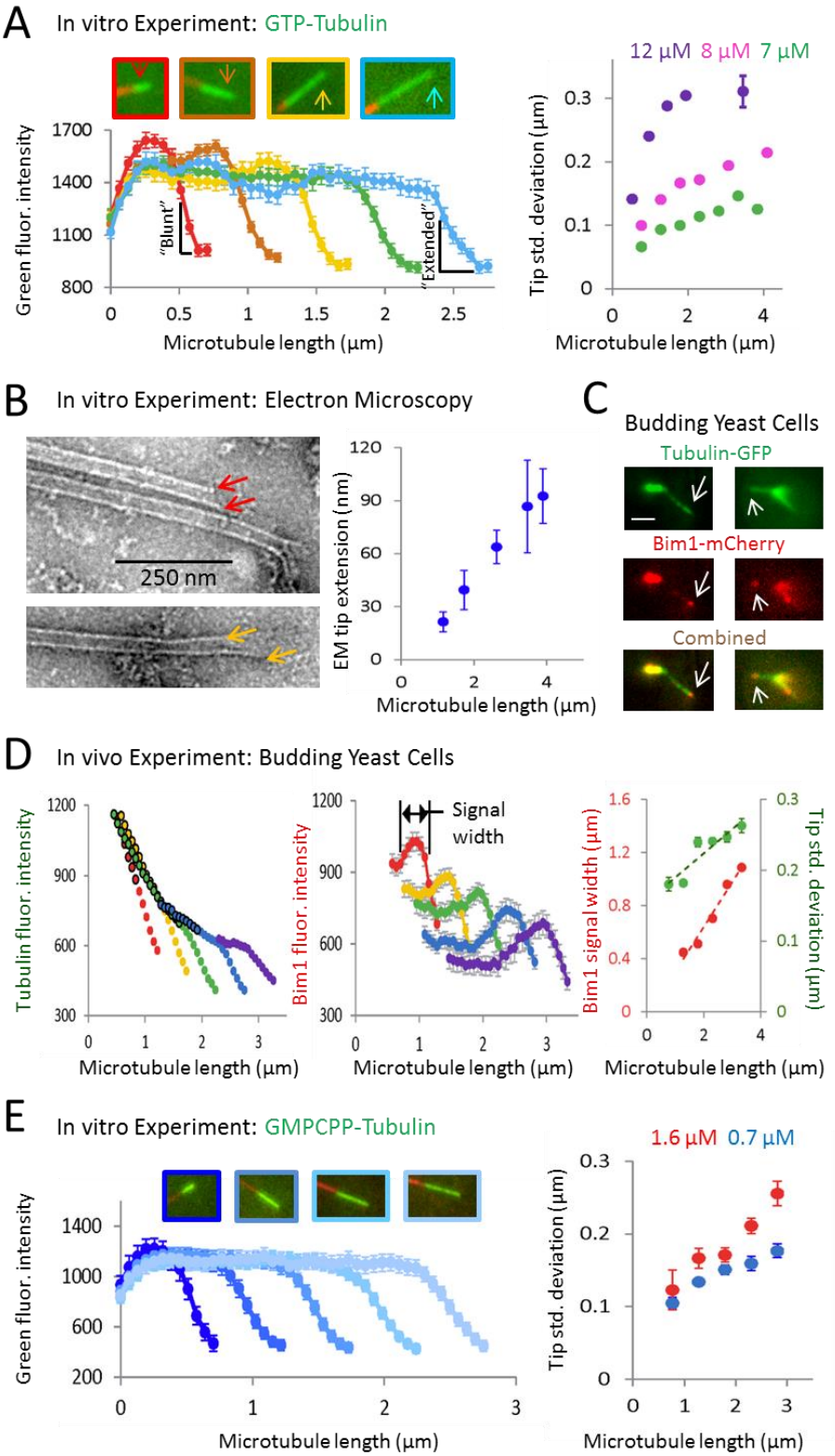
A
In vitro Experiment: GTP-Tubulin
Green fluor. intensity
Microtubule length (μm)
"Blunt"
"Extended"
12 μM 8 μM 7 μM
Tip std. deviation (μm)
Microtubule length (μm)
B
In vitro Experiment: Electron Microscopy
250 nm
EM tip extension (nm)
Microtubule length (μm)
C
Budding Yeast Cells
Tubulin-GFP
Bim1-mCherry
Combined
D
In vivo Experiment: Budding Yeast Cells
Tubulin fluor. intensity
Microtubule length (μm)
Bim1 fluor. intensity
Signal width
Microtubule length (μm)
Bim1 signal width (μm)
Tip std. deviation (μm)
Microtubule length (μm)
E
In vitro Experiment: GMPCPP-Tubulin
Green fluor. intensity
Microtubule length (μm)
1.6 μM 0.7 μM
Tip std. deviation (μm)
Microtubule length (μm)

Figure 3-3: Tip Taper Increases with Microtubule Age, Both In Vitro and In Vivo (A) Green Alexa 488 GTP-tubulin microtubule extensions were grown from red GMPCPP-stabilized seeds (left, top). Green fluorescence intensity is plotted as a function of distance from the red/green transition point (left, bottom). Quantitative tip standard is estimated by Gaussian survival function fitting (right). (B) Tip structures were directly measured using TEM (red arrows denote a blunt tip; yellow arrows denote a more tapered tip; n = 29 microtubules). (C) Microtubules are dual labeled in budding yeast cells: Green GFP-Tub1 labels microtubules, and red Bim1-mCherry labels microtubule plus ends. Scale bar represents 2 mm. (D) Both the microtubule tip SD (green) and the Bim1 signal width (red) increase as a function of in vivo microtubule length (right). (E) Green Alexa 488 GMPCPP microtubule extensions were grown from red GMPCPP-stabilized seeds (left, top). The average fluorescence intensity as a function of microtubule length is plotted (left, bottom). GMPCPP-tubulin microtubule tips are more tapered at longer microtubule lengths (right; red: 1.6 mM GMPCPP-tubulin; blue: 0.7 mM GMPCPP-tubulin). Error bars represent SE. See also Figures S3-2 and S3-3.

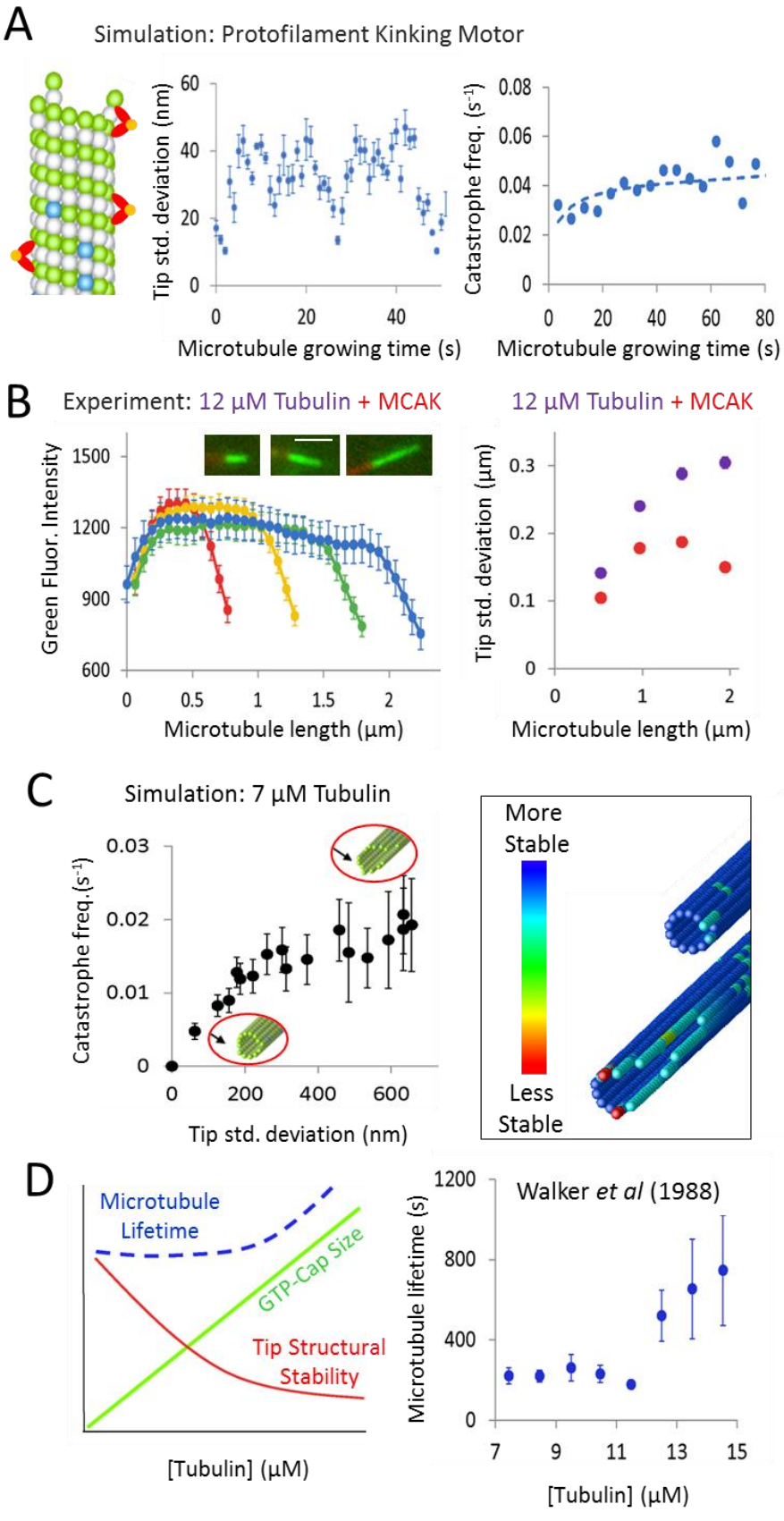
A
Simulation: Protofilament Kinking Motor
Tip std. deviation (nm)
Microtubule growing time (s)
Catastrophe freq. (s-1)
Microtubule growing time (s)
B
Experiment: 12 µM Tubulin + MCAK
12 µM Tubulin + MCAK
Green Fluor. Intensity
Microtubule length (µm)
Tip std. deviation (µm)
Microtubule length (µm)
C
Simulation: 7 µM Tubulin
Catastrophe freq.(s-1)
Tip std. deviation (nm)
More Stable
Less Stable
D
Microtubule Lifetime
GTP-Cap Size
Tip Structural Stability
[Tubulin] (µM)
Walker et al (1988)
Microtubule lifetime (s)
[Tubulin] (µM)

Figure 3-4: A Model for Age-Dependent Microtubule Catastrophe. (A) A protofilament-kinking molecular motor is added to the 3D simulation (left), which disrupts the microtubule tip structure, such that the tip structure evolves quickly and then fluctuates (center). As a result, microtubule catastrophe frequency is relatively constant as a function of microtubule growing time (right). (B) The depolymerizing molecular motor MCAK disrupts microtubule tip structures, similar to simulation results for a protofilament-kinking molecular motor (purple, tubulin controls; red, tubulin plus MCAK). Scale bar represents 2 mm. (C) Simulated catastrophe frequency is higher for more tapered tip structures (left). Here, catastrophe frequency data from Figure 3-1D are plotted against the tip SD data from Figure 3-2A by selecting the appropriate values for each at similar microtubule growing times. Increased off-rates at tapered tips could create localized ‘‘hot spots’’ of less stable subunits (right, green versus blue). (D) A speculative model for the antagonistic effects of tip structure and GTP cap. Here, increasingly tapered and destabilized tip structures at moderate tubulin concentrations (left, red) could antagonize the stabilizing effect of the GTP cap size (left, green). However, the tip structure effect may ultimately saturate at high tubulin concentrations, such that the stabilizing effect of a substantial GTP cap would then begin to dominate (left, blue). This model could explain previously published in vitro data in which the net microtubule lifetime is relatively constant at moderate tubulin concentrations but increases rapidly at higher concentrations (right, [121]). Note that these data were digitized from Walker et al. 1988 and then transformed from catastrophe frequency (s21) into lifetime (s) by taking the inverse of each number. Error bars represent SE. See also Table S3-2.

Supplemental Material and Methods

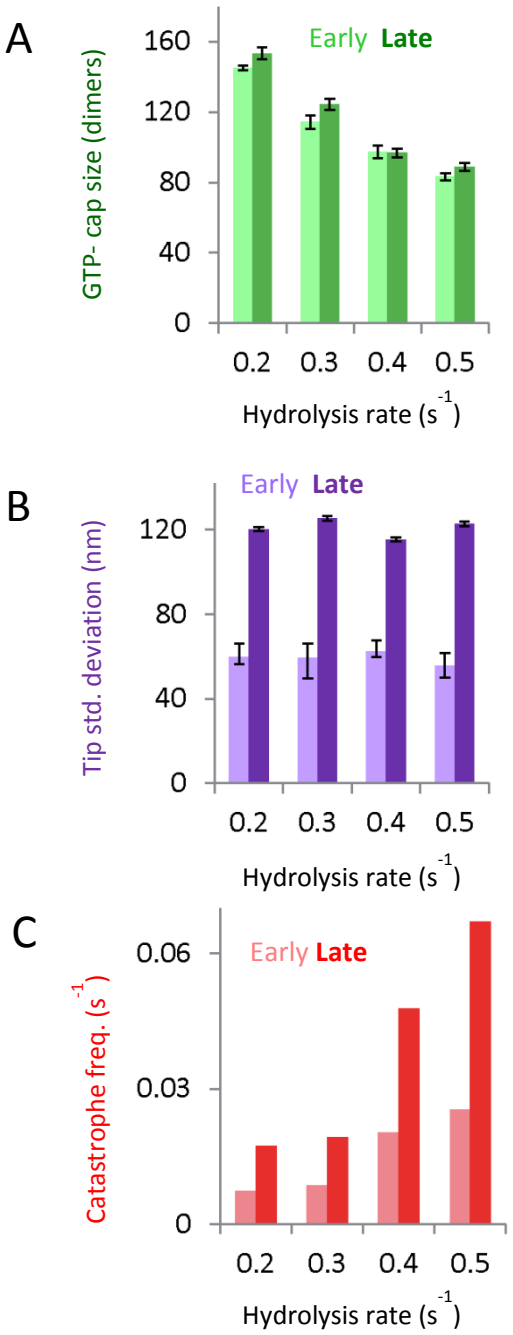

Figure S3-1: Effect of Hydrolysis Rate on 3D Simulation Results, Related to Figures 1 and 2. (A) Increasing the simulated GTP-hydrolysis rates results in decreasing GTP cap sizes, although GTP cap size does not change as a function of microtubule age, regardless of the GTP-hydrolysis rate used in the simulation. (B) In contrast, the tip structure aging is independent of GTP-hydrolysis rate over all tested values: the tip standard deviation is smaller at early time points and larger at late time points, regardless of hydrolysis rate. This result suggests that simulated tip structures may evolve as a result of microtubule assembly kinetics, independent of GTP-hydrolysis. (C) Similarly, catastrophe frequency is lower for young microtubules and higher for older microtubules, regardless of the simulated hydrolysis rate.

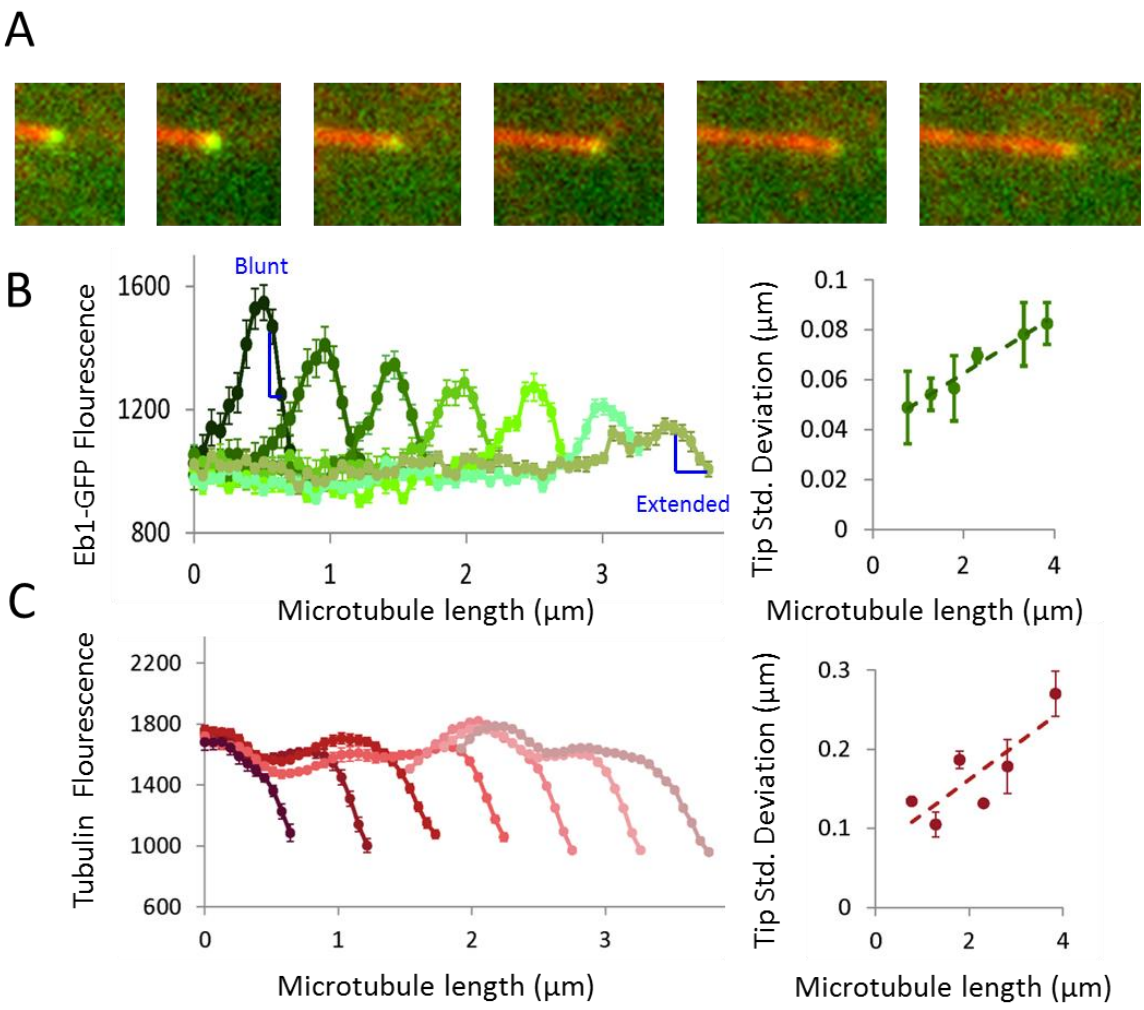

Figure S3-2: In Vitro Localization of EB1 as a Function of Microtubule Length, Related to Figure 3. (A) Similar to previous reports for Mal3-GFP, EB1-GFP intensity becomes more diffuse as a function of length for growing in vitro microtubules [135]. (B) By averaging in vitro EB1-GFP intensity as a function of microtubule length at 7 µM GTP-tubulin, we find that the average EB1-GFP intensity becomes more diffuse for longer microtubules (left). By fitting the fall-off in EB1-GFP intensity at microtubule tips to a Gaussian function, the apparent microtubule tip standard deviation, as reflected by EB1-GFP fluorescence, increases as a function of microtubule length (right). (C) Similarly, the Alexa-568 tubulin fluorescence can be averaged at different microtubule lengths, leading to an increasing tip standard deviation as a function of microtubule length.

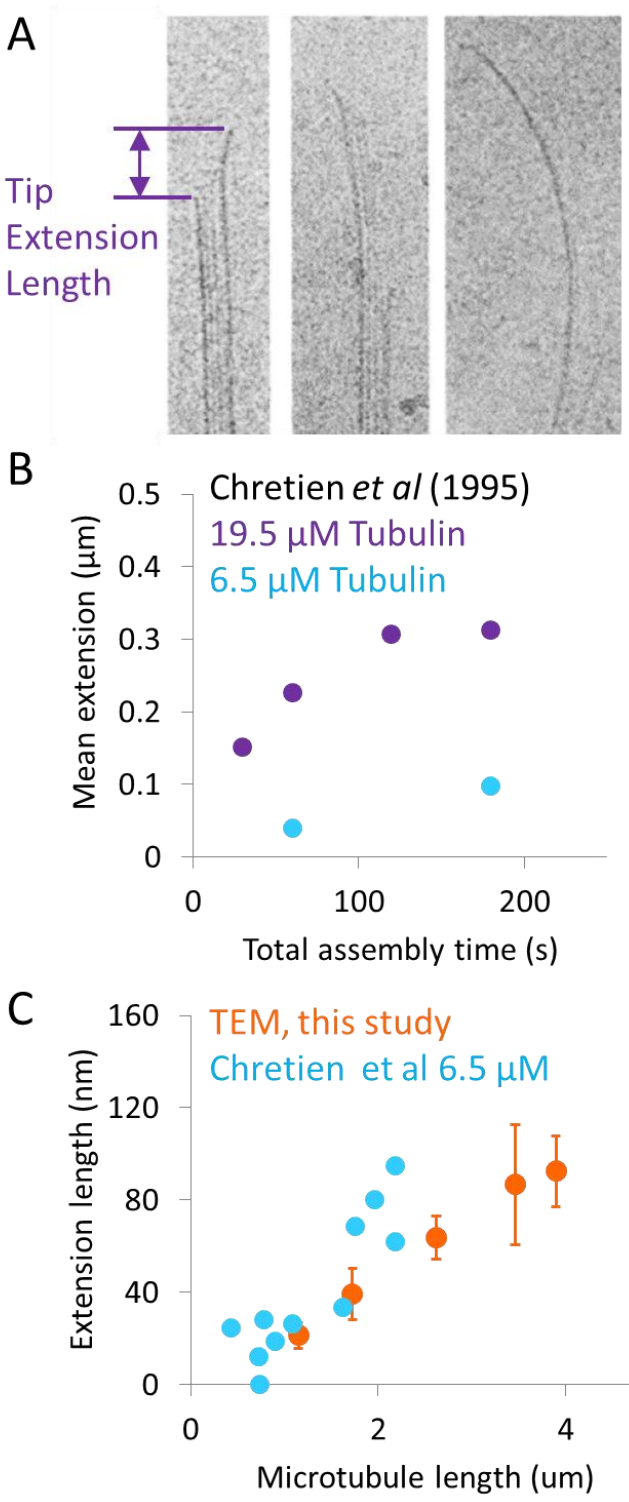
A
Tip
Extension
Length
B
Chretien *et al* (1995)
19.5 µM Tubulin
6.5 µM Tubulin
Mean extension (µm)
0.5
0.4
0.3
0.2
0.1
0
0
100
200
Total assembly time (s)
C
TEM, this study
Chretien et al 6.5 µM
Extension length (nm)
160
120
80
40
0
0
2
4
Microtubule length (um)

Figure S3-3: Relationship of Current Work to Previous Cryo-electron Microscopy Studies, Related to Figure 3. (A) Cryo-electron microscopy images reproduced from Chretien *et al.* (1995) [37] demonstrate the observation and measurement of extended tip structures. (B) Data reproduced from Table 4 in Chretien *et al.* (1995): "Measurements of Microtubule End Extensions at Different Tubulin Concentrations and Assembly Times". Data shown is for 19.5 μM and 6.5 μM GTP-tubulin, and demonstrates that mean tip extension length increases with total assembly time. (C) To directly compare measurements of tip extension length as a function of microtubule length, microtubules in Figure 7A of Chretien *et al.* (1995) (6.5 μM GTP-tubulin) were measured using ImageJ. In this published image, the entire microtubule lengths are visible, so both microtubule length and tip extension length could be measured. Results from Chretien *et al.* (1995) are similar to TEM data from the current study.

Methods

Simulation Methods: Microtubule Assembly

Briefly, the 3D simulation accounts for (1) subunit arrivals at the tip of the microtubule, (2) subunit departures from the tip and (3) stochastic GTP hydrolysis of subunits that are buried in the lattice (Fig. 3-1A). The tubulin subunit arrival rate is calculated as shown in Fig. 3-1A [120]. After addition to the lattice, a GTP-tubulin subunit is subject to first-order stochastic hydrolysis once it is buried in the lattice by the addition of a single longitudinal neighbor on top of it. Hydrolysis of a buried subunit changes its preferred angle in the lattice, and therefore results in mechanical strain between lateral and longitudinal neighbors [119]. To explicitly account for mechanical and chemical energetic differences between tubulin subunits at the microtubule tip based on their lateral and longitudinal neighbor configurations, the subunit departure rate from a given protofilament, $k_{off,PF}$, depends on the equilibrium constant, where

$$K_{eq} \equiv \frac{k_{on,PF}}{k_{off,PF}} = e^{-\Delta G^0_{total}/k_B T} \qquad (1a)$$

Therefore, by rearrangement:

$$k_{off,PF} = \frac{k_{on,PF}}{e^{-\Delta G^0_{total}/k_B T}} \qquad (1b)$$

where $k_{off,PF}$ is the off-rate per individual protofilament (s^{-1}), k_B is Boltzmann's constant, T is absolute temperature, and ΔG^0_{total} is the total free energy of the stabilizing bonds on a specific subunit, given by

$$\Delta G^0_{total} = \sum \Delta G^{0*}_{Longitudinal} + \sum \Delta G^0_{Lateral} \qquad (2)$$

Here, $\Delta G^{0*}_{Longitudinal}$ is the total longitudinal bond energy for a given subunit, and $\Delta G^0_{Lateral}$ is the total lateral bond energy for a given subunit. Both lateral and longitudinal bond energies are penalized by bending and stretching, which decreases the stability of both lateral and longitudinal bonds, and thus increases the off-rate of the associated tubulin subunit from the lattice. We note that the details for how GDP subunits are destabilized

at the tips of microtubules remains an open question. However, the essential feature of the model in regards to catastrophe is that GDP tubulin subunits have a high probability of leaving the lattice when exposed at the tip. While the simulation assumes that this destabilization is accomplished via protofilament kinking, as curled protofilaments have been observed in depolymerizing microtubules, the mechanism for destabilization of GDP tubulin subunits at microtubule tips is not critical to the model results.

As the stochastic 3D model computer simulation proceeds, the microtubule tip structure naturally evolves as subunits arrive and depart from the tip of each protofilament. In addition, the bending and stretching energy penalty introduced by stochastic hydrolysis of buried subunits in the lattice produces a behavior in which slow microtubule growth is followed by periods of rapid shortening (Fig. 3-1B). In analyzing simulation results, we characterize these events as catastrophes (Fig. 3-1B, black arrows). Simulations were performed using MATLAB (Mathworks, Version 7.7, Natick, MA), as described previously [119], with exceptions as described below. Simulation parameters are listed in Table S3-1.

In 2002, the Odde and Cassimeris labs published a “2D” model for microtubule assembly [120], and in the current paper, we have used a “3D” model simulation for microtubule assembly, as described in Van Buren et al (2005) [119]. However, the parameterization is identical between these two models, except that the energetic penalty for a GDP-tubulin subunit in the lattice was assigned a value $\Delta G_{Kink} = 2.1 - 2.5$ k_BT in the 2002 paper, while in the current work the energetic penalty for a GDP-tubulin subunit is calculated based on the degree of lateral and longitudinal stretching exhibited by an individual kinked subunit at the tip of a microtubule using a Hookean spring law equation (see Van Buren et al (2005), eqn 24 [119]). The Young’s modulus and preferred kinking angle parameters used in the current simulations result in a similar value for the GDP-tubulin energetic penalty of $\Delta G_{Kink} = 4.3$ k_BT. Therefore, although the relationship between tip structure and catastrophe frequency was not studied in previous work, we expect that catastrophe behavior is similar between the two models.

In order to properly simulate our *in vitro* experiments, we switched to a “3-state” model in the simulation. Here, all simulations started with a microtubule “seed” that was composed of GMPCPP tubulin. Simulation parameters for the GMPCPP seeds are as

shown in Table S3-1, and are similar to previous work [104] . Briefly, subunits could dissociate from the tip of a GMPCPP-seed, however, the GMPCPP-tubulin subunits in the seed did not hydrolyze, and so the effective off-rate for GMPCPP-tubulin subunits from the seed was low relative to the GTP/GDP-tubulin extensions which grew from the seed.

Inclusion of a stable GMPCPP seed in the simulation eliminated the requirement for starting the simulation with an arbitrary GTP-cap size, and so allowed dynamic microtubules to naturally nucleate from the seed and thus develop a GTP-cap as part of the assembly process. In addition, when catastrophe events were observed in the simulations, new microtubules could naturally re-nucleate from the simulated GMPCPP-seed, thus allowing for multiple cycles of dynamic instability. The rules for GTP-tubulin assembly from the GMPCPP seed were similar to the previously described 3D model [119], where GTP-tubulin subunits were stochastically incorporated at the microtubule tip, and were then stochastically hydrolyzed to GDP-tubulin once the subunits were buried in the lattice.

Calculating age-dependent catastrophe times

To directly test whether younger microtubules are less likely to catastrophe than older microtubules in the 3D model simulation, we calculated the time-dependent catastrophe frequency, $f_{\pm}(t)$, as a function of microtubule age, t, as previously described [15,34], as follows:

$$f_{\pm}(t) = \frac{dF(t)/dt}{1 - F(t)} \qquad (1)$$

Where $F(t)$ is the cumulative distribution of catastrophe times [15,34]. In Fig. 3-5A, we are plotting the catastrophe frequency data from Fig. 3-1D against the tip standard deviation data from Fig. 3-2A by selecting the appropriate values for each at similar microtubule growing times.

Table S3-1: Simulation Parameters: Tubulin Self-Assembly

Parameter	Description	Value
[GTP-tub]	Free GTP-tubulin concentration	$6x10^{-6}$ M (for catastrophe simulations)
[GMPCPP-tub]	Free GMPCPP-tubulin concentration	0 M (assumption)
$k_{on,MT}$	Tubulin on-rate constant per MT	65 $\mu M^{-1}s^{-1}$ MT^{-1} [104,118–120]
$k_{hyd,\ GTP}$	Hydrolysis rate constant per GTP-tubulin subunit	0.2-0.5 $s^{-1}subunit^{-1}$
$k_{hyd,\ GMPCPP}$	Hydrolysis rate constant per GMPCPP-tubulin subunit	~0 $s^{-1}subunit^{-1}$ [104]
$\Delta G^{0*}_{Long,GTP}$	Longitudinal chemical bond energy (GTP-tubulin polymer)	-7.2 k_BT [104,118–120]
$\Delta G^{0}_{Lat,GTP}$	Lateral chemical bond energy (GTP-tubulin polymer)	-5.7 k_BT [104,118–120]
$\Delta G^{0*}_{Long,GMPCPP}$	Longitudinal chemical bond energy (GMPCPP-tubulin polymer)	-7.2 kBT (matched to GTP in simulation)
$\Delta G^{0}_{Lat,GMPCPP}$	Lateral chemical bond energy (GMPCPP-tubulin polymer)	-5.7 k_BT (matched to GTP in simulation)
EI_{MT}	Flexural rigidity of a microtubule	$4x\ 10^{-24}Nm^2$ [119]
$\theta_{GTP,pref}$	Preferred angle for GTP-tubulin	0° [119]
$\theta_{GDP,pref}$	Preferred angle for GDP-tubulin	22° [119]
$\theta_{GMPCPP,pref}$	Preferred angle for GMPCPP-tubulin	0° (assumed)

Simulation Methods: Kinking Motor

The above-described microtubule self-assembly simulation was also run with the inclusion of a depolymerizing molecular motor. Here, a single molecular motor was added to the simulation. This was an "MCAK-like" motor, which randomly attached to a single protofilament (based on a weighted protofilament-length array), and then diffused along the protofilament (no directed motion) until (a) the motor randomly detached from the protofilament, or (b) the motor arrived at the protofilament plus-end. Once at the plus-end of a protofilament, the motor acted to change the preferred angle of GTP-tubulin subunits to match that used for GDP-tubulin subunits (22°). The motor had no effect on tip-associated GDP or GMPCPP tubulin subunits. If a tubulin subunit that was associated with a motor detached, then the motor would move to the next tubulin subunit towards the minus-end, ie, the motor tracked depolymerizing protofilaments. This continued until the motor stochastically dissociated from the protofilament. In general, motor activities (attach, move, or detach) occurred at every time step, after a tubulin-associated event (association, dissociation, or hydrolysis). Simulation parameters for the motor are in Table S3-2.

The one-dimensional diffusion assumption for the "MCAK-like" motor in the simulation was made for computational simplicity, as the method in which the simulated motor arrives at the microtubule end does not affect its ultimate role in kinking the protofilaments at the end of the simulated microtubules. However, this assumption does not necessarily reflect the behavior of MCAK on the lattice [131,136].

Table S3-2: Simulation Parameters: Depolymerizing Motor

Parameter	Description	Value
D_{mcak}	Motor diffusion coefficient on microtubule lattice	0.38 $\mu m^2 s^{-1}$ [130]
N_{motor}	Number of motors in simulation	1
$k_{on,MCAK}$	Motor on-rate constant (per concentration of polymerized tubulin)	2 $\mu M^{-1}s^{-1}$
$k_{off,\ MCAK}$	Motor off-rate on lattice	10 s^{-1}
$k_{off,MCAK,END}$	Motor off-rate at plus-end	20 s^{-1}
$\theta_{GTP,MCAK}$	Preferred angle for GTP-Tubulin subunit at plus-end WITH motor present	22°

Analysis of Simulation Results

Because of the large data sets generated from simulations, the simulation data analysis was automated in MATLAB. When simulations were run, the following data was recorded every after every 1 s of simulated microtubule self-assembly:

Table S3-3: Simulation Recorded Data

Recorded Parameter	Description	Units
t	Elapsed time since start of simulation	s
L_{MT}	Median protofilament length	nm
σ_{tip}	Standard deviation of protofilament lengths	nm
n_{added}	Number of subunits added in the 1 s interval	--
n_{lost}	Number of subunits lost in the 1 s interval	--

Once simulations were complete, this data was automatically read in to a custom MATLAB program. Catastrophe events were defined by n_{lost} for a given 1 second time step: for the 6 μM tubulin catastrophe simulations, if n_{lost} was >550 tubulin subunits, this was counted as a catastrophe event. This metric is reasonable given that the stochastic tubulin subunit on-rate for the 6 μM simulation was 390 subunits/sec. Using this method, the simulated catastrophe times (defined as the elapsed time from the start of microtubule growth until catastrophe) were measured. Then, catastrophe frequency was calculated as a function of microtubule growing time, as previously described [15,34].

In vitro *TIRF Microscopy Experimental Methods*

To perform *in vitro* analysis of dynamic microtubule tip structures, Alexa-488 labeled GTP-tubulin microtubules were grown from rhodamine-labeled GMPCPP-tubulin microtubule seeds, as previously described [114]. Briefly, the GMPCPP-seeds were attached via surface bound anti-rhodamine antibodies to cleaned and silinized coverslips within a parafilm-constructed flow chamber. The reaction mixture included imaging buffer, as previously described [15]. TIRF microscopy using a Nikon Eclipse *Ti* microscope with Nikon CFI Apochromat 100X 1.49 NA oil objective was then used to image the green GTP microtubules growing from cover-slip attached red GMPCPP seeds. An Andor $iXon_3$ EM-CCD camera fitted with a 2.5X projection lens was used to

capture images with small pixel size (64 nm in the field/pixel). Since fluorescence intensity was analyzed along the length of microtubules, single-plane/single-shot images in different areas along the flow chamber were taken once microtubules in the chamber achieved steady-state. Therefore, no time-lapse imaging was performed in this study, and no images were subjected to more than one laser exposure.

Because the microtubule shortening rate is ~10-fold faster than the growing rate, we expected that the vast majority of observed microtubules would be in the growing state. However, to verify that the presence of a small population of shortening microtubules would not affect our results, we performed one experiment at 8 μM GTP-tubulin in which we collected 3-4 frames in each field of view. Then, the microtubules were screened such that the first frame of each series was used for analysis, but only the microtubules which remained in the growing state through all 3-4 frames were selected for the analysis. This data is shown in Fig. 3-3B (magenta), and is consistent with the other data sets.

In vivo *Yeast Imaging Experimental Methods*

Yeast cells labeled with GFP-Tub1 and SPC110-mCherry spindle pole markers were imaged using TIRF microscopy on a Nikon Eclipse *Ti* microscope with Nikon CFI Apochromat 100X 1.49 NA oil objective, and an Andor iXon$_3$ EM-CCD camera fitted with a 2.5X projection lens. As with the *in vitro* experiments, only single-plane/single-shot images were collected to avoid complications with photobleaching in analyzing *in vivo* tip structures.

To prepare for imaging, yeast cells were grown overnight at 26°C in 25ml YPD + 100μl 100x adenine, and then diluted into 15ml YPD + 100μl 100x adenine 2 hours prior to imaging. Cells were immobilized during imaging on a coverslip to allow for TIRF imaging. To do this, we soaked coverslips overnight in 1 M aqueous NaOH, and then washed with nanopure water. The coverslips were allowed to dry, and then used to build parafilm-sealed flow chambers. We then adhered the cells to the coverslips in the flow chambers by introducing concanavalin-A into a flow chamber for 20 minutes at room temperature. Excess concanavalin-A was then washed out of the chamber and replaced with water. Cells were introduced into the chamber and naturally adhered to the

concanavalin-A-coated coverslip. After 10-15 minutes, unadhered cells were vacuumed from the chamber, and then water with glucose was introduced for imaging.

Image Analysis

Images were analyzed identically for *in vitro* microtubule and for budding yeast *in vivo* experiments. Here, custom MATLAB code was used to quantify fluorescence intensity as a function of position along the length of a fluorescent microtubule. Because this measurement is inherently noisy, we grouped single images of many different microtubules together by length, and then calculated average curves for each length group. Thus, each microtubule was sorted by length in 512 nm increments (8 pixels), and then the fluorescence was rebinned into a normalized number of pixels according to the average length of the assigned group. For example, a microtubule of length 1344 nm (21 pixels) would be assigned to the microtubule length group from 1024-1536 nm (16-24 pixels), and so the fluorescence would be rebinned into (16+24)/2=20 normalized pixels. The method for rebinning fluorescence into a normalized number of pixels was as previously described [116].

To collect the fluorescence intensity data as a function of position, cropped, color-combined images were analyzed using the custom MATLAB code. Here, the operator used a screen cursor to click first on the red/green transition between the seed (or spindle pole), and the green GTP-tubulin microtubule extension. Then the operator used the screen cursor to click again just outside of the microtubule tip, by aligning the edge of the cursor on the tip so that the cursor center was aligned just outside of the tip. Using these two click locations, the MATLAB code calculated the fluorescence intensity at each position between the two clicks by integrating fluorescence ±4 pixels above and below the line connecting the two endpoints. Thus, an average data set of fluorescence intensity by pixel position was built up for a variety of microtubule lengths. This is the data that is plotted in Figs. 3-3A, 3-3E, and 3-4D.

To calculate the “tip standard deviation” from the TIRF fluorescence intensity data, we used the approach as previously described in [104,105]. Briefly, the distance (or position) and corresponding average fluorescence intensity data for each average microtubule length was read in to a MATLAB program which then fit the Gaussian survival function to

the microtubule fluorescence intensity data, starting from the flat distribution along the length of the microtubule (the initial rise in fluorescence intensity was attributed to the transition between the seed (or spindle pole body) and the growing microtubule, and so was ignored). In this way, if the fluorescence intensity dropped quickly at the tip of the microtubule, the standard deviation of the Gaussian survival function ("tip standard deviation") was low, which is consistent with a "blunt" microtubule tip. In contrast, if the fluorescence intensity dropped more gradually at the tip of the microtubule, the tip standard deviation was high, which is consistent with a more extended microtubule tip (i.e., which has a large standard deviation in protofilament lengths).

Statistical Analysis

All error bars on simulation graphs represent the standard error of the mean (SEM), either calculated directly, or (in the case of Fig. 3-1D) calculated via error propagation.

Error bars on the experimental fluorescence intensity curves also represent SEM. To calculate error bars for the fitted tip standard deviation of each microtubule length, a 95% confidence interval for the tip standard deviation was calculated during the Gaussian survival function fit, and then this interval was divided by 1.96 to estimate the standard deviation of the estimated parameter. This value was then divided by $N^{½}$ to calculate SEM.

Electron Microscopy Experimental Methods

To visualize microtubules using room-temperature transmission electron microscopy (TEM), the microtubules were grown in a mixture of BRB80, GTP (1 mM), unlabeled tubulin (9 μM), and purified centrosomes at 37˚C on a 300-mesh carbon coated copper grid. This was done for 2 minutes using an environmental device as previously described [136]. After 2 minutes, and while still holding the grid in the warm, humid air stream, the grid was immediately stained with 1% uranyl acetate for 1 minute. The stain was then wicked away with filter paper and the grid was left to dry. Specimens were observed using an FEI Technai Spirit BioTWIN transmission electron microscope. Images were recorded at 11,000X at -3 to -5 defocus. Microtubule length and microscope zoom were carefully regulated to ensure that entire microtubules could be

visualized in the TEM field of view. Therefore, both the microtubule length as well as the difference between the longest visible protofilament and the shortest visible protofilament could be directly measured. Data was analyzed using the image processing package Fiji (Image J).

The grid contained a mixture of polymerizing and depolymerizing microtubules, and we distinguished the depolymerizing microtubules by their characteristic curled-back plus-end protofilaments. These microtubules were not included in the analysis.

Chapter Four

Thesis Conclusions and Discussion

The primary conclusion of my thesis work is that the microtubule structure affects its interactions with other proteins, like αTAT1, and also its own dynamics. The mechanisms and characterizations of the processes described in this work are novel and important. First, we verified that αTAT1's main entryway to the lumen is at microtubule ends, and not through lattice breathing as once theorized (Figure 2-1 and 2-2, [61,83,86]), and that the rate or likelihood of entry is likely dependent on the structure at the microtubule ends. Specifically, αTAT1 is more likely to bind and enter the lumen of a microtubule with a tapered end versus a microtubule with a blunt end (Figure 2-1B). Second, we determined that the position of lysine 40 of α-tubulin within the hollow lumen of the microtubule dictates how efficiently the microtubule can be acetylated. When the microtubule structure is intact and the ends are blunt, αTAT1 entry is rare and the diffusion down the lumen is slow (Figure 2-3). The efficiency of microtubule acetylation can be increased by disrupting the microtubule structure to allow access to the luminal K40 sites (Figure 2-4). Third, we found that αTAT1 can create tapered microtubule ends and act as a slow depolymerase (Figure 2-5). Finally, we found that tapered microtubule ends are correlated with age dependent microtubule catastrophe (Figure 3-3), and may be the mechanism by which some depolymerases, including αTAT1, induce microtubule depolymerization.

How αTAT1 accesses the microtubule lumen to bind and acetylate the α-tubulin K40 residues has been a topic of debate [74,84,137]. This is in part because initial studies published with α-tubulin acetylation staining in cells showed dispersed, relatively uniform sections of acetylation along microtubules [52]. It was thought that uniform patterning of acetylation could only be caused if the microtubule acetyltransferase was able to enter the lumen at any position along the microtubule, or if the unstructured loop where K40 resides was able to escape the lumen during protofilament breathing. This last mechanism was particularly attractive because the acetylated K40 residues would then be positioned on the outer surface of the lattice and thus able to directly interact with microtubule associated proteins such as motor proteins.

However, our work supports a model in which αTAT1 primarily enters the microtubule lumen via its ends, and not at any position along the length of the lattice. This is in line with other studies that found gradients of acetylation from the ends of axonemes [74]. End entry may be facilitated by other proteins in cells by increasing the probability of αTAT1 arriving at microtubule ends. One study showed that the clathrin adaptor protein AP2 binds to and directs αTAT1 to the ends of microtubules during cell

migration [112]. Still, we did find that αTAT1 can enter the lumen along the length of the lattice if the microtubule had structural defects such as at bends (Figure 2-4). This type of luminal access may be more important in cells where microtubules would be more susceptible to bends and breaks. Additionally, acetylation can also occur more uniformly when αTAT1 enters the lumen of dynamic microtubules (Figure 2-3C).

Once αTAT1 has entered the lumen, we demonstrated that it is unable to efficiently diffuse down the length of the lumen. In solution αTAT1 would be able to diffuse quickly, however because there is a large concentration of potential binding sites within the small volume of the lumen, αTAT1 is likely to continually bind the K40 sites (Figure 2-2F-G). This continual rebinding would drastically decrease the time αTAT1 spends diffusing in solution, and thus decrease the distance it is able to travel prior to rebinding (Figure 2-6A-C). Furthermore, we found that rapid αTAT1 rebinding directly depends on αTAT1 affinity for the K40 binding sites (Figure 2-6D-E). In cells, higher salt concentrations may decrease the affinity of αTAT1 to K40 sites, and thus allow for longer stretches of microtubule acetylation. This may be particularly true in very stable microtubule networks such as in neuronal axons.

In addition to modifying the acetylation state of microtubules, we found that αTAT1 can change the structure at microtubule ends. Specifically, when microtubules are incubated with αTAT1, either with or without acetyl CoA present, there was reduced fluorescence at the microtubule ends compared to control microtubules (Figure 2-5A). This is suggestive of more tapered microtubule tips. The tapering effect at the ends may be contributing to more αTAT1 binding in a cooperative manner (Figure 2-5C). Additionally, the increase in microtubule end tapering with αTAT1 incubation is correlated with slow depolymerization. When incubated with αTAT1 for several hours, microtubules are on average much shorter than microtubules incubated without αTAT1 for the same periods of time (Figure 2-5B). A related process was described in Kalebic et al., where increased expression of αTAT1 in mammalian cells led to microtubule destabilization. Interestingly, this effect did not require αTAT1 acetyltransferase activity [80], similar to the microtubule end tapering effect described in our work (Figure 2-5A). It is possible that in cells, αTAT1 can remodel the microtubule network either by destabilizing microtubules or by acetylating α-tubulin subunits. How and in what context this occurs will be an important topic of future study.

The mechanism by which αTAT1 is able to destabilize dynamic microtubules may be intimately linked to its effect on microtubule ends. The tapering at ends may create

unstable protofilaments that have fewer lateral neighbors, and thus may be more susceptible to catastrophe. We found that this same tapering increases naturally as microtubules grow for longer periods of time and/or lengths (Figure 3-3). The evolution of the microtubule end from blunt to tapered provides a logical explanation for age-dependent microtubule catastrophe (Figure 3-4C). Additionally, microtubule associated proteins, including αTAT1, could manipulate microtubule end structures to influence microtubule dynamics in cells.

There are several different and exciting avenues of research that follow from the work presented here. First, not all microtubules are acetylated in cells, and some networks are much more highly acetylated than others. These highly acetylated networks tend to be stable, and it is not yet known how these microtubules accumulate acetylation. Theoretically, two different mechanisms could be contributing to the accumulation of acetylation on stable microtubules. The first is that αTAT1 preferentially binds and/or preferentially acetylates stable microtubules in cells. Because stable microtubule networks have lifetimes on the order of hours and dynamic microtubules have lifetimes on the order of minutes, acetylation may accumulate on stable microtubules because of the long amount of time for αTAT1 to both diffuse (this work) and enzymatically transfer an acetyl group to K40 sites [84]. The second possible mechanism is that αTAT1 binds and acetylates all microtubules, but destabilizes dynamic microtubules at a higher rate or efficiency than stable microtubules. This action would similarly result in an accumulation of acetylation on stable microtubule networks. However, in this model, acetylation may be important for fine-tuning the function of dynamic microtubule networks. In dynamic microtubule networks, αTAT1 may be acting with different binding partners to specifically acetylate those microtubules. Identifying these binding partners could reveal the cellular processes in which acetylation is modulating microtubule function.

Similarly, it will also be important to elucidate the general function of microtubule acetylation. As of now, several different and distinct functional changes have been described, such as increasing the processivity of certain motor proteins [55,57], but a clear universal effect of microtubule acetylation is not yet known. Finally, more work needs to be done to understand how microtubule acetylation is contributing to or alleviating human disease.

References

1. Nogales, E., Wolf, S. G. & Downing, K. H. Structure of the αβ tubulin dimer by Electron Crystallography. *Nature* **391,** 199–204 (1998).

2. Weisenberg, R. C., Deery, W. J. & Dickinson, P. J. Tubulin-nucleotide interactions during the polymerization and depolymerization of microtubules. *Biochemistry* **15,** 4248–4254 (1976).

3. Mitchison, T. & Kirschner, M. Dynamic instability of microtubule growth. *Nature* **312,** 237–42 (1984).

4. Inoué, S. & Salmon, E. D. Force generation by microtubule assembly/disassembly in mitosis and related movements. *Mol. Biol. Cell* **6,** 1619–40 (1995).

5. Dogterom, M. & Bernard, Y. Measurement of the Force-Velocity Relation for Growing Microtubules. *Science (80-.).* **278,** 856–860 (1997).

6. Kalisch, S. M., Laan, L. & Dogterom, M. Force generation by dynamic microtubules in vitro. *Curr. Opin. Cell Biol.* **17,** 67–74 (2005).

7. Belotti, D. *et al.* The Drug Paclitaxel Has Antiangiogenic. *Clin. Cancer Res.* **2,** 1843–1849 (1996).

8. Desai, A., Verma, S., Mitchison, T. J. & Walczak, C. E. Kin I kinesins are microtubule-destabilizing enzymes. *Cell* **96,** 69–78 (1999).

9. Tournebize, R. *et al.* Control of microtubule dynamics by the antagonistic activities of XMAP215 and XKCM1 in Xenopus egg extracts. *Nat. Cell Biol.* **2,** 13–9 (2000).

10. Walczak, C. E., Mitchison, T. J. & Desai, A. XKCM1: A Xenopus kinesin-related protein that regulates microtubule dynamics during mitotic spindle assembly. *Cell* **84,** 37–47 (1996).

11. Goshima, G., Wollman, R., Stuurman, N., Scholey, J. M. & Vale, R. D. Length control of the metaphase spindle. *Curr. Biol.* **15,** 1979–1988 (2005).

12. Rogers, G. C. *et al.* Two mitotic kinesins cooperate to drive sister chromatid separation during anaphase. *Nature* **427,** 364–370 (2004).

13. Maney, T., Hunter, A. W., Wagenbach, M. & Wordeman, L. Mitotic centromere-associated kinesin is important for anaphase chromosome segregation. *J. Cell Biol.* **142,** 787–801 (1998).

14. Kline-Smith, S. L. & Walczak, C. E. The Microtubule-destabilizing Kinesin XKCM1 Regulates Microtubule Dynamic Instability in Cells. *Mol. Biol. Cell* **13,** 2718–2731 (2002).

15. Gardner, M. K., Zanic, M., Gell, C., Bormuth, V. & Howard, J. Depolymerizing kinesins Kip3 and MCAK shape cellular microtubule architecture by differential control of catastrophe. *Cell* **147,** 1092–1103 (2011).

16. Gardner, M. K. *et al.* Chromosome Congression by Kinesin-5 Motor-Mediated Disassembly of Longer Kinetochore Microtubules. *Cell* **135,** 894–906 (2008).

17. Gupta, M. L., Carvalho, P., Roof, D. M. & Pellman, D. Plus end-specific depolymerase activity of Kip3, a kinesin-8 protein, explains its role in positioning the yeast mitotic spindle. *Nat. Cell Biol.* **8,** 913–923 (2006).

18. Tischer, C., Brunner, D. & Dogterom, M. Force- and kinesin-8-dependent effects in the spatial regulation of fission yeast microtubule dynamics. *Mol. Syst. Biol.* **5,** 250 (2009).

19. Wargacki, M. M., Tay, J. C., Muller, E. G., Asbury, C. L. & Davis, T. N. Kip3, the yeast kinesin-8, is required for clustering of kinetochores at metaphase. *Cell Cycle* **9,** 2581–2588 (2010).

20. McNally, F. J. & Vale, R. D. Identification of katanin, an ATPase that severs and disassembles stable microtubules. *Cell* **75,** 419–429 (1993).

21. Gard, D. L. & Kirschner, M. W. A microtubule-associated protein from Xenopus eggs that specifically promotes assembly at the plus-end. *J. Cell Biol.* **105,** 2203–2215 (1987).

22. Noetzel, T. L., Drechsel, D. N., Hyman, A. A. & Kinoshita, K. A comparison of the ability of XMAP215 and tau to inhibit the microtubule destabilizing activity of XKCM1. *Philos. Trans. R. Soc. Lond. B. Biol. Sci.* **360,** 591–4 (2005).

23. Moores, C. A. *et al.* Distinct roles of doublecortin modulating the microtubule

cytoskeleton. *EMBO J.* **25,** 4448–57 (2006).

24. Carlier, M. F. & Pantaloni, D. Kinetic analysis of guanosine 5'-triphosphate hydrolysis associated with tubulin polymerization. *Biochemistry* **20,** 1918–1924 (1981).

25. Carlier, M. F., Hill, T. L. & Chen, Y. Interference of GTP hydrolysis in the mechanism of microtubule assembly: an experimental study. *Proc. Natl. Acad. Sci. U. S. A.* **81,** 771–775 (1984).

26. Nogales, E. & Wang, H. W. Structural mechanisms underlying nucleotide-dependent self-assembly of tubulin and its relatives. *Curr. Opin. Struct. Biol.* **16,** 221–229 (2006).

27. Voter, W. A., O'Brien, E. T. & Erickson, H. P. Dilution-induced disassembly of microtubules: Relation to dynamic instability and the GTP cap. *Cell Motil. Cytoskeleton* **18,** 55–62 (1991).

28. Walker, R. A., Inoue, S. & Salmon, E. D. Asymmetric behavior of severed microtubule ends after ultraviolet-microbeam irradiation of individual microtubules in vitro. *J. Cell Biol.* **108,** 931–937 (1989).

29. Walker, R. A., Pryer, N. K. & Salmon, E. D. Dilution of individual microtubules observed in real time in vitro: Evidence that cap size is small and independent of elongation rate. *J. Cell Biol.* **114,** 73–81 (1991).

30. Caplow, M. & Shanks, J. Evidence that a single monolayer tubulin-GTP cap is both necessary and sufficient to stabilize microtubules. *Mol. Biol. Cell* **7,** 663–75 (1996).

31. Drechsel, D. N. & Kirschner, M. W. The minimum GTP cap required to stabilize microtubules. *Curr. Biol.* **4,** 1053–1061 (1994).

32. Howard, J. *Mechanics of Motor Proteins and the Cytoskeleton*. (Sunderland, MA: Sinauer Associates, Inc., 2001).

33. Phillips, R., Kondev, J., Theriot, J. & Garcia, H. *Physical Biology of the Cell*. (London: Taylor & Francis Group, 2012).

34. Odde, D. J., Cassimeris, L. & Buettner, H. M. Kinetics of microtubule catastrophe assessed by probabilistic analysis. *Biophys. J.* **69,** 796–802 (1995).

35. Odde, D. J., Buettner, H. M. & Cassimeris, L. Spectral analysis of microtubule assembly dynamics. *AIChE J.* **42,** 1434–1442 (1996).

36. Seetapun, D., Castle, B. T., McIntyre, A. J., Tran, P. T. & Odde, D. J. Estimating the microtubule GTP cap size in vivo. *Curr. Biol.* **22,** 1681–7 (2012).

37. Chrétien, D., Fuller, S. D. & Karsenti, E. Structure of growing microtubule ends: two-dimensional sheets close into tubes at variable rates. *J. Cell Biol.* **129,** 1311–28 (1995).

38. Janke, C. & Bulinski, J. C. Post-translational regulation of the microtubule cytoskeleton: mechanisms and functions. *Nat. Rev. Mol. Cell Biol.* **12,** 773–86 (2011).

39. Hernault, S. W. L. & Rosenbaum, J. L. Chlamydomonas α-Tubulin is Posttranslationally Modified by Acetylation on the ϵ-Amino Group of a Lysine. *Biochemistry* 473–478 (1985). doi:10.1021/bi00323a034

40. Piperno Gianni, Ledizet Michel, C. X. Microtubules Containing Acetylated a-Tubulin in Mammalian Cells in Culture. *J. Cell Biol.* **104,** 289–302 (1987).

41. Schatten, G. *et al.* Acetylated α-tubulin in microtubules during mouse fertilization and early development. *Dev. Biol.* **130,** 74–86 (1988).

42. Sale, W. S., Besharse, J. C. & Piperno, G. Distribution of acetylated alpha-tubulin in retina and in vitro-assembled microtubules. *Cell Motil. Cytoskeleton* **9,** 243–253 (1988).

43. Cambray-Deakin, M. A. & Burgoyne, R. D. Posttranslational modifications of α-tubulin: Acetylated and detyrosinated forms in axons of rat cerebellum. *J. Cell Biol.* **104,** 1569–1574 (1987).

44. Black, M. M. & Keyser, P. Acetylation of alpha-tubulin in cultured neurons and the induction of alpha-tubulin acetylation in PC12 cells by treatment with nerve growth factor. *J Neurosci* **7,** 1833–1842 (1987).

45. Dráberová, E., Viklický, V. & Dráber, P. Exposure of lumenal microtubule sites after mild fixation. *Eur. J. Cell Biol.* **79,** 982–985 (2000).

46. Li, H., Derosier, D. J., Nicholson, W. V, Nogales, E. & Downing, K. H. Microtubule Structure at 8 A Resolution. *Structure* **10,** 1317–1328 (2002).

47. Nogales, E., Whittaker, M., Milligan, R. A. & Downing, K. H. High-Resolution Model of the Microtubule. *Cell* **96,** 79–88 (1999).

48. Soppina, V., Herbstman, J. F., Skiniotis, G. & Verhey, K. J. Luminal Localization of α-tubulin K40 Acetylation by Cryo-EM Analysis of Fab-Labeled Microtubules. *PLoS One* **7,** e48204 (2012).

49. Piperno, G. & Fuller, M. T. Monoclonal Antibodies Specific for an Acetylated Form of a-Tubulin Recognize the Antigen in Cilia and Flagella from a Variety of Organisms. **101,** 2085–2094 (1985).

50. Cambray-deakin, M. A. & Burgoyne, R. D. Acetylated and Detyrosinated a-Tubulins Are Co-Localized in Stable Microtubules in Rat Meningeal Fibroblasts. *Cell Motil. Cytoskeleton* **8,** 284–291 (1987).

51. Black, M. M., Baas, P. W. & Humphries, S. Dynamics of a-Tubulin Deacetylation in Intact Neurons. *J. Neurosci.* **9,** (1989).

52. Schulze, E., Asai, D. J., Bulinski, J. C. & Kirschner, M. Posttranslational modification and microtubule stability. *J. Cell Biol.* **105,** 2167–77 (1987).

53. Webster, D. R. & Borisy, G. G. Microtubules are acetylated in domains that turn over slowly. *J. Cell Sci.* **92,** 57–65 (1989).

54. Belmadani, S., Poüs, C., Fischmeister, R. & Méry, P. F. Post-translational modifications of tubulin and microtubule stability in adult rat ventricular myocytes and immortalized HL-1 cardiomyocytes. *Mol. Cell. Biochem.* **258,** 35–48 (2004).

55. Reed, N. a *et al.* Microtubule acetylation promotes kinesin-1 binding and transport. *Curr. Biol.* **16,** 2166–72 (2006).

56. Misawa, T. *et al.* Microtubule-driven spatial arrangement of mitochondria promotes activation of the NLRP3 inflammasome. *Nat. Immunol.* **14,** 454–60

(2013).

57. Dompierre, J. P. *et al.* Histone deacetylase 6 inhibition compensates for the transport deficit in Huntington's disease by increasing tubulin acetylation. *J. Neurosci.* **27,** 3571–83 (2007).

58. Sudo, H. & Baas, P. W. Acetylation of microtubules influences their sensitivity to severing by katanin in neurons and fibroblasts. *J. Neurosci.* **30,** 7215–26 (2010).

59. Topalidou, I. *et al.* Genetically separable functions of the MEC-17 tubulin acetyltransferase affect microtubule organization. *Curr. Biol.* **22,** 1057–65 (2012).

60. Cueva, J. G., Hsin, J., Huang, K. C. & Goodman, M. B. Posttranslational acetylation of α-tubulin constrains protofilament number in native microtubules. *Curr. Biol.* **22,** 1066–74 (2012).

61. Howes, S. C., Alushin, G. M., Shida, T., Nachury, M. V & Nogales, E. Effects of tubulin acetylation and tubulin acetyltransferase binding on microtubule structure. *Mol. Biol. Cell* **25,** 257–66 (2014).

62. Gaertig, J. *et al.* Acetylation of Lysine 40 in α-tubulin Is Not Essential in Tetrahymena thermophila. *J. Cell Biol.* **129,** 1301–1310 (1995).

63. Matsuyama, A. *et al.* In vivo destabilization of dynamic microtubules by HDAC6-mediated deacetylation. *EMBO J.* **21,** 6820–31 (2002).

64. Hubbert, C. *et al.* HDAC6 is a microtubule-associated deacetylase. *Nature* **417,** 455–458 (2002).

65. North, B. J., Marshall, B. L., Borra, M. T., Denu, J. M. & Verdin, E. The human Sir2 ortholog, SIRT2, is an NAD+-dependent tubulin deacetylase. *Mol. Cell* **11,** 437–444 (2003).

66. Zhang, X. *et al.* HDAC6 Modulates Cell Motility by Altering the Acetylation Level of Cortactin. *Mol. Cell* **27,** 197–213 (2007).

67. Zilberman, Y. *et al.* Regulation of microtubule dynamics by inhibition of the tubulin deacetylase HDAC6. *J. Cell Sci.* **122,** 3531–3541 (2009).

68. Seigneurin-Berny, D. *et al.* Identification of components of the murine histone

deacetylase 6 complex: link between acetylation and ubiquitination signaling pathways. *Mol. Cell. Biol.* **21,** 8035–44 (2001).

69. Hook, S. S., Orian, A., Cowley, S. M. & Eisenman, R. N. Histone deacetylase 6 binds polyubiquitin through its zinc finger (PAZ domain) and copurifies with deubiquitinating enzymes. *Proc. Natl. Acad. Sci. U. S. A.* **99,** 13425–13430 (2002).

70. Ohkawa, N. *et al.* N-acetyltransferase ARD1-NAT1 regulates neuronal dendritic development. *Genes to Cells* **13,** 1171–1183 (2008).

71. Conacci-Sorrell, M., Ngouenet, C. & Eisenman, R. N. Myc-nick: A cytoplasmic cleavage product of Myc that promotes α-tubulin acetylation and cell differentiation. *Cell* **142,** 480–493 (2010).

72. Creppe, C. *et al.* Elongator Controls the Migration and Differentiation of Cortical Neurons through Acetylation of α-Tubulin. *Cell* **136,** 551–564 (2009).

73. Solinger, J. A. *et al.* The Caenorhabditis elegans elongator complex regulates neuronal α-tubulin acetylation. *PLoS Genet.* **6,** (2010).

74. Akella, J. S. *et al.* MEC-17 is an alpha-tubulin acetyltransferase. *Nature* **467,** 218–22 (2010).

75. Kalebic, N. *et al.* αTAT1 is the major α-tubulin acetyltransferase in mice. *Nat. Commun.* **4,** 1962 (2013).

76. Kim, G.-W., Li, L., Gorbani, M., You, L. & Yang, X.-J. Mice lacking α-tubulin acetyltransferase 1 are viable but display α-tubulin acetylation deficiency and dentate gyrus distortion. *J. Biol. Chem.* **288,** 20334–50 (2013).

77. Friedmann, D. R., Aguilar, A., Fan, J., Nachury, M. V & Marmorstein, R. Structure of the α-tubulin acetyltransferase, αTAT1, and implications for tubulin-specific acetylation. *Proc. Natl. Acad. Sci. U. S. A.* **109,** 19655–60 (2012).

78. Davenport, A. M. *et al.* Structural and functional characterization of the α-tubulin acetyltransferase MEC-17. *J. Mol. Biol.* **426,** 2605–2616 (2014).

79. Neumann, B. & Hilliard, M. Loss of MEC-17 leads to microtubule instability and

axonal degeneration. *Cell Rep.* **6,** 93–103 (2014).

80. Kalebic, N. *et al.* Tubulin acetyltransferase αTAT1 destabilizes microtubules independently of its acetylation activity. *Mol. Cell. Biol.* **33,** 1114–23 (2013).

81. Kormendi, V., Szyk, A., Piszczek, G. & Roll-Mecak, A. Crystal structures of tubulin acetyltransferase reveal a conserved catalytic core and the plasticity of the essential N terminus. *J. Biol. Chem.* **287,** 41569–75 (2012).

82. Maruta, H., Greer, K. & Rosenbaum, J. L. The Acetylation of Alpha-Tubulin and Its Relationship to the Assembly and Disassembly of Microtubules Preparation of Chlamydomonas Cell Body Extract. *J. Cell Biol.* **103,** 571–579 (1986).

83. Shida, T., Cueva, J. G., Xu, Z., Goodman, M. B. & Nachury, M. V. The major alpha-tubulin K40 acetyltransferase alphaTAT1 promotes rapid ciliogenesis and efficient mechanosensation. *Proc. Natl. Acad. Sci. U. S. A.* **107,** 21517–22 (2010).

84. Szyk, A. *et al.* Molecular basis for age-dependent microtubule acetylation by tubulin acetyltransferase. *Cell* **157,** 1405–15 (2014).

85. Odde, D. Diffusion inside microtubules. *Eur. Biophys. J.* **27,** 514–20 (1998).

86. Yajima, H. *et al.* Conformational changes in tubulin in GMPCPP and GDP-taxol microtubules observed by cryoelectron microscopy. *J. Cell Biol.* **198,** 315–322 (2012).

87. Chen, S., Owens, G. C., Makarenkova, H. & Edelman, D. B. HDAC6 Regulates mitochondrial transport in hippocampal neurons. *PLoS One* **5,** (2010).

88. Outeiro, T. F. *et al.* Sirtuin 2 Inhibitors Rescue a-Synuclein–Mediated Toxicity in Models of Parkinson's Disease. *Science (80-.).* **317,** 516–519 (2007).

89. Godena, V. K. *et al.* Increasing microtubule acetylation rescues axonal transport and locomotor deficits caused by LRRK2 Roc-COR domain mutations. *Nat. Commun.* **5,** 5245 (2014).

90. Zhang, Z. *et al.* HDAC6 Expression Is Correlated with Better Survival in Breast Cancer HDAC6 Expression Is Correlated with Better Survival in Breast Cancer. **10,** 6962–6968 (2004).

91. Haggarty, S. J., Koeller, K. M., Wong, J. C., Grozinger, C. M. & Schreiber, S. L. Domain-selective small-molecule inhibitor of histone deacetylase 6 (HDAC6)-mediated tubulin deacetylation. *Proc. Natl. Acad. Sci. U. S. A.* **100,** 4389–94 (2003).

92. Catalano, M. G., Poli, R., Pugliese, M., Fortunati, N. & Boccuzzi, G. Valproic acid enhances tubulin acetylation and apoptotic activity of paclitaxel on anaplastic thyroid cancer cell lines. *Endocr. Relat. Cancer* **14,** 839–845 (2007).

93. Stones, R., Benoist, D., Peckham, M. & White, E. Microtubule proliferation in right ventricular myocytes of rats with monocrotaline-induced pulmonary hypertension. *J. Mol. Cell. Cardiol.* **56,** 91–6 (2013).

94. Tagawa, H. *et al.* Cytoskeletal Mechanics in Pressure-Overload Cardiac Hypertrophy. *Circ. Res.* **80 ,** 281–289 (1997).

95. Cooper, G. Cytoskeletal networks and the regulation of cardiac contractility: microtubules , hypertrophy , and cardiac dysfunction. *Am J Physiol Hear. Circ Physiol* **291,** 1003–1014 (2006).

96. Quinones, G. B., Danowski, B. a, Devaraj, A., Singh, V. & Ligon, L. a. The posttranslational modification of tubulin undergoes a switch from detyrosination to acetylation as epithelial cells become polarized. *Mol. Biol. Cell* **22,** 1045–57 (2011).

97. Arce, C. a, Casale, C. H. & Barra, H. S. Submembraneous microtubule cytoskeleton: regulation of ATPases by interaction with acetylated tubulin. *FEBS J.* **275,** 4664–74 (2008).

98. Wickström, S. a, Masoumi, K. C., Khochbin, S., Fässler, R. & Massoumi, R. CYLD negatively regulates cell-cycle progression by inactivating HDAC6 and increasing the levels of acetylated tubulin. *EMBO J.* **29,** 131–144 (2009).

99. Castro-Castro, A., Janke, C., Montagnac, G., Paul-Gilloteaux, P. & Chavrier, P. ATAT1/MEC-17 acetyltransferase and HDAC6 deacetylase control a balance of acetylation of alpha-tubulin and cortactin and regulate MT1-MMP trafficking and breast tumor cell invasion. *Eur. J. Cell Biol.* **91,** 950–60 (2012).

100. Brion, B. H. and J.-P. Reduction of Acetylated a-Tubulin Immunoreactivity in Neurofibrillary Tangle-bearing Neurons in Alzheimer's Disease. *J. Neuropathol. Exp. Neurol.* **55,** 964–972 (1996).

101. Perdiz, D., Mackeh, R., Poüs, C. & Baillet, A. The ins and outs of tubulin acetylation: more than just a post-translational modification? *Cell. Signal.* **23,** 763–71 (2011).

102. Howes, S. C., Alushin, G. M., Shida, T., Nachury, M. V & Nogales, E. Effects of tubulin acetylation and tubulin acetyltransferase binding on microtubule structure. *Mol. Biol. Cell* **25,** 257–66 (2014).

103. Coombes, C. E., Yamamoto, A., Kenzie, M. R., Odde, D. J. & Gardner, M. K. Evolving tip structures can explain age-dependent microtubule catastrophe. *Curr. Biol.* **23,** 1342–8 (2013).

104. Gardner, M. K. *et al.* Rapid microtubule self-assembly kinetics. *Cell* **146,** 582–92 (2011).

105. Demchouk, A. O., Gardner, M. K. & Odde, D. J. Microtubule Tip Tracking and Tip Structures at the Nanometer Scale Using Digital Fluorescence Microscopy. *Cell. Mol. Bioeng.* **4,** 192–204 (2011).

106. Northrup, S. H. & Erickson, H. P. Kinetics of protein-protein association explained by Brownian dynamics computer simulation. *Proc. Natl. Acad. Sci. U. S. A.* **89,** 3338–3342 (1992).

107. Gupta, K. K. *et al.* Mechanism for the catastrophe-promoting activity of the microtubule destabilizer Op18/stathmin. *Proc. Natl. Acad. Sci. U. S. A.* **110,** 20449–54 (2013).

108. Schulze, E., Francisco, S., Lafayette, W. & Angeles, L. Posttranslational Modification and Microtubule Stability. *J. Cell Biol.* **105,** 2167–2177 (1987).

109. Li, Y. & Black, M. Microtubule Assembly and Turnover in Growing Axons. *J. Neurosci.* **16,** 531–544 (1996).

110. Bulinski, J. C., Richards, J. E. & Piperno, G. Posttranslational Modifications of a Tubulin : Detyrosination and Acetylation Differentiate Populations of Interphase

Microtubules in Cultured Cells. *J. Cell Biol.* **106,** 1213–1220 (1988).

111. Thompson, W. C., Asai, D. J. & Carney, D. H. Heterogeneity among microtubules of the cytoplasmic microtubule complex detected by a monoclonal antibody to alpha tubulin. *J. Cell Biol.* **98,** 1017–1025 (1984).

112. Montagnac, G. *et al.* αTAT1 catalyses microtubule acetylation at clathrin-coated pits. *Nature* **502,** 567–570 (2013).

113. Kalebic, N. *et al.* The Tubulin Acetyltransferase αTAT1 Destabilizes Microtubules Independently of its Acetylation Activity. *Mol. Cell. Biol.* **3502,** (2012).

114. Gell, C. *et al. Microtubule dynamics reconstituted in vitro and imaged by single-molecule fluorescence microscopy*. *Methods in Cell Biology* **95,** (Elsevier, 2010).

115. Gardner, M. K., Odde, D. J. & Bloom, K. Kinesin-8 molecular motors: putting the brakes on chromosome oscillations. *Trends Cell Biol.* **18,** 307–310 (2008).

116. Gardner, M. K. *et al.* Tension-dependent Regulation of Microtubule Dynamics at Kinetochores Can Explain Metaphase Congression in Yeast □. *Mol. Biol. Cell* **16,** 3764–3775 (2005).

117. Sprague, B. L. *et al.* Mechanisms of Microtubule-Based Kinetochore Positioning in the Yeast Metaphase Spindle. *Biophys. J.* **84,** 3529–3546 (2003).

118. Schek, H. T., Gardner, M. K., Cheng, J., Odde, D. J. & Hunt, A. J. Microtubule Assembly Dynamics at the Nanoscale. *Curr. Biol.* **17,** 1445–1455 (2007).

119. VanBuren, V., Cassimeris, L. & Odde, D. J. Mechanochemical model of microtubule structure and self-assembly kinetics. *Biophys. J.* **89,** 2911–26 (2005).

120. VanBuren, V., Odde, D. J. & Cassimeris, L. Estimates of lateral and longitudinal bond energies within the microtubule lattice. *Pnas* **99,** 6035–6040 (2002).

121. Walker, R. A. *et al.* Dynamic Instability of Individual Microtubules. *J. Cell Biol.* **107,** 1437–1448 (1988).

122. Stepanova, T. *et al.* History-dependent catastrophes regulate axonal microtubule behavior. *Curr. Biol.* **20,** 1023–1028 (2010).

123. Brun, L., Rupp, B., Ward, J. J. & Nédélec, F. A theory of microtubule catastrophes and their regulation. *Proc. Natl. Acad. Sci. U. S. A.* **106,** 21173–21178 (2009).

124. Margolin, G., Goodson, H. V. & Alber, M. S. Mean-field study of the role of lateral cracks in microtubule dynamics. *Phys. Rev. E - Stat. Nonlinear, Soft Matter Phys.* **83,** 1–14 (2011).

125. Margolin, G. *et al.* The mechanisms of microtubule catastrophe and rescue: implications from analysis of a dimer-scale computational model. *Mol. Biol. Cell* **23,** 642–656 (2012).

126. Chretien, D., Metoz, F., Verde, F., Karsenti, E. & Wade, R. H. Lattice defects in microtubules: Protofilament numbers vary within individual microtubules. *J. Cell Biol.* **117,** 1031–1040 (1992).

127. Gell, C. *et al.* Microtubule dynamics reconstituted in vitro and imaged by single-molecule fluorescence microscopy. *Methods Cell Biol.* **95,** 221–45 (2010).

128. Blake-Hodek, K. A., Cassimeris, L. & Huffaker, T. C. Regulation of Microtubule Dynamics by Bim1 and Bik1, the Budding Yeast Members of the EB1 and CLIP-170 Families of Plus-End Tracking Proteins. *Mol. Biol. Cell* **21,** 2013–2023 (2010).

129. Hyman, A. A., Salser, S., Drechsel, D. N., Unwin, N. & Mitchison, T. J. Role of GTP hydrolysis in microtubule dynamics: information from a slowly hydrolyzable analogue, GMPCPP. *Mol. Biol. Cell* **3,** 1155–67 (1992).

130. Helenius, J., Brouhard, G., Kalaidzidis, Y., Diez, S. & Howard, J. The depolymerizing kinesin MCAK uses lattice diffusion to rapidly target microtubule ends. *Nature* **441,** 115–119 (2006).

131. Montenegro Gouveia, S. *et al.* In vitro reconstitution of the functional interplay between MCAK and EB3 at microtubule plus ends. *Curr. Biol.* **20,** 1717–1722 (2010).

132. Friel, C. T. & Howard, J. The kinesin-13 MCAK has an unconventional ATPase cycle adapted for microtubule depolymerization. *Embo J* **30,** 3928–3939 (2011).

133. Tran, P. T., Walker, R. A. & Salmon, E. D. A metastable intermediate state of microtubule dynamic instability that differs significantly between plus and minus

ends. *J. Cell Biol.* **138,** 105–117 (1997).

134. Fygenson, D. K., Braun, E. & Libchaber, A. Phase diagram of microtubules. *Phys. Rev. E* **50,** 1579–1588 (1994).

135. Maurer, S. P., Fourniol, F. J., Bohner, G., Moores, C. a & Surrey, T. EBs recognize a nucleotide-dependent structural cap at growing microtubule ends. *Cell* **149,** 371–82 (2012).

136. Cooper, J. R., Wagenbach, M., Asbury, C. L. & Wordeman, L. Catalysis of the microtubule on-rate is the major parameter regulating the depolymerase activity of MCAK. *Nat. Struct. Mol. Biol.* **17,** 77–82 (2010).

137. Rymut, S. M. & Kelley, T. J. Broader implications : biological and clinical significance of microtubule acetylation. *Cell Health Cytoskelet.* **7,** 71–82 (2015).